Single Rotor, Dual Stator Axial Flux Permanent Magnet Motor Design, Analysis and Test

By

Calvin H. Corey III

Submitted in partial fulfillment of the requirements for the degree of

Master of Science

(Electrical Engineering)

at the

UNIVERSITY OF WISCONSIN-MADISON

2019

Under Supervision of Professor Bulent Sarlioglu

Approved by 

Bulent Sarlioglu

Date May 2, 2019

Abstract

The Axial Flux Permanent Magnet (AFPM) motor is a unique machine topology which possesses advantages over Radial Field Permanent Magnet (RFPM) machines. Over the last several decades this uniqueness has garnered interest, yet RFPM motors continue to be to most prevalent PM motor topology in industry. This thesis will investigate the Single Rotor, Dual slotted Stator (SRDS) topology with integral-slot windings for comparison against more conventional Single Rotor, Single Stator (SRSS) RFPM machines.

To facilitate investigation of the SRDS AFPM motor, this thesis reviews and extends existing RFPM analytical modeling techniques for application and use in AFPM machines. During developing of analytical modeling equations an alternative method for prediction of no-load Back-Electromotive Force (BEMF) waveforms will be developed for comparison against classical finite element predictions. An in-depth review of phase self-inductance calculations as well as overall machine performance calculations will be carried out.

In addition to analytical modeling, this thesis will investigate Two Dimensional (2D) Finite Element (FE) representations of the SRDS axial field motor. This exploration aims to address the inherent Three Dimensional (3D) nature of AFPM motors and quantify the accuracy of 2D modeling techniques, relative to analytic and 3D predictions. Lastly, a prototype SRDS AFPM will be manufactured for comparison to analytical and finite element predictions.

Acknowledgments

I wish to express my sincere gratitude to all of those who have contributed knowledge, time, effort and funding for this thesis. First, I would like to thank Professor Bulent Sarlioglu for affording me the opportunity to conduct this research under his advisement.

I would like to extend a special thank you to DRS Naval Power Systems for supporting this thesis through funding the prototype machine material and build. A special thank you to Ed Thaxton, William Wink, Eric Tripodi, Gary Plowman, Mark Coluci, Pablo Melendez, Eddy Heriberto, and all of the others at DRS whom helped me through this project and the especially hard task of building a prototype machine.

I would also like to extend a special thank you to Chris Cheek and Peter Fail of 3L Power, whom graciously allowed me to use their test facility and hardware while conducting this research.

I would also like to thank Professor Jahns, Professor Giri, Professor Fredette, Professor Duffy, and Professor Zinn for the outstanding education they afforded me while I attended U.W. Madison.

I would also like to thank Noremac Manufacturing, Electro-Core, and BJA magnetics for providing me with the material required to build a prototype machine.

Finally, and most of all I would like to extend a very special thanks to my fiancé Hayley, and my family. Without their continued support, patience and sacrifice this thesis would have not been possible.

Acronyms, Abbreviations and Nomenclature

A	electrical current in amperes, shear plane area, conductor area
α	conductor temperature coefficient, coil pitch angle
α_{skew}	stator skew angle
α_{sm}	smoothing function variable
A_{cu}	cross sectional area of stator conductor
A_g	air gap area in the reluctance path across the air gap
A_m	magnet area in the reluctance path across the air gap
A_s	cross sectional area of stator slot
AFPM	axial flux permanent magnet
B	air gap flux density
$B(\Theta)$	air gap flux density as a function of electrical angle
BEMF	back-electromotive force
B_{pk}	peak value of air gap flux density
CPS	coils per slot
D	active rotor diameter
DRTS	dual rotor triple stator
$\mathcal{E}$	electromotive force
e_a	back-electromotive force
EM	electromagnetic
EMF	electromagnetic force
F	force
FE	finite element
FEA	finite element analysis
FFT	fast fourier transform
γ	slot pitch angle
g	air gap height
g'	air gap height modified by carter coefficient
H_m	magnet height in the direction of the air gap

I	electrical current
K_b	stator winding breadth factor
K_c	carter's coefficient
Ke	electrical constant in V/RPM
K_n	stator winding skew factor
K_p	stator winding pitch factor
K_{sm}	waveform smooth function
Kt	torque constant in ft-lbs/A
K_w	stator winding factor
L	active electromagnetic length, half of the waveform period
λ	flux linkage
λ_n	flux linkage of n discretized FEA model
L_{AA}	phase self-inductance
L_c	length of stator conductor
L_e	end turn component of phase inductance
L_g	air gap component of phase inductance
L_{phase}	phase self-inductance
L_s	slot leakage inductance, electromagnetic length
m	number of slots per rotor pole, per motor phase
m_{frac}	fractional portion of magnet relative to a full pitch magnet
N	number of conductors
n	number of conductors, harmonic number
n_{cs}	number of coils per stator slot
N_s	number of stator slots
n_{ts}	number of turns per coil
Θ	electrical angle
Φ	magnetic flux
P	number of rotor poles, slot permeance coefficient
PP	number of rotor pole pairs
ρ	resistivity of stator conductor
PCB	printed circuit board

PM	permanent magnet
Q	number of motor phases
$RFPM$	radial field permanent magnet
$\mathscr{R}_g$	air gap reluctance
$\mathscr{R}_m$	magnet reluctance
R_{iw}	inside working radius
r_n	average radius of n discretized FEA model
R_{ow}	outside working radius
R_{phase}	phase resistance
S_{pf}	slot packing factor
SPP	slots per pole per phase
$SRDS$	single rotor, dual stator
$SRSS$	single rotor, single stator
T	torque
t	time
T_f	operation temperature of conductor
THD	total harmonic distortion
T_0	initial temperature of conductor
T_{ph}	conductor turns per motor phase
τ_s	pitch length of stator slot and tooth width
τ_{cp}	circumferential length of end turns
σ	shear stress, lancoz sigma factor
μ_r	recoil permeability
V	voltage
$V_{emf}(\Theta,t)$	back electromotive force as a function of electrical angle and time
VFD	variable frequency drive
$Vrms$	root mean squared voltage
ω_s	slot width
x	distance

Table of Contents

Abstract ii

Acknowledgments iii

Acronyms, Abbreviations and Nomenclature iv

Chapter 1 1

Introduction 1

1.1 Background and Overview 1

1.2 Thesis Contributions 2

1.3 Thesis Layout 3

Chapter 2 5

Electric Machines Review 5

2.1 Electric Motor Types and Classes 5

2.1.1 Permanent Magnet Motor Classification 7

2.2 Axial Flux Machines 7

2.2.1 Single Rotor, Dual Slotted Stator Axial Field Machines 8

Chapter 3 13

Analytical Design and Sizing of Axial Field PM Motors 13

3.1 Permanent Magnet Motor Fundamental Concepts and Terminology 13

3.2 Initial Machine Size: Torque Density Scaling Method 18

3.3 Equivalent Circuit Model 21

3.3.1 Winding Resistance 22

3.3.2 Winding Factors 23

3.3.3 Back Electromotive Force 27

3.3.4 Phase Self Inductance 30

3.3.5 Overall Machine Efficiency 38

3.4 Analytical No-Load Waveform Prediction 42

3.4.1 Idealized Air Gap Flux Density 43

3.4.2 Back-EMF Waveforms 45

Chapter 4 47

Finite Element Performance Modeling 47

4.1 Introduction and Motivation for 2D Modeling of Axial Field Motors. 47

4.2 2D “Unwrapped” Modeling Approaches. 47

Chapter 5 55

Machine Design and Performance Case Study 55

5.1 Machine under Evaluation 55

5.2 Analytical Performance Predictions 57

5.3 2D Finite Element Performance 60

5.3.1 Planar Modeling of Axial Flux Machines 60

5.3.2 Unconstrained and Flux Wrapper Full Models: 90

5.4 Discussion of Case Study Results 93

5.4.1 Performance Comparison 94

5.4.2 Analysis Computation Time 99

5.5 Summary of SRDS AFPM Modeling Efforts 100

Chapter 6 102

Experimental Results 102

6.1 Prototype SRDS AFPM Characteristics 102

6.2 Machine Performance Testing: Setup and Test Conditions. 103

6.3 Unloaded Machine Measurements 105

6.3.1 Back-EMF Test Data 105

6.3.2 Inductance and Resistance Testing 107

6.4 Experimental Machine: Load and Efficiency Testing 108

6.4.1 Discussion of Load and Efficiency Test Results 110

6.5 Summary of Experimental Data 111

Chapter 7 112

Conclusions and Future Work 112

7.1 Conclusions 112

7.2 Recommendations for Future Work 113

7.2.1 2D FE Modeling of Alternative Axial Flux Machines 113

7.2.2 2D FE Modeling of Alternative Slot and Magnet Configurations 113

7.2.3 2D FE Optimization and Design of Experiments 113

7.2.4 2D FE Cogging Prediction Refinement 114

7.2.5 Analytical BEMF Prediction 114

7.2.6 Quantification of 3D FE Effects 114

References 115

List of Figures

Figure 1. Electric Machinery Family 6

Figure 2. Permanent Magnet Motor Types 7

Figure 3. PA44 Single Rotor, Dual Stator 625hp Motor [5] 9

Figure 4. PA57-1000 Single Rotor, Dual Stator PM 1000hp Generator [40] 9

Figure 5. GKN-EVO eDrive Systems Prototype AF-130 Single Rotor, Dual Stator 89hp motor [44], [47] 10

Figure 6. NASA 1500hp TACOM Motor [46] 10

Figure 7. Large Power Direct-Driven 130kW Generator [45] 11

Figure 8. Sumitomo Electric Single Rotor, Dual Stator PMM [43] 12

Figure 9. 2D Model of Surface Mount Radial Field Permanent Magnet Motor with Parallel Sided Slots. 14

Figure 10. Flux Path in Surface Mount Permanent Magnet Motor with Parallel Sided Slots 16

Figure 11. Topologies and Flux path of RFPM (a) and AFPM (b) motors [1] 17

Figure 12. Circumferential Slice of SRDS AFPM (Shaft Not Shown) 17

Figure 13. Motor Shear Planes (Left), Radial Field Motor (Center), Axial Field Motor, Stator not Shown (Right) 18

Figure 14. Force on sheet of current-carrying conductors, resulting from magnetic B-field [10] 19

Figure 15. Single Phase Equivalent Circuit of PM Motor 21

Figure 16. 3-Phase, Wye Connected Equivalent Circuit Model 22

Figure 17. Winding Pitch for a 2-pole motor with short-pitched coils [4] 25

Figure 18. Slot pitch angle for single phase, 2-pole motor, m=5 [4] 26

Figure 19. Visualization of Carter Coefficient. [13] 29

Figure 20. Two Air Gap C-Core and Corresponding Magnetic Circuit Diagram 31

Figure 21. Two Airgap C-Core with Permanent Magnet (black) Replacing One Airgap 32

Figure 22. 4-Pole Radial Field PM Motor and Resulting Magnetic Circuit Model 32

Figure 23. Slot Leakage Flux [13] 35

Figure 24. Slot Permeance Coefficients [17] 36

Figure 25. RFPM Motor Coil End Turn Geometry Assumption (Left), AFPM Coil End Turn Geometry (Right) 37

Figure 26. M-10X Electrical Steel, Core Loss Rate Table [62] 41

Figure 27. Idealized Air Gap Flux Distribution for Non-Continuous SRDS AFPM Motor 43

Figure 28. Axial flux motor assembly and equivalent 2-D planar representation (a), single planar model representation of axial flux motor (b) and planar model with two discrete segments (c). 48

Figure 29. Single pole, single planar FEA model of AFPM 49

Figure 30. Single pole, two discrete segment FEA model representation of an AFPM 49

Figure 31. Improperly conditioned 2D, 4-pole AFPM FE Model 51

Figure 32. 4-pole AFPM FE Model with two extra magnets and 6 extra slots. 52

Figure 33. 4-pole AFPM FE Model with two extra magnets and 12 extra slots. 52

Figure 34. 4-pole AFPM FE Model with two extra magnets and Flux Wrappers 53

Figure 35. 4-pole AFPM FE Model with antiperiodic boundary conditions 54

Figure 36. Exploded View of 60-Slot, 10-Pole SRDS AFPM 56

Figure 37. Flux 3D Model of 60-Slot, 10-Pole SRDS AFPM 57

Figure 38. SRDS AFPM Motor Performance Summary, 5Hp at 1800 RPM Operation 58

Figure 39. SRDS AFPM Motor Efficiency Map 58

Figure 40. Analytical Back-EMF vs. 3D FEA Back-EMF at 1800 RPM 59

Figure 41. FFT of Analytical Back-EMF vs. FFT of 3D FEA Back-EMF at 1800 RPM, (a) 1st through 20th Harmonic, (b) 3rd through 20th Harmonic. 60

Figure 42. (a) Single Slice 2D FEA vs. 3D FEA Back-EMF at 1800 RPM and (b) Single Slice 2D FEA vs. 3D FEA Flux Linkage at 1800 RPM 61

Figure 43. FFT of 2D FEA, Single Slice Model Back-EMF vs. FFT of 3D FEA Back-EMF at 1800 RPM, (a) 1st through 20th Harmonic, (b) 3rd through 20th Harmonic 62

Figure 44. 2D FEA, Single Slice Model Terminal Voltage vs 3D FEA Terminal Voltage, 1800 RPM, 5.0Apk excitation (a), Resulting Electromagnetic Torque (b) 63

Figure 45. 2D FEA, Single Slice Model Terminal Voltage vs 3D FEA Terminal Voltage, 1800 RPM, 13.25Apk excitation (a), Resulting Electromagnetic Torque (b) 63

Figure 46. 2D FEA, Single Slice Model Terminal Voltage vs 3D FEA Terminal Voltage, 1800 RPM, 40.0Apk excitation (a), Resulting Electromagnetic Torque (b) 63

Figure 47. 2D FEA, Single Slice Model Terminal Voltage vs 3D FEA Terminal Voltage, 1800 RPM, 100Apk excitation (a), Resulting Electromagnetic Torque (b) 64

Figure 48. 2D FEA, Single Slice Model Kt vs. vs 3D FEA Kt vs. Analytical Kt 65

Figure 49. 2D FEA, Single Slice Cogging Torque vs. 3D FEA Cogging Torque Predictions 66

Figure 50. 2-Slice 2D FEA vs. 3D FEA Back-EMF at 1800 RPM 66

Figure 51. FFT of 2D FEA, 2-Slice Model Back-EMF vs. FFT of 3D FEA Back-EMF at 1800 RPM, (a) 1st through 20th Harmonic, (b) 3rd through 20th Harmonic 67

Figure 52. Two Slice 2D FEA vs. 3D FEA Flux Linkage at 1800 RPM 68

Figure 53. 2D FEA, 2-Slice Model Terminal Voltage vs 3D FEA Terminal Voltage, 1800 RPM, 5.0Apk Excitation (a), Resulting Electromagnetic Torque (b) 68

Figure 54. 2D FEA, 2-Slice Model Terminal Voltage vs 3D FEA Terminal Voltage, 1800 RPM, 13.25Apk excitation (a), Resulting Electromagnetic Torque (b) 69

Figure 55. 2D FEA, 2-Slice Model Terminal Voltage vs 3D FEA Terminal Voltage, 1800 RPM, 40.0Apk excitation (a), Resulting Electromagnetic Torque (b) 69

Figure 56. 2D FEA, 2-Slice Model Terminal Voltage vs 3D FEA Terminal Voltage, 1800 RPM, 100Apk excitation (a), Resulting Electromagnetic Torque (b) 69

Figure 57. 2D FEA, 2-Slice Model Kt vs. vs 3D FEA Kt vs. Analytical Kt 71

Figure 58. 2D FEA, 2-Slice Cogging Torque vs. 3D FEA Cogging Torque Predictions 71

Figure 59. 4-Slice 2D FEA vs. 3D FEA Back-EMF at 1800 RPM 72

Figure 60. FFT of 2D FEA, 4-Slice Model Back-EMF vs. FFT of 3D FEA Back-EMF at 1800 RPM, (a) 1st through 20th Harmonic, (b) 3rd through 20th Harmonic 73

Figure 61. Four Slice 2D FEA vs. 3D FEA Flux Linkage at 1800 RPM 74

Figure 62. 2D FEA, 4-Slice Model Terminal Voltage vs 3D FEA Terminal Voltage, 1800 RPM, 5.0Apk excitation (a), Resulting Electromagnetic Torque (b) 74

Figure 63. 2D FEA, 4-Slice Model Terminal Voltage vs 3D FEA Terminal Voltage, 1800 RPM, 13.25Apk excitation (a), Resulting Electromagnetic Torque (b) 75

Figure 64. 2D FEA, 4-Slice Model Terminal Voltage vs 3D FEA Terminal Voltage, 1800 RPM, 40.0Apk excitation (a), Resulting Electromagnetic Torque (b) 75

Figure 65. 2D FEA, 4-Slice Model Terminal Voltage vs 3D FEA Terminal Voltage, 1800 RPM, 100Apk excitation (a), Resulting Electromagnetic Torque (b) 75

Figure 66. 2D FEA, 4-Slice Model Kt vs. vs 3D FEA Kt vs. Analytical Kt 77

Figure 67. 2D FEA, 4-Slice Cogging Torque vs. 3D FEA Cogging Torque Predictions 78

Figure 68. 8-Slice 2D FEA vs. 3D FEA Back-EMF at 1800 RPM 78

Figure 69. FFT of 2D FEA, 8-Slice Model Back-EMF vs. FFT of 3D FEA Back-EMF at 1800 RPM, (a) 1st through 20th Harmonic, (b) 3rd through 20th Harmonic 79

Figure 70. 8-Slice 2D FEA vs. 3D FEA Flux Linkage at 1800 RPM 80

Figure 71. 2D FEA, 8-Slice Model Terminal Voltage vs 3D FEA Terminal Voltage, 1800 RPM, 5.0Apk excitation (a), Resulting Electromagnetic Torque (b) 80

Figure 72. 2D FEA, 8-Slice Model Terminal Voltage vs 3D FEA Terminal Voltage, 1800 RPM, 13.25Apk excitation (a), Resulting Electromagnetic Torque (b) 81

Figure 73. 2D FEA, 8-Slice Model Terminal Voltage vs 3D FEA Terminal Voltage, 1800 RPM, 40.0Apk excitation (a), Resulting Electromagnetic Torque (b) 81

Figure 74. 2D FEA, 8-Slice Model Terminal Voltage vs 3D FEA Terminal Voltage, 1800 RPM, 100Apk excitation (a), Resulting Electromagnetic Torque (b) 81

Figure 75. 2D FEA, 8-Slice Model Kt vs. vs 3D FEA Kt vs. Analytical Kt 83

Figure 76. 2D FEA, 8-Slice Cogging Torque vs. 3D FEA Cogging Torque Predictions 83

Figure 77. 16-Slice 2D FEA vs. 3D FEA Back-EMF at 1800 RPM 84

Figure 78. FFT of 2D FEA, 16-Slice Model Back-EMF vs. FFT of 3D FEA Back-EMF at 1800 RPM, (a) 1st through 20th Harmonic, (b) 3rd through 20th Harmonic 85

Figure 79. 16-Slice 2D FEA vs. 3D FEA Flux Linkage at 1800 RPM 86

Figure 80. 2D FEA, 16-Slice Model Terminal Voltage vs 3D FEA Terminal Voltage, 1800 RPM, 5.0 Apk excitation (a), Resulting Electromagnetic Torque (b) 86

Figure 81. 2D FEA, 16-Slice Model Terminal Voltage vs 3D FEA Terminal Voltage, 1800 RPM, 13.25 Apk excitation (a), Resulting Electromagnetic Torque (b) 87

Figure 82. 2D FEA, 16-Slice Model Terminal Voltage vs 3D FEA Terminal Voltage, 1800 RPM, 40.0 Apk excitation (a), Resulting Electromagnetic Torque (b) 87

Figure 83. 2D FEA, 16-Slice Model Terminal Voltage vs 3D FEA Terminal Voltage, 1800 RPM, 100.0 Apk excitation (a), Resulting Electromagnetic Torque (b) 87

Figure 84. 2D FEA, 16-Slice Model Kt vs. vs 3D FEA Kt vs. Analytical Kt 89

Figure 85. 2D FEA, 16-Slice Cogging Torque vs. 3D FEA Cogging Torque Predictions 89

Figure 86. Back-EMF 1800 RPM, Unconstrained and Flux Wrapper 2-D FEA 91

Figure 87. Cogging Torque, Unconstrained and Flux Wrapper 2-D FEA. 92

Figure 88. Cogging Torque, Unconstrained and Flux Wrapper 2-D FEA, 0-180 Electrical Degrees 93

Figure 89. Comparison of all 2D FEA Kt Predictions vs. 3D Kt Predictions vs. Analytical Kt Predictions 95

Figure 90. Single Slice FEMM 2D FEA vs. Single Slice Flux 2D FEA vs. 3D FEA Back-EMF at 1800 RPM 97

Figure 91. Single Slice FEMM 2D FEA vs. Single Slice Flux 2D FEA vs. 3D FEA Cogging Torque 97

Figure 92. SRDS AFPM Loaded Terminal Voltages, Flux 2D vs. FEMM 98

Figure 93. SRDS AFPM Electromagnetic Torque, Flux 2D vs. FEMM 99

Figure 94. Prototype 10-Pole, 60-Slot, SRDS AFPM Assembly (a), One of the SRDS AFPM Stators Before Assembly (b). 102

Figure 95. SRDS AFPM Back-EMF Test Setup 103

Figure 96. SRDS AFPM Load Testing Test Setup 104

Figure 97. SRDS AFPM Load Testing Single Line Diagram 104

Figure 98. SRDS AFPM BEMF Test Data and FFT 105

Figure 99. FFT of Measured Back-EMF Data at 1800 RPM, (a) 1st through 20th Harmonic, (b) 3rd through 20th Harmonic 106

Figure 100. SRDS AFPM Efficiency Measurement vs. Prediction 109

Figure 101. SRDS AFPM Measured Torque Constant, Kt 110

List of Tables

Table I. Typical Shear Stress Values of Electric Machines [10] 20

Table II. SRDS AFPM Machine Parameters 55

Table III. Phase Self Inductance Comparison (2D vs. 3D vs. Analytical) 90

Table IV. Comparison of 2D FEA Voltage Predictions vs. 3D FEA Predictions 94

Table V. Computer Hardware Used For Analysis 100

Table VI. Approximate Computation Time of Each Analysis Method 100

Table VII. Comparison of Predicted Back-EMF Voltage at 1800 RPM. 106

Table VIII. Comparison of Back-EMF Total Harmonic Distortion Predictions 107

Table IX. 2-D AND 3-D FINITE ELEMENT SELF-INDUCTANCE (1A EXCITATION) VS. TEST MEASURED SELF-INDUCTANCE @ 100HZ 107

Table X. Analytic Phase Resistance vs. Test Measured Resistance @ 100Hz 108

Chapter 1

Introduction

1.1 Background and Overview

Permanent magnet motors have been widely adopted across many industry applications ranging from washing machines to automotive and ship propulsion systems [2], [49]-[51]. Despite being widely regarded as one of the most power-dense types of PM motors in existence today [52]-[55], axial field PM motors have been sparsely adopted in industry with only a few commercial examples [5], [6], [40], [47], [48]. Until recent adoption by the automotive industry over the last two decades [49], [50]-[52], [58], the high initial ownership cost of PM technology had reduced adaptation in commercial applications.

The AFPM motor's unique power density enables them to greatly enhance or realize applications which required extreme compactness (e.g. aerospace and military applications), yet industry has been slow to adopt this topology. While this thesis does not specifically target one application, the motivation for this thesis is to further develop industry understanding of SRDS AFPM machines, such that their high power density can be adapted for, and utilized in demanding applications, such as electric aircraft.

The sizing equations of AFPM machines has been thoroughly investigated in prior research and texts [1], [13], [38], [39] [41], [45], [52], [53], [56], [57]. Gieras, Wang, Kamper and Hanselman [1], [13] provide comprehensive texts describing all aspects of design and performance of most AFPM machine technology, including some reference to SRDS slotted motors. However, because reference [1] and [13] are all-encompassing textbooks, details on the SRDS machine design are sparse.

Kim [38] studied analytical methods of predicting machine performance and waveforms using classic winding function techniques. Kim's research concluded with a series of case studies comparing analytical

results to finite element results as well as comparing the performance of toroidal wound stators to more conventional overlapping windings in Single Rotor, Single Stator (SRSS) and Dual Rotor Single toroid Stator (DRSS) style machines.

Aydin [39], Jensen [41] and Tremelling [56] also provide comprehensive evaluations of AFPM machines. Aydin [39] conducted groundbreaking research on AFPM machine cogging torque and airgap flux density characteristics, as well as introducing a new machine type, the Field Controlled Axial Flux Permanent Magnet (FCAFPM). Jensen [41] conducted early research of a DRSS, toroidal wound, amorphous core axially field machine design almost three decades ago, where he designed, and tested a prototype machine. Tremelling [56] conducted research on a Dual Rotor, Triple Stator (DRTS) machine which featured Printed Circuit Board (PCB), slotless stators.

In addition, reference [45] focused on a SRDS design with fractional concentrated windings for direct driven renewable energy, [52] and [57] focused on a DRDS toroidal wound machine design for Electric Vehicles and marine power generator and [53] evaluated a FCAFPM.

While the aforementioned works demonstrate extensive and comprehensive research on AFPM machines, these works also illustrate that the focus has not been in SRDS, slotted stator machines which feature integral slot-pole combinations greater than one Slot per Pole per Phase (SPP).

To address this research gap, this thesis will provide the industry reader with a comprehensive, standalone guide for analytical modeling and of a Single Rotor, Dual Stator Axial Field Permanent Magnet Motor which features integral slot-pole windings with greater than one SPP. This thesis will also propose a new method for the prediction of BEMF waveforms and 2D modeling techniques for AFPM machines.

1.2 Thesis Contributions

This thesis seeks to derive a comprehensive set of analytical equations for analytical prediction of SRDS AFPM performance. Analytical equations will be derived leveraging and extending classic electromagnetic equations which are applied to more standard RFPM machines. Complementing these analytical equations,

this thesis proposes a method for modeling and analyzing SRDS AFPMs using 2D FE models. The presented 2D modeling techniques are derived using average spatial machine parameters and applied predicted forces to an average moment arm. Further investigation is conducted to quantify increases in 2D modeling accuracy afforded through discretizing the 3D geometry into several 2D models and summing the resulting torques and flux linkages from each model. Lastly, this thesis produces a prototype SRDS AFPM and compares experimental results against analytical and FE predictions, validating and quantifying each approaches accuracy.

1.3 Thesis Layout

This thesis will methodically walk through the design, analysis and test of an SRDS AFPM motor with a slotted stator featuring integral slot-pole windings. A prototype motor will then be manufactured, tested and correlated to the analyses conducted throughout this thesis. Emphasis will be placed on developing analytical modeling methods as well as 2D finite element modeling techniques.

Chapter two will develop a quasi-two dimensional planar representation of the SRDS AFPM and will encompass the adaptation of classical RFPM motor electromagnetic analysis methods for use in the design of an axial field machine. Chapter three will develop an equivalent circuit model and derive analytical expressions for circuit components such as phase voltage, BEMF, self-inductance and resistance. This chapter will include analytical BEMF waveform estimations, developed as an extension of work conducted by Zhu and Howe [3], but will incorporate a simplified Fourier Series approach, leveraging classic machine design equations developed by Kirtley, Schmitz, Novotny and others [4], [30], [35], [36], [37].

In Chapter four, 2D finite element modeling techniques will be explored and compared against 3D modeling efforts. This chapter will investigate 2D, single plane modeling of the entire machine, single plane, single pole modeling and multi-plane modeling for SRDS AFPM machines. Each modeling technique will be exercised and pertinent characteristics compared against one another (e.g. airgap flux

density, flux linkage, voltage, torque, etc.). This chapter will conclude by summarizing observations, strengths, and weaknesses of each approach.

Chapter five will conduct a performance case study on an integral slot-pole SRDS AFPM with 2 SPP. The targeted design point is established such that machine performance can be compared against widely available, more conventional machines (e.g. squirrel cage induction motors). The machine under assessment will be designed to achieve five (5) horsepower while operating at eighteen hundred (1800) RPM with a nominal three phase input of two hundred and eight (208) volts per stator. This case study will include analytical and finite element analysis derived in Chapters two and three.

In Chapter six, the machine designed in chapter four will be manufactured and characterized by experimental testing. This chapter will provide background on the hands-on experience of building and testing a SRDS AFPM motor and will detail the results obtained when the prototype motor is tested. Inductance, resistance, BEMF, torque, power factor and efficiency will be measured and compared against analytical and finite element predictions.

Lastly, Chapter seven will summarize the work of this thesis. This chapter will provide key observations, conclusions as well as opportunities for future work. Chapter six will also identify any shortcomings or unexpected results experienced during this thesis.

Chapter 2

Electric Machines Review

This chapter presents a review of literature and motor technology which is relevant to developing an understanding of the Single Rotor, Dual Stator, Axial Field Permanent Magnet motor. First, the broader category of electric machines is explored to provide context on the enormity of electric machines topologies and the sub-category of Axial Field Permanent Magnet motors. After presenting machine topologies and classifications, this chapter provides a thorough description of current state-of-the art commercial and experiments of SRDS AFPM machines. Lastly, this chapter will conclude by introducing RFPM machine terminology and linking the RFPM design to the AFPM design, preparing the reader for 2D modeling efforts of Chapter 3 and beyond.

2.1 Electric Motor Types and Classes

Electric motors can be described in two broad categories, Alternating Current (AC) and Direct Current (DC) Machines. Within these broad categories, machines can be broken into several sub-categories, each with their own unique characteristics and optimal applications. Figure 1 provides an overview of electric machine types and differing topologies:

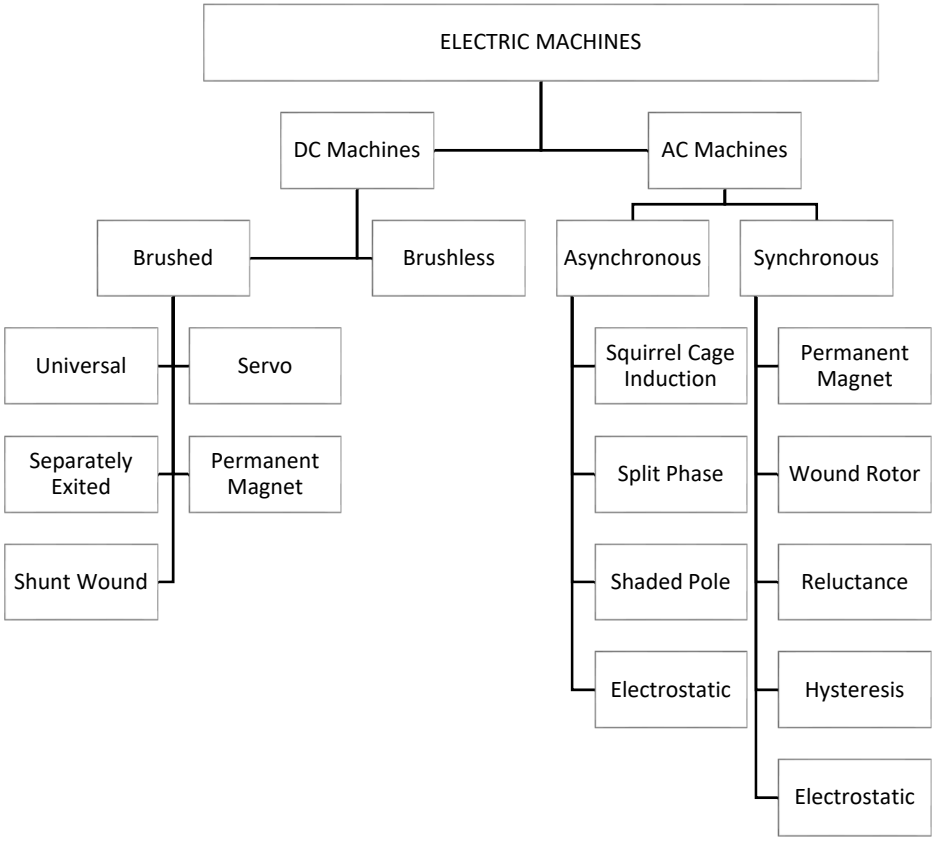

Figure 1. Electric Machinery Family

PM motors can be categorized as both Brushless DC (BLDC) and Synchronous AC machines. As is often the case with PM motors there can be confusion as to which category the machine actually belongs to (BLDC vs. Synchronous). BLDC machines share the same field excitation as the synchronous machine, permanent magnets. The difference lies in the BLDC's armature which is designed for a square, or trapezoidal excitation [5], [8], [20]. In the case of the synchronous machine, a sinusoidal excitation is supplied to the motor's armature for torque and speed production. This thesis will focus on synchronous permanent magnet motors which utilize sinusoidal armature excitation; but the general principles, equations and design approach is equally valid for both permanent magnet topologies.

2.1.1 Permanent Magnet Motor Classification

The first portion of Section 2.1 has laid the groundwork for the focus of this thesis, The PM synchronous motor. However, even in the sub-category of PM synchronous motors, there is broad range of motor topologies in existence. Figure 2 outlines the most prominent styles of PM motor topologies existing today. This thesis will focus on the Single Rotor, Dual Stator sub-class of Axial Field PM motors sometimes referred to as a double-sided Axial Flux Permanent Magnet Motor (AFPM) [1].

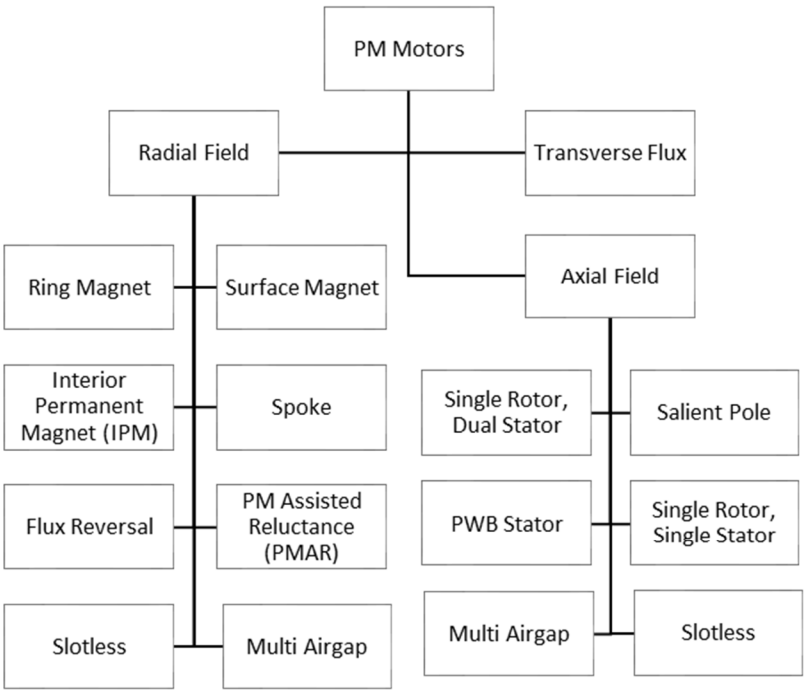

Figure 2. Permanent Magnet Motor Types

2.2 Axial Flux Machines

Axial flux machines are a special sub-class of permanent magnet machines. The AFPM machine is attractive, relative to its RFPM counterpart because of its inherent pancake shape, which results from its disc-type rotor constructions [1] and because of their inherently high torque density [31], [32], [59]. The

AFPM's disc-type rotor assembly affords it suitability for applications where a short axial length is desirable, and can accommodate the AFPM's large diameter rotor.

Kim, Aydin and Jensen have provided comprehensive evaluation and comparison of existing AFPM motor topologies [38], [39], [41]. In the time since these inclusive studies were conducted, electric vehicle (EV) an alternative energy markets have renewed interest in axial flux topologies; This interest comes as the volatility of rare-earth magnet cost has reduced and because of the ongoing volatility in fossil fuel energy sources [28], [44], [45], [47]. To enhance these previous works, Section 2.2.1 provides a summary of additional scientific research examples as well as industrial use of the Single Rotor, Dual slotted Stator AFPM motor.

2.2.1 Single Rotor, Dual Slotted Stator Axial Field Machines

While widely regarded as one of the most power-dense (hp/lb) types of Permanent Magnet motors in existence [46], [51] -[55] there are only a few commercial examples of the AFPM machine [5], [6], [40], [47], [48]. Of these examples even fewer utilize the Single Rotor, Double Stator (SRDS) electromagnetic topology [5], [40], [47]. This section provides a survey of existing SRDS machines and accompanying power density where data is available.

Reference [5] presents a commercial example of a 625 horsepower motor, the PA44, which is primarily used as a top drive motor in the oil and gas industry. The PA44 weight is 395 lbs, yielding a power density rating of 1.58 hp/lb, nearly ten times greater than a typical "small" industrial motor rating of 0.16 hp/lb [46]. The PA44 has a maximum efficiency of 95% and a maximum operating speed of 6000 RPM.

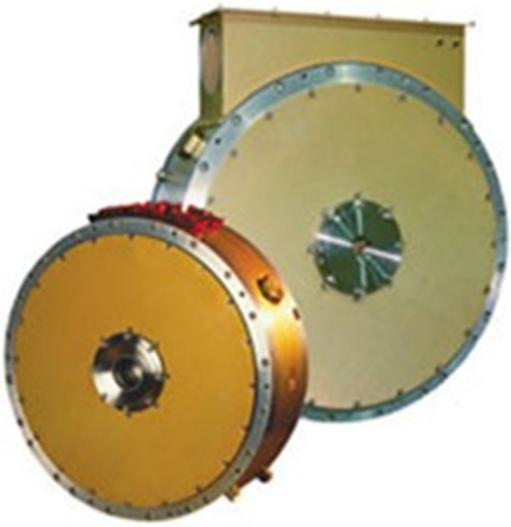

Figure 3. PA44 Single Rotor, Dual Stator 625hp Motor [5]

In [40] an alternative commercial example is presented, the 1000 horsepower PA57 which operates as both a generator and motor. The PA57 has a maximum operating speed of 4000 RPM and its maximum efficiency is 96%. The PA57 weight is 700 lbs, yielding a slightly lower 1.42 hp/lb rating.

Figure 4. PA57-1000 Single Rotor, Dual Stator PM 1000hp Generator [40]

The last commercial Reference presented is the AF-130 motor [44], [47]. The AF-130 is a motor targeted at the electric vehicle market, has a maximum operating speed of 8000 RPM and maximum efficiency of 95%. The AF-130 is rated for 89hp and weighs 62lbs, resulting in a power density of 1.43 hp/lb.

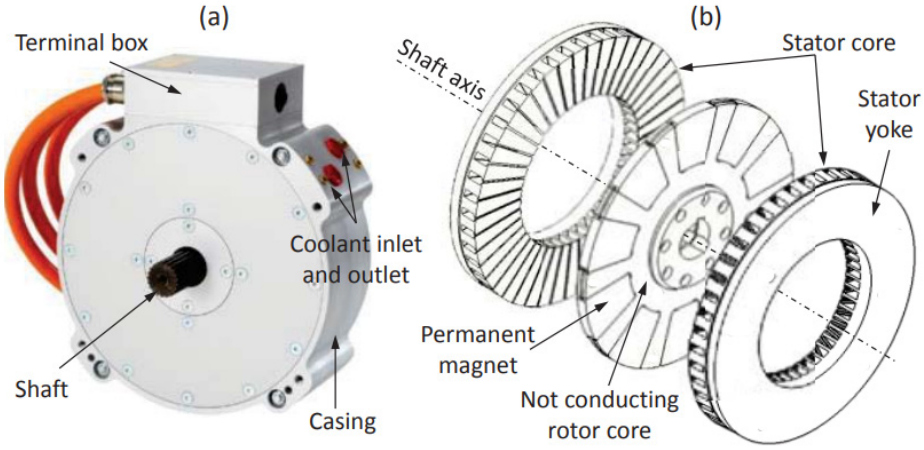

Figure 5. GKN-EVO eDrive Systems Prototype AF-130 Single Rotor, Dual Stator 89hp motor [44], [47]

While only three commercial SRDS AFPM motor examples were uncovered while reviewing literature, there were several other scientific and experimental machines unearthed. Reference [46] provides details the Army Tank-Automotive Command (TACOM) SRDS 1500 horsepower motor, developed to propel ground vehicles. The TACOM motor weighed 750 lbs and has a power density of 2 hp/lb. The TACOM motor speed and efficiency are not specified.

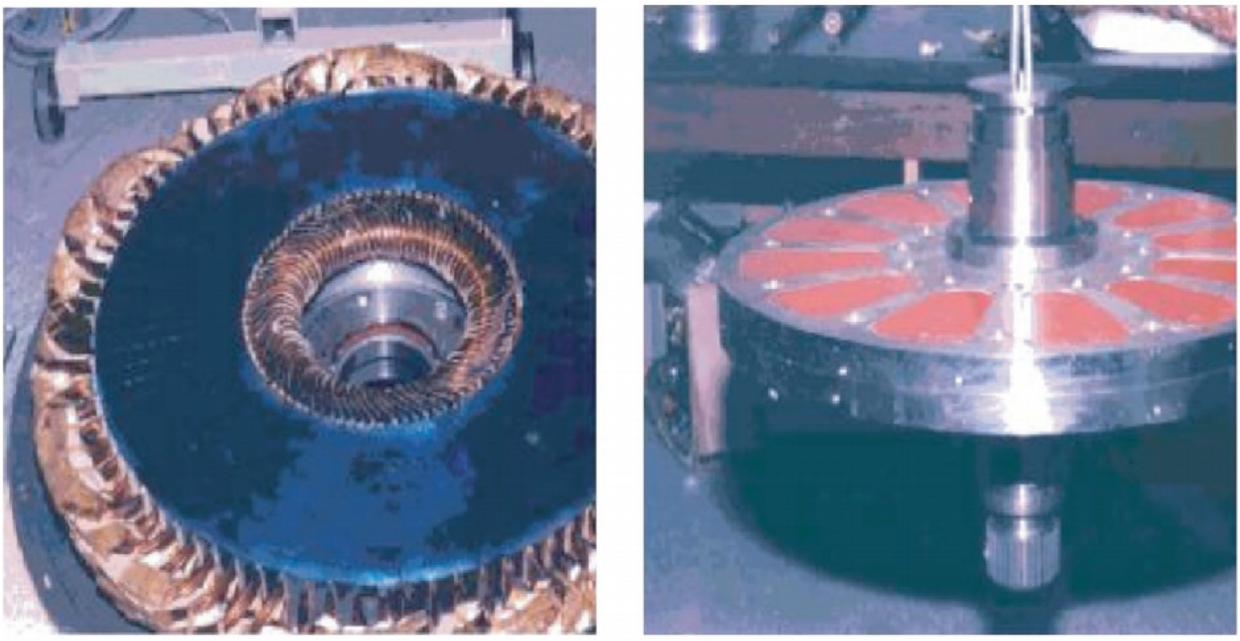

Figure 6. NASA 1500hp TACOM Motor [46]

Reference [45] presented a 130kW (174 hp), 26 RPM SRDS generator which was developed for large power direct-driven wind applications. The presented machine has an outside diameter of 1860 mm (73 in) and a predicted efficiency at rated load and speed of 93.1%, however, no overall machine weight nor maximum operational speed are provided. The focus of [45] is to address concerns of manufacturing large diameter AFPM motors and manufacturing tradeoffs which impact performance. The authors conclude that increasing the number of radial magnet segments can significantly reduce magnet eddy current and that the inclusion of welding lines on the stator tooth will reduce cogging torque when the slot opening is lower than 0.22, but will increase cogging when the slot opening is above 0.22.

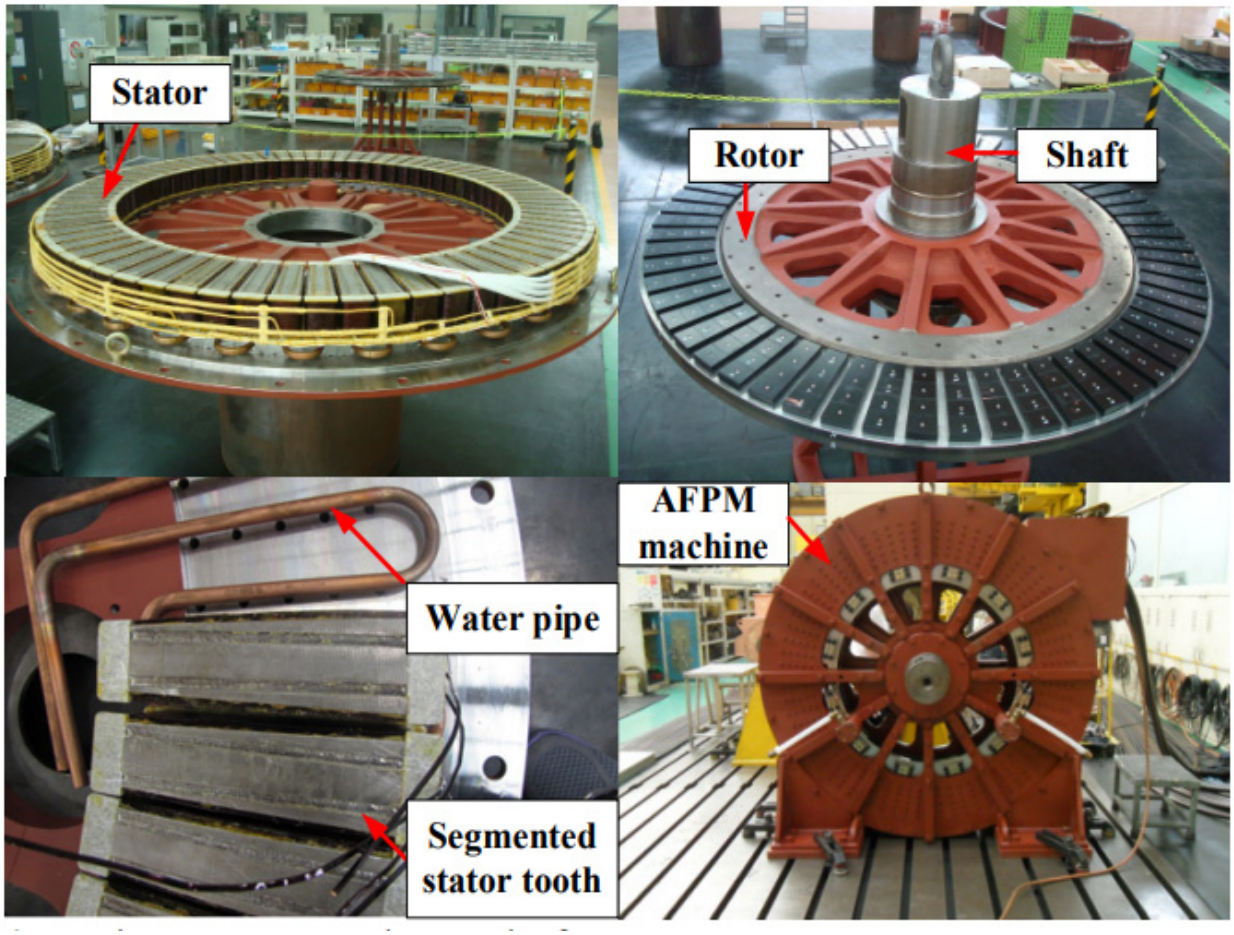

Figure 7. Large Power Direct-Driven 130kW Generator [45]

Lastly, [43] presents a 125W (0.168hp), 1000 RPM SRDS motor developed for commercial automotive and consumer goods applications. The motor efficiency was measured to be 94.1%. The motor physically measured 110mm (4.33 in) in diameter by 41mm (1.62 in) long, however maximum operational speed and weight were not reported. This paper evaluated Soft Magnetic Powder Cores (SMPC) versus more traditional 0.35mm magnetic steel and concluded that SMPCs can provide equivalent or better performance than magnetic steel while offering improvement in shaping flexibility.

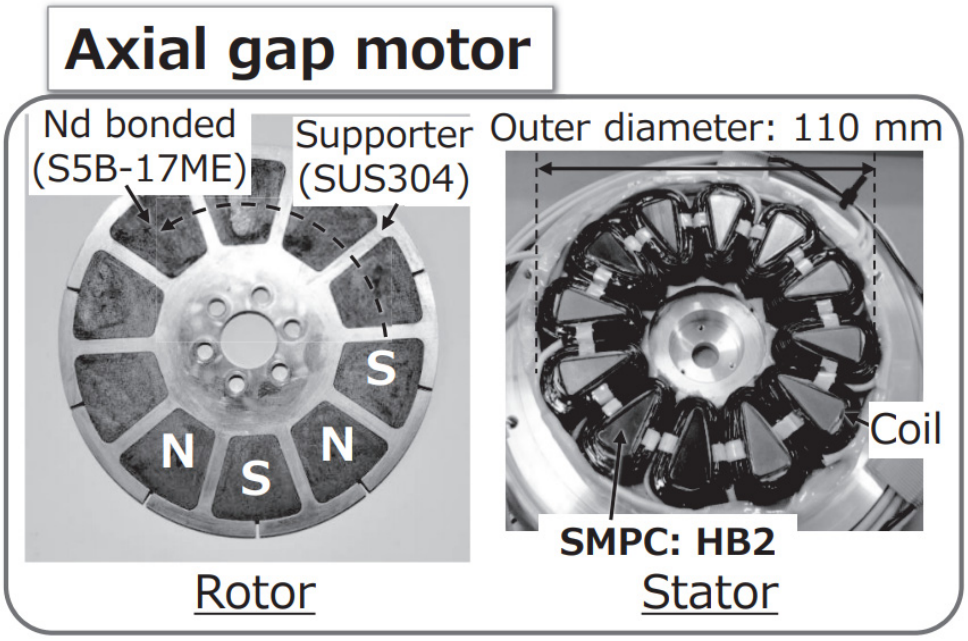

Figure 8. Sumitomo Electric Single Rotor, Dual Stator PMM [43]

Relative to a standard small industrial motor power density of 0.16 hp/lb and large industrial motor power density of 1.4 hp/lb [46], References [5], [40], [44] and [47] offer compelling evidence that SRDS AFPM motors are capable of providing superior power density. Additionally, these references offer confirmation that a SRDS AFPM can be suitable for application ranging from fractional horsepower to megawatt-class power generation.

Chapter 3

Analytical Design and Sizing of Axial Field PM Motors

At present time, FE modeling can provide accurate predictions of SRDS AFPM motor performance. While the precision of FEA cannot be matched with analytical modeling methods, the rapidness in which several motor designs can be evaluated using analytical techniques is attractive. Since an AFPM motor is inherently a 3-D problem, a quasi-2D approach is taken to help simplify the analytical modeling techniques in this chapter and follow on chapters will evaluate quasi-2D finite element modeling techniques.

This chapter will first extend the common torque density scaling method from RFPM machines to AFPM machines [11], [16]. Subsequently, an equivalent circuit model will be developed and used to predict overall machine performance and characteristics. Lastly, this chapter will review analytical inductance calculations and introduce a Fourier series based approach of prediction no-load Back-EMF for comparison against the more common classic analytical techniques [30], [38].

3.1 Permanent Magnet Motor Fundamental Concepts and Terminology

The fundamental objective of a motor is electro-mechanical power conversion. This conversion process is achieved using electrical and magnetic energy to produce forces (torques) which cause the desired mechanical motion [14]. For the case of a permanent magnet motor, the magnetic energy is harvested from permanent magnets placed on the rotor and the electrical energy is harvested from coils of wire and electrical steel which are used to create the stator.

Since all motors seek to achieve the same fundamental goal of electro-mechanical power conversion, it should not be a surprise that all motors fundamentally consist of the same two building blocks: 1) the stator and 2) the rotor. While it is true that some PM motors modify or even remove portions these basic building blocks (e.g. slotless stators, Halbach array, and embedded PM rotors, etc.) they are not the focus of this

thesis and thus are neglected for purposes of simplification. To ensure clarity and for future reference, the fundamental motor building blocks and their attributes are described below in Figure 9.

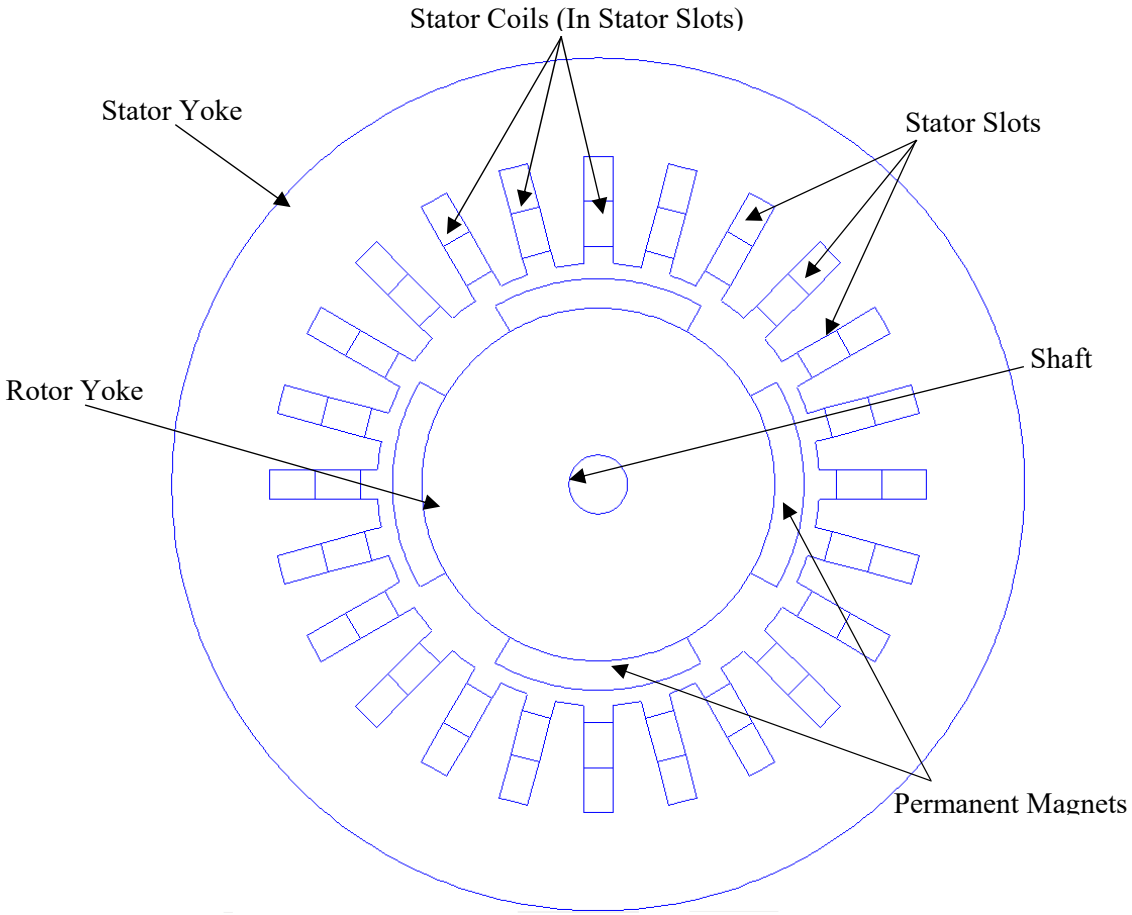

Figure 9. 2D Model of Surface Mount Radial Field Permanent Magnet Motor with Parallel Sided Slots

The overwhelming advantage PM motors possess is permanent magnet excitation. This advantage comes from the definition of permanent magnets: A permanent source of magnetic energy [field] that is not subject to failure. Of course permanent magnets can fail in cases of extreme abuse such as overheating or demagnetization through an opposing electric field, but in the author's opinion, the PMs inherent robustness and simplicity is why PM motor technology has evolved so rapidly over the last two decades.

There is a diverse selection of permanent magnets available, each with their own attributes. These attributes and related tradeoffs are not presented here, but are reviewed thoroughly in [16], [17], [20], [29], and [56]. Regardless of the PM grade selected, an overarching characteristic which allows engineers and physicist alike to harness their energy exists: all permanent magnets are dipoles. Since all PM's are dipoles, they are governed by Gauss' laws of magnetism. The integral form of Gauss' law [30] states:

$$\oint_S B \cdot dA = 0 \tag{2. 1}$$

Where S is a closed surface and dA is a vector whose magnitude is the area of an infinitesimally small portion of the surface S. Restating Gauss's law in words, the magnetic field through any closed surface must equal zero, conserving the magnetic field. A consequence of Gauss's law is that magnetic field lines form loops to and from the magnets north pole to its south pole. When a permanent magnet is supplied with a relatively low reluctance path(s), such as a ferromagnetic stator and ferromagnetic rotor, the permanent magnet's flux can be directed in such a manner that it provides useful work [power-conversion]. Figure 10 is the same surface mount PM motor as was shown in Figure 9, this time with the magnetic flux lines shown, emphasizing that magnetic field is harnessed from the magnets routed through magnetic iron to do work and is ultimately conserved.

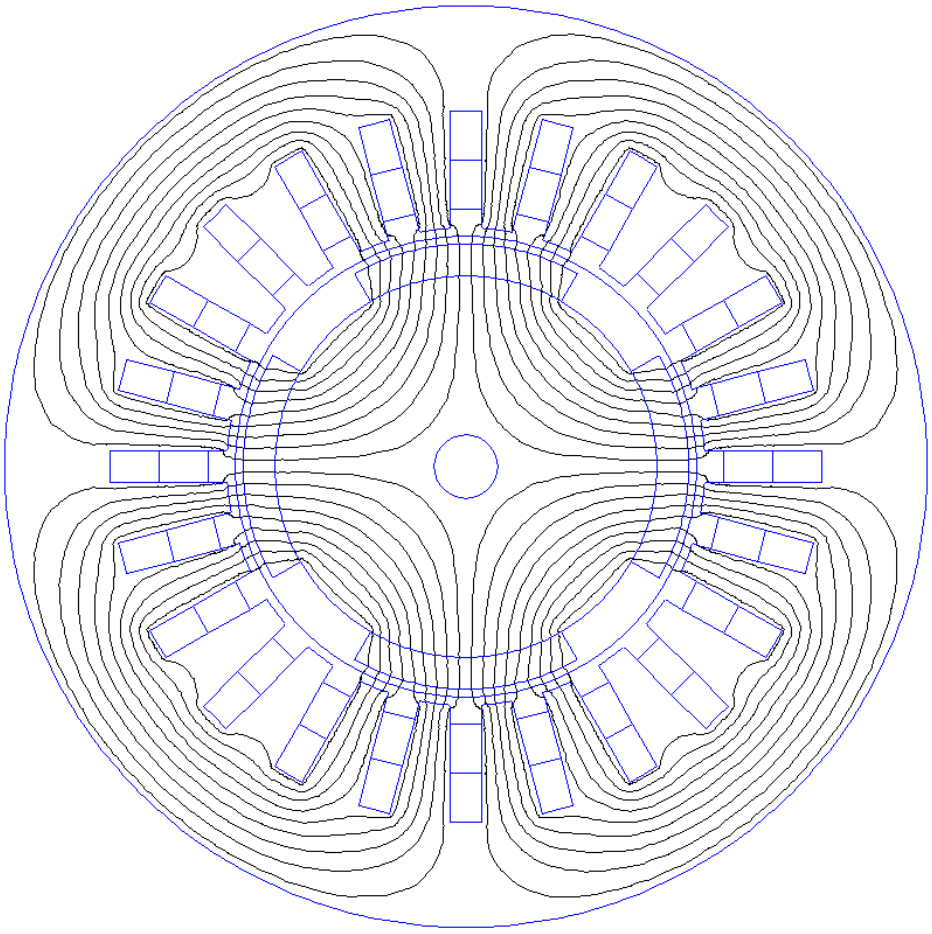

Figure 10. Flux Path in Surface Mount Permanent Magnet Motor with Parallel Sided Slots

The primary function of the magnetic rotor is to provide the energy source via permanent magnets, whereas the primary purpose of the stator is to provide electrical energy, in the form of current to the motor. These fundamental principles are the same in AFPM motors, except that flux path follows the shaft in the axial direction, rather than the radial direction. Figure 11 provides a comparison between a traditional RFPM motor and a SRSS AFPM. Figure 12 provides a 2D circumferential slice of a SRDS axial field motor clarifying the magnetic orientation of the SRDS AFPM motor under consideration in this thesis.

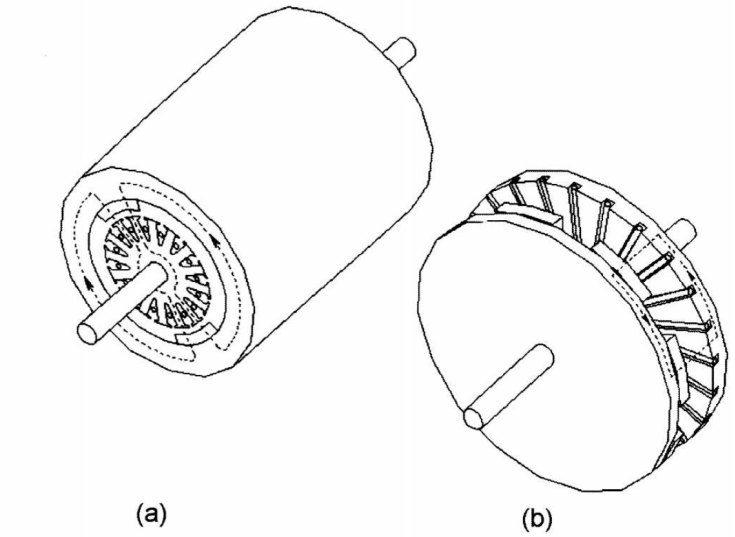

Figure 11. Topologies and Flux path of RFPM (a) and AFPM (b) motors [1]

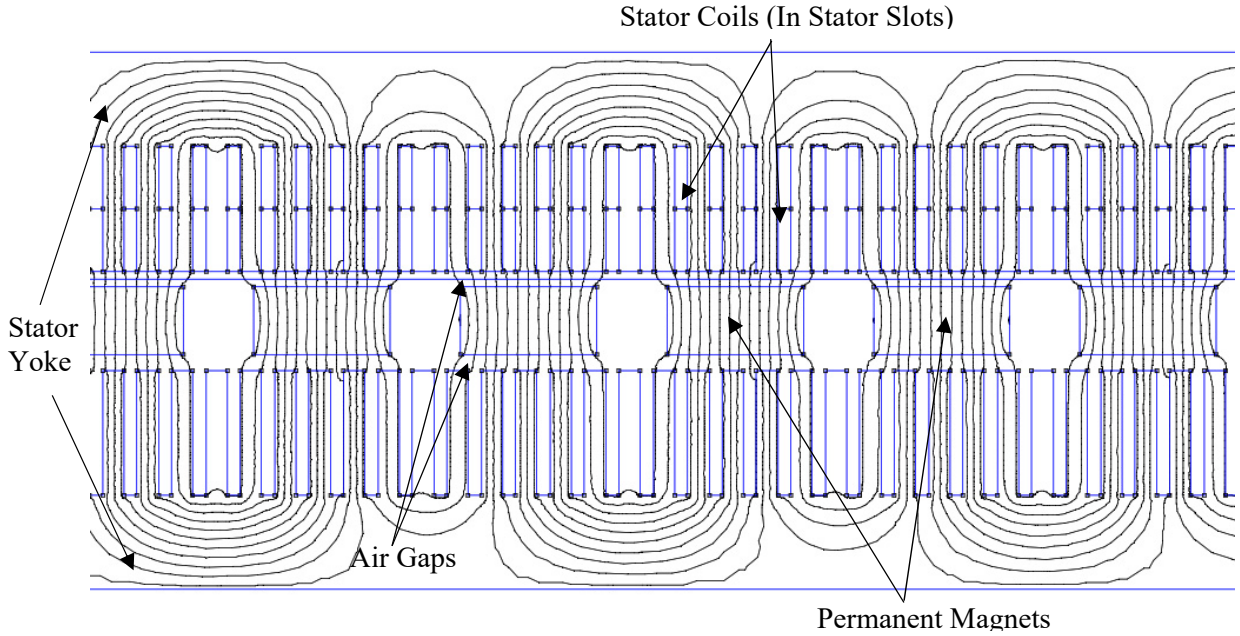

Figure 12. Circumferential Slice of SRDS AFPM (Shaft Not Shown)

From the SRDS AFPM presented in Figure 12, we can see that the magnetic field is conserved as flux circulates through the permanent magnets, across the air gap and first stator, back through the air gaps, permanent magnet, second stator and back to finally back to the magnetic source.

3.2 Initial Machine Size: Torque Density Scaling Method

The physical size of electric machines is primarily determined by its torque capability [10] and often the first question that needs to be address is how physically large a motor will be. For this reason, it is desirable to develop a method of machine sizing that does not necessitate the significant effort required to develop a circuit or finite element model.

One prominent way to estimate an initial machine size is through torque density scaling [11]. Torque density scaling allows expression of an electric machine's torque density in terms of pressure and is sometimes referred to as air gap shear stress or magnetic shear stress of the machine [11], [12]. The torque density scaling method is derived from the equations of Lorentz Force, where the force exhibited on a wire carrying current, I in a uniform magnetic field, B is expressed as:

$$\vec{F} = \vec{I}Lx\vec{B} \tag{3.1}$$

When the concept of Lorentz force is coupled with classical mechanics, a shear plane for each machine topology is observed, taking place at the center of the mechanical air gap. Figure 13 presents shear planes for three major motor topologies and includes arrows indicating the direction of the Lorentz force.

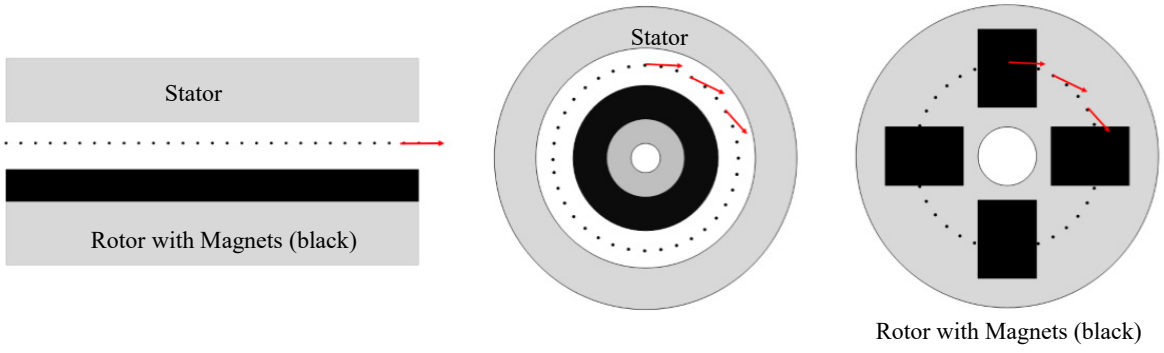

Figure 13. Linear Motor Shear Planes (Left), Radial Field Motor (Center), Axial Field Motor, Stator not Shown (Right)

From Figure 13, it is evident that a shear plane is a circumferential or linear plane over which mechanical shear stress is concentrated. In the case of shear stress, there is an inherent assumption that the mechanical

shearing forces (torques) are applied along the shear plane, with no stress acting perpendicular to the plane. For purposes of magnetic shear stress, σ, is equal to the electro-magnetic force over the plane area in units of lb/in^2 or Pascals:

$$\sigma = \frac{F}{A} \tag{3.2}$$

If we assume that the shear plane is derived from a uniformly distributed sheet of conductors with density n conductors per meter, each carrying current I and that the uniform magnetic field, B remains orthogonal to the shear plane, the linear current density A in A/m can be defined as *nI* and magnetic shear stress defined as [10]:

$$\sigma = \frac{F}{A} = BnI = BA \tag{3.3}$$

In the case of an electric machines with a rotor diameter, D, and an active magnetic stack length L the electric machines torque is described as:

$$T = F\,\frac{D}{2} = \frac{\pi}{2}\sigma D^2 L \tag{3.4}$$

Note: equation (3.4) describes the classic mechanics of a moment arm, where torque, T is produced by a moment arm and is equal to force times distance of the moment arm. Figure 14 provides an illustrative view of this electro-mechanical interaction:

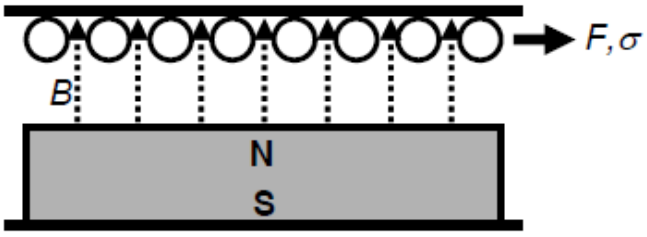

Figure 14. Force on sheet of current-carrying conductors, resulting from magnetic B-field [10]

Equations (3.2) through (3.4) outline key characteristic of a typical radial field electric machine: An electric machines torque output is proportional to the product of magnetic shear stress, σ and the rotor's volume, D^2L. Rearranging the magnetic length and diameter of a motor can be described by:

$$L = \frac{2\,T}{\pi\sigma D^2} \;\; ; \;\; D = \sqrt{\frac{2\,T}{\pi\,\sigma\,L}} \tag{3.5}$$

The same governing physics and thus underlying magneto-mechanical interactions apply to axial field motors, however geometric differences results in a different set of geometric equations and dependencies. The identities of equation (3.5) are near common-knowledge amongst the motor design community and are based on the premise of tangential force [torque] being produced over the swept rotor surface area [16], [17], described mathematically in (3.3). This theory is also applicable to axial field motors, except that the surface area which tangential force acts over must be changed to accommodate the AFPM motor configuration. A factor of two must also be added for the SRDS AFPM, as both stators equally contribute to torque production. The equation of shear stress for an SRDS AFPM motor is given as:

$$\sigma = \frac{T * (\frac{R_{ow} - R_{iw}}{2})}{2(\pi R_{ow}^2 - \pi R_{iw}^2)} = \frac{T}{\pi(R_{ow} - R_{iw})(R_{iw} + R_{ow})^2} \tag{3.6}$$

Combining these equations, with geometric design constraints and typical machines shear stress values, as presented below in Table I provides a fast, reliable method of predicting electromagnetic volume and thus size of an electric motor.

Table 1. Typical Shear Stress Values of Electric Machines [10]

Application	**Shear Stress (kPa)**
TEFC industrial motors < 1kW	0.7 to 2
TEFC industrial motors > 1kW	4 to 15
High-performance industrial servos	10 to 20
Aerospace machines	20 to 35
Very large liquid-cooled machines	70 to 100

3.3 Equivalent Circuit Model

It is well known that steady-state operation of permanent magnet motors can be accurately modeled using a speed dependent voltage source with a series inductor and resistor [9], [15], [17], [20]. The speed dependent voltage source is referred to as Back-Electromotive Force (Back-EMF or BEMF) and is a consequence of flux linking between the rotating rotor field and the stationary stator coils. The resistor and inductor in series with the voltage source represent the motor's phase impedance, values which are a result of the selected motor size, design and topology.

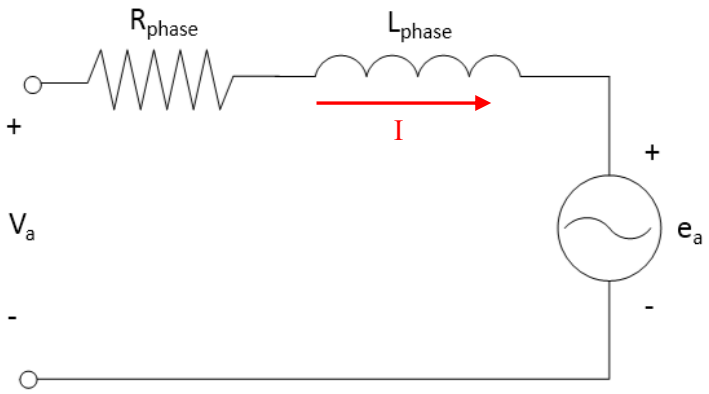

Figure 15. Single Phase Equivalent Circuit of PM Motor

In the case of a permanent magnet motor, the BEMF is directly attributed to the rotor's permanent magnets, motor geometry and rotational rotor speed. This interaction is governed by Faraday's law and is developed below in section3.3.3. The resistor and inductor of Figure 15 are lumped parameters representing a single phase of the motor. These lumped parameters are derived in sections 3.3.1 and 3.3.4 respectively.

Since the equivalent circuit is representative of a single motor phase, it can be applied to any motor with n-phases and adapted to any winding configuration (e.g. Wye, Delta, etc.). Figure 16 provides an adaptation of the equivalent circuit model for a typical 3-phase, Wye connected motor:

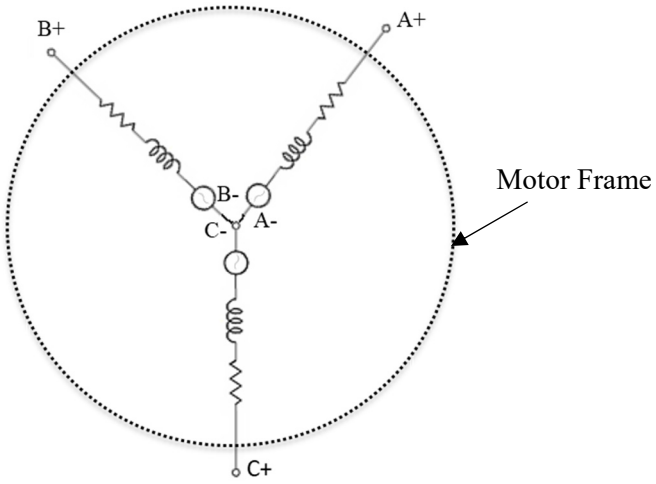

Figure 16. 3-Phase, Wye Connected Equivalent Circuit Model

3.3.1 Winding Resistance

A consequence of building an electro-magnetic power conversion device is that materials which are available must be used for construction. In most cases, this means that standard copper or aluminum conductors are used for conduction of currents and voltages within the stator. One impact of using these conductive materials is that a parasitic resistance, R_{phase} is generated through each phase winding:

$$R_{phase} = \rho \frac{L_c}{A_{cu}} \tag{3.7}$$

where ρ is the resistivity of the conductor which is a material property and is a function of temperature, L_c is the length of the stator conductor and A_{cu} is the cross sectional area of the conductor. If we assume that the conductor material is copper, the resistivity is 1.73×10^{-8} Ωm at ambient temperature, $T_0 = 20$ºC. Using the material's temperature coefficient, $\alpha = 3.8 \times 10^{-3}$, temperature can be corrected for operation temperature, T_f:

$$\rho(T_f) = \rho(T_0)[1 + \alpha(T_f - T_o)] \tag{3.8}$$

The length of the stator conductor is directly related to the stator design and encompasses a summation of in-slot coil lengths, end turn coil lengths and coil connections throughout one stator phase. The cross

sectional area of the conductor is dependent on the slot [copper] packing factor, S_{pf} of the motor as well as the number of coils per stator slot, n_{cs}:

$$A_{cu} = \frac{A_s\, S_{pf}}{n_{cs}\, n_t} \tag{3.9}$$

where A_s is the total slot area and n_t is the number of turns per stator coil.

Slot packing factor can vary from approximately 0.3 – 0.8, and is dependent on stator construction [16], [61]. The addition of slot liners and other insulating materials may limit the slot packing factor and when these additions are considered I believe this range is closer to 0.25 – 0.65. Generally distributed, random wound stators provide the lowest slot packing factor, where-as compressed, concentrated windings provide the best [16]. Slot packing factor is the ratio of conductor area, to that of total slot area:

$$S_{pf} = \frac{A_{cu}}{A_s} \tag{3.10}$$

The optimal value of slot packing factor is 1, however this is not practically feasible due to insulating materials applied to the conductors; a requirement to ensure no ground faults are present. As such, the design engineer must maximize slot packing factor, while minimizing its impacts to other salient design features

3.3.2 Winding Factors

Winding factors are used to empirically adjust motor flux linkage and consequently airgap flux density for non-uniformities associated with the construction of the motor. One of the most succinct statements clarify winding factors was written by Professor James Kirtley: *"The simplest and perhaps best definition of a winding factor is the ratio of flux linked by an actual winding to flux that would have been linked by a full-pitch, concentrated winding with the same number of turns"* [4], [9]. That is:

$$k_w = \frac{\lambda_{actual}}{\lambda_{full-pitch}} \tag{3.11}$$

There are three winding factors which are commonly specified by design engineers, winding pitch factor, k_p, winding distribution, or winding breadth factor, k_b and winding skew factor, k_n [1], [4], [9], [35], [36], [37], [42]. Combining these three winding factors, the overall motor winding factors is expressed as:

$$k_w = k_p k_b k_n \tag{3.12}$$

Each of these winding factors offers insight as to how the motor's MMF is impacted by spatial changes in the motor design and are well-established industry terms [1], [4], [9], [35], [36], [37]. Since these winding factors are of particular importance when predicting overall motor performance, the following sub-sections will methodically walk through the definition of each winding factor.

3.3.2.1 Winding Pitch Factor for Integral Slot-Pole Windings

Winding pitch, α refers to the angular displacement between coil sides in the stator. Coil pitch is expressed in electrical radians, where 2π electrical radians are equal to the mechanical angle over a full rotor pole pair. A coil is said to be "short-pitched" when its pitch angle is less than π radians, and "long-pitched" when the pitch angle is greater than π radians [34].

Practically, most motors are short-pitched as the benefits of long pitch are equivalent to short pitching. However, relative to a short-pitched winding, long-pitched windings will incur a larger resistance penalty due to the longer end turns required to make the coil long-pitched [34]. Figure 17 depicts a 2-pole motor with short-pitched stator coils.

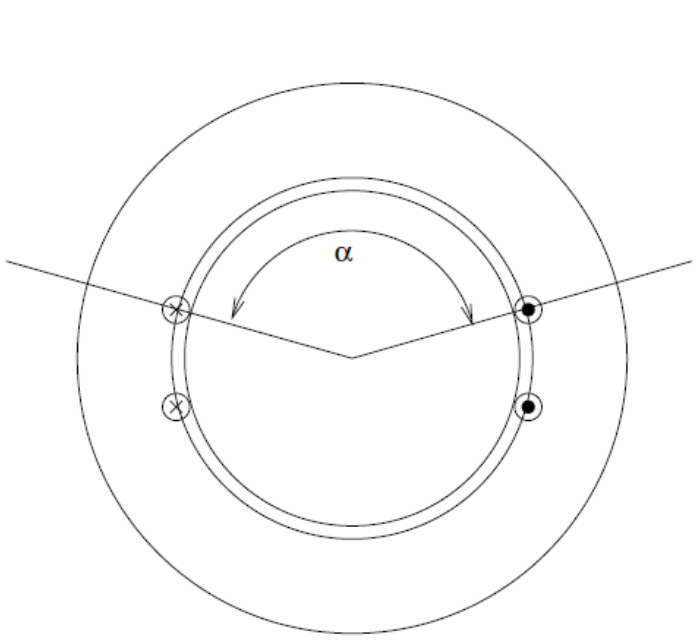

Figure 17. Winding Pitch for a 2-pole motor with short-pitched coils [4]

The general form of winding pitch factor for any n-harmonic is:

$$K_p = sin\frac{n\pi}{2}\ sin\frac{n\alpha}{2} \tag{3.13}$$

When developing an equivalent circuit model for an integral slot-pole permanent magnet motor, only the case of fundamental winding pitch factor need to be considered and the equation simplifies to:

$$K_p = \left|\sin\frac{\alpha}{2}\right| \tag{3.14}$$

3.3.2.2 Winding Distribution Factor for Integral Slot-Pole Windings

Winding distribution, or breadth factor is employed to account for intra-phase winding coils which link flux slightly out of phase from each other due to spatial positioning the coils. While at first this sounds like an undesirable effect, it is a knob of key importance in motor design and has similar impacts as coil pitch. Coil pitch and breadth can be used by the design engineer to transform a back-EMF waveform from trapezoidal to sinusoidal. Winding distribution factor is given as:

$$K_b = \frac{sin\frac{nm\gamma}{2}}{m\,sin\frac{n\gamma}{2}} \tag{3.15}$$

where m refers to the number of slots per rotor pole, per motor phase and γ is the slot pitch angle in electrical radians for integral slot-pole motors. m and γ are described by the following equations and the slot pitch angle is depicted in Figure 18.

$$m = \frac{N_s}{2PP\,Q}, \qquad \gamma = \frac{2\pi PP}{N_s} \tag{3.16}$$

where Q is the he number of motor phases, PP is the number of rotor pole pairs and Ns is the number of stator slots.

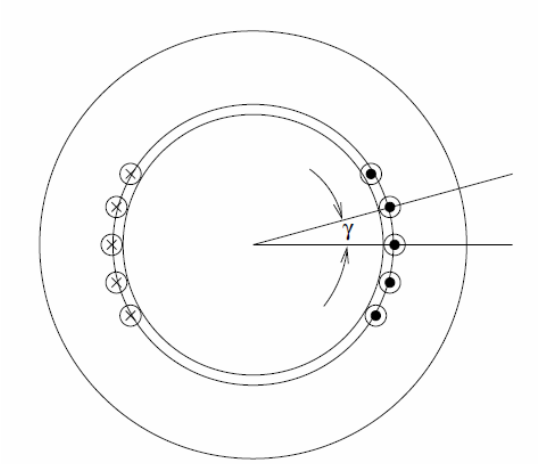

Figure 18. Slot pitch angle for single phase, 2-pole motor, m=5 [4]

Similar to the case of winding pitch factor, only the fundamental component of winding breadth factor needs to be considered for use in the integral slot-pole motor equivalent circuit model. This simplifies the expression of winding breadth factor to:

$$K_b = \frac{sin\frac{m\gamma}{2}}{m\,sin\frac{\gamma}{2}} \tag{3.17}$$

It is important to note that equations (3.15) – (3.17) are only valid for motors featuring integral-slot pole combinations. This is because the stator winding function of integral slot-pole motors features the same period as the rotor poles; whereas fractional-slot motor windings do not share the same period as the rotor [38]. In the case of fraction-slot motors, a more classical space vector or Fourier Series approach must be used to determine the winding distribution factor [7], [38], [71], [72].

3.3.2.3 Winding Skew Factor

Winding skew factor, K_n is intended to correct for instances when the stator slot is intentionally misaligned during the assembly process. The winding skew factor is given as:

$$K_n = \frac{sin(n\,\alpha_{skew}/2)}{n\,\alpha_{skew}/2} \tag{3.18}$$

where α_{skew} is the skew angle in radians. Similar to the case of breadth and pitch factor, the fundamental component is again only used for the equivalent circuit model, simplifying the winding skew factor to:

$$K_n = \frac{sin(\alpha_{skew}/2)}{\alpha_{skew}/2} \tag{3.19}$$

3.3.3 Back Electromotive Force

All PM machines, including the SRDS AFPM motor, are unique in that they do not require external excitation to produce a speed dependent voltage source. This speed dependent voltage source is the motor's back-EMF and is a signature characteristic of a PM motor which is governed by Faraday's Law. Faraday's Law states that electromotive force, ε [volts], is given by the time rate change of magnetic flux, Φ:

$$\varepsilon = -\frac{d\Phi}{dt} \tag{3.20}$$

If we consider the case where magnetic flux is linked using N conductors and the identity Φ = BA, Faraday's expands to:

$$\varepsilon = -\frac{d\mathrm{NBA}}{dt} \tag{3.21}$$

The area and flux density being described by Faraday's law are the same as were designated when deriving Lorenz force in section 3.2. As such area, A is defined by the active length multiplied by the airgap circumferential length, x, in meters. If we incorporate these common terms and drop the negative, which indicates the voltage phase, BEMF voltage can be expressed as:

$$\varepsilon = NBL_{st}\frac{dx}{dt} \tag{3.22}$$

where dx/dt is equal to the linear velocity, in meters per second, of magnetic flux passing the armature conductors, B is the peak value of airgap flux density and N is the number of conductors per phase.

In the case of a radial field motor, the linear velocity of flux is observed at the stator inside radius, where the flux is linked to the stator coils. In the case of an axial field motor, flux linkage is still occurring at the coils, however, the coils are spatially positioned along the radial direction. This spatial positioning of coils means that the linear velocity of flux is changing as the coil transverse the radial direction. In order to account for this, the linear velocity must be observed at that the average working radius, Rs.

It's important to note that N conductors are the number of series turns per phase, and T_{ph} multiplied by two. This factor of two is because all stator coils have 2 active coil sides, both linking flux and consequently producing Back-EMF voltage.

$$\varepsilon = 2T_{ph}B_{pk}L_{st}\frac{dx}{dt} \tag{3.23}$$

B_{pk} is the peak value of the normal component of airgap flux density, which is described as:

$$B_{pk} = \frac{B_r}{1+\mu_r\frac{g'}{H_m}} \tag{3.24}$$

where Br is the remnant or residual flux density of the permanent magnet, μ_r is the recoil permeability of the magnet, H_m is the magnet height in the direction of the airgap and g' is the airgap length modified by the Carter's Coefficient, Kc [13]:

$$K_c = \left[1 - \frac{1}{\frac{\tau_s}{\omega_s}\left(5\,\frac{g}{\omega_s} + 1\right)}\right]^{-1} \tag{3.25}$$

where τ_s is the pitch length of a slot and tooth, ω_s is the slot width and g is the physical airgap of the motor.

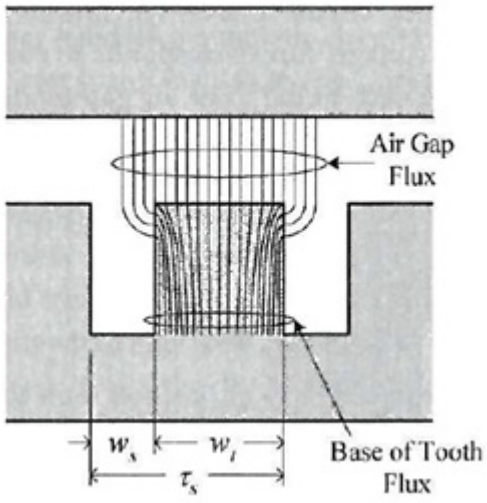

Figure 19. Visualization of Carter Coefficient. [13]

Carter's coefficient can now be used to calculate the equivalent airgap of the permanent magnet motor, g'. For the case of a standard radial field permanent magnet motor there is only one airgap in the reluctance path, and g' is given by:

$$g' = gK_c \tag{3.26}$$

In the case of a SRDS AFPM, the equivalent reluctance path has two airgaps. This introduces a factor of 2 into the equation and the equivalent airgap is described by:

$$g' = 2gK_c \tag{3.27}$$

Now that the equivalent airgap is known, the peak value of the airgap flux density for a SRDS AFPM machine is expressed as:

$$B_{pk} = \frac{B_r}{1 + \mu_r \frac{2gK_c}{H_m}} \tag{3.28}$$

and the Series Number of Turns per phase, Tph is given as:

$$T_{ph} = \frac{N_s N_{cs}}{2 Q} \tag{3.29}$$

3.3.4 Phase Self Inductance

Similar to the case of winding resistance, winding inductance is a byproduct of stator construction. While winding inductance can be considered parasitic in nature, it acts as a first order filter for pulse-width modulated voltages. This filtering effect is due to inductance's inherent role in the motor time constant, therefore regulating the rate at which phase current can change with respect to time [13]. While phase inductance has a positive filtering effect, it can also negatively impact motor power factor.

When a motor is under heavy load and armature currents are highest, phase inductance will act to pull the motor power factor down. For all aforementioned reasons it is important to define a method which characterizes a PM motors phase inductance without the burden of running a detailed finite element model. According to [13], [17], phase inductance is the summation of the air gap inductance, the slot leakage inductance and end turn inductance:

$$L_{phase} = L_g + L_s + L_e \tag{3.30}$$

where Lg is the air gap component of the phase inductance, Ls is the slot leakage component of phase inductance and Le is the end turn portion of phase inductance.

3.3.4.1 Air Gap Inductance

From [13] an expression for the air gap component of a PM motor's inductance is derived as:

$$L_g = \frac{\lambda}{i} = \frac{N_m n_m^2}{\Re_g + \Re_m} \tag{3.31}$$

where λ is magnetic flux, i is current, N_m is the number of magnetic rotor poles, n_m is the number of turns per coil, $\Re_g$ is the air gap reluctance and $\Re_m$ is the magnet reluctance. Studying (3.31), we can see that this simply describes the inductance of a typical C-Core inductor with two air gaps, multiplied by N_m inductors in series:

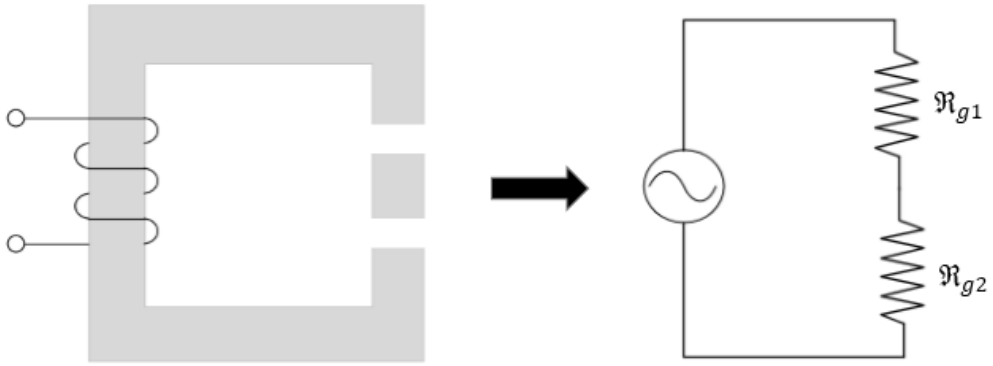

Figure 20. Two Air Gap C-Core and Corresponding Magnetic Circuit Diagram

In the case a permanent magnet motor, air gap fringing and the permanent magnets recoil permeability must be taken into account. These additions result in a marginal modification to the C-Core and reluctance diagram arrangement:

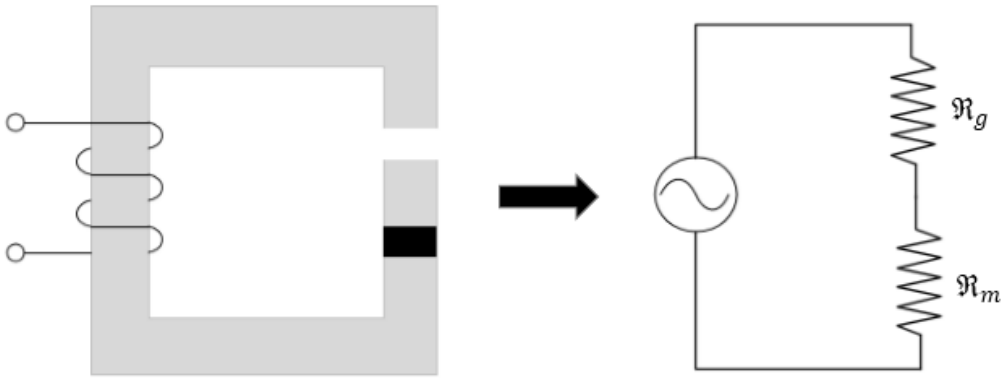

Figure 21. Two Airgap C-Core with Permanent Magnet (black) Replacing One Airgap

The factor Nm presented in (3.31) inherently implies that all motor coils in a single phase are in series with one another. This simplification will be maintained throughout the remainder of this thesis, however that is not a strict requirement of motor construction. This method can be applied to any motor topology to determine the air gap component of inductance. Below, Figure 22 depicts application of this methodology to the 4-pole, 3-phase radial field motor presented in earlier in Figure 9, neglecting the marginal saliency provide by discrete magnets:

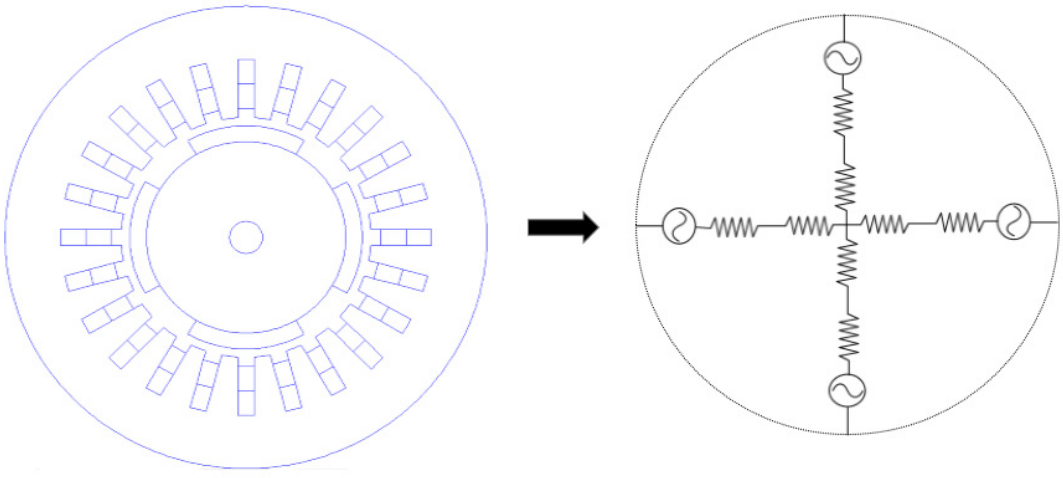

Figure 22. 4-Pole Radial Field PM Motor and Resulting Magnetic Circuit Model

Using the identities of magnet reluctance, air gap reluctance and air gap area we can calculate the air gap component of a radial field motor's inductance. Similar to C-Core magnetic circuit analysis, the equations of reluctance are given as [13]:

$$\Re_m = \frac{H_m}{\mu_r \mu_0 A_m} \tag{3.32}$$

$$\Re_g = \frac{g'}{\mu_0 A_g} \tag{3.33}$$

where A_g is the air gap area and Am is area of the magnet in the reluctance path. For a radial field motor, these are given as:

$$A_{g\_radial} = L_{st}\theta_{st}R_{ro} = \left(2\pi/_{N_m}\right) L_{st}R_{r0} \tag{3.34}$$

$$A_{m\_radial} = L_{st}\theta_{st}R_{ro}m_{frac} = \left(2\pi/_{N_m}\right) L_{st}R_{r0}m_{frac} \tag{3.35}$$

where m_{frac} is the fractional portion of a magnet in the motor, relative to a full pitch magnet ($0 > m_{frac} < 1$). Combining (3.31) through (3.35) the air gap component of phase inductance for a radial field motor is:

$$L_{g\_radial} = \frac{2\pi\mu_0 L_{st}R_{ro}}{g' + \frac{H_m}{\mu_r C_\varphi}}\, n_m^2 \tag{3.36}$$

where C_φ is the flux concentration factor, $C_\varphi = A_m/A_g$. If we assume that $A_g \approx A_m$ this equation simplifies to:

$$L_{g\_radial} = \frac{2\pi\mu_0 L_{st}R_{ro}}{g' + \frac{H_m}{\mu_r}} n_m^2 \tag{3.37}$$

where R_{ro} is the inside radius of the stator, Lst is the active length of the air gap, g' is the equivalent air gap, including the effects of Carter's Coefficient, Hm is the magnet radial height, μr is the magnet relative

permeability and n_m^2 is the number of turns per slot squared. This air gap component of inductance, (3.37) matches the classical winding function based definition of phase self-inductance [17], [30], [34]:

$$L_{AA} = \frac{\mu_0 r l}{g} \int_0^{2\pi} N(\theta)^2 \, d\theta \tag{3.38}$$

However, the objective of this thesis is not to analyze a radial field motor, and thus (3.37) must be modified to accommodate the axial-configuration. To accommodate an axial field machine, the equation of air gap area must be adjusted to account for the axial motor geometry:

$$A_g = \left(\pi R_{ro}^2 - \pi R_{ri}^2\right) \Big/ N_m \tag{3.39}$$

Combining this new definition of air gap area and again assuming $A_g \approx A_m$ the air gap component of an axial field motor's inductance is:

$$L_g = L_{g\_axial} = \frac{\mu_0 n_m^2 \left(\pi R_{ro}^2 - \pi R_{ri}^2\right)}{g' + \frac{H_m}{\mu_r}} \tag{3.40}$$

3.3.4.2 Slot Leakage Inductance

With the air gap component of inductance determined, we now focus our attention to deriving an expression for the slot leakage component of air gap flux density. Slot leakage inductance is a result of coil currents in the slot producing a magnetic field that crosses from one side of the slot to the other, in addition to the flux being driven across the air gap [17]. This magnetic field seems a bit odd until one realizes that the magnetic field is circulating around the slot conductors, following the right-hand rule [13]. Slot leakage field, H is depicted below:

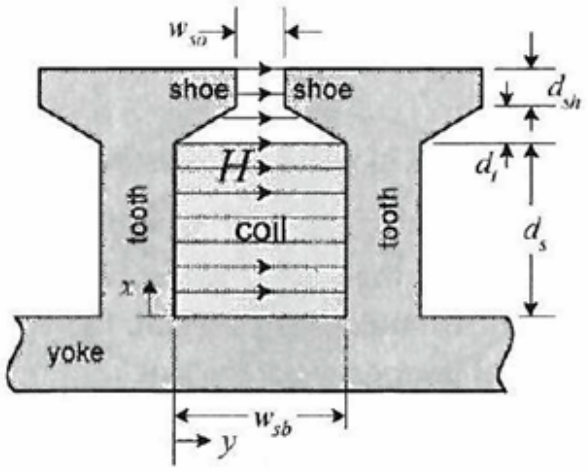

Figure 23. Slot Leakage Flux [13]

Computation of the slot leakage component of inductance is complicated by the fact that magnetic flux linking the coil is not constant over the cross section of the coil, but rather it is approximately linear with respect to slot depth [13]. Several authors have outlined methods for calculation of slot leakage inductance through the utilization of permeance functions to account for this non-uniform distribution [17], [18], [19]. The general form of slot leakage inductance for a single rectangular slot, L_{sr} is:

$$L_{sr} = \mu_0 L_{st} N^2 P \tag{3.41}$$

where P is the slot permeance coefficient and is a function of slot height, width and shape as well as the distribution of the copper conductors within the slot. For the case of a rectangular slot, the permeance will be at its highest when the coil conductors are crowded at the bottom of the slot and the permeance will be its least when all the coil conductors are crowded at the top of the slot, closest to the motor air gap [17]. For these reasons, slot permeance coefficients exist, which are normalized to the ratio of slot height to slot width. These coefficients are presented in Figure 24.

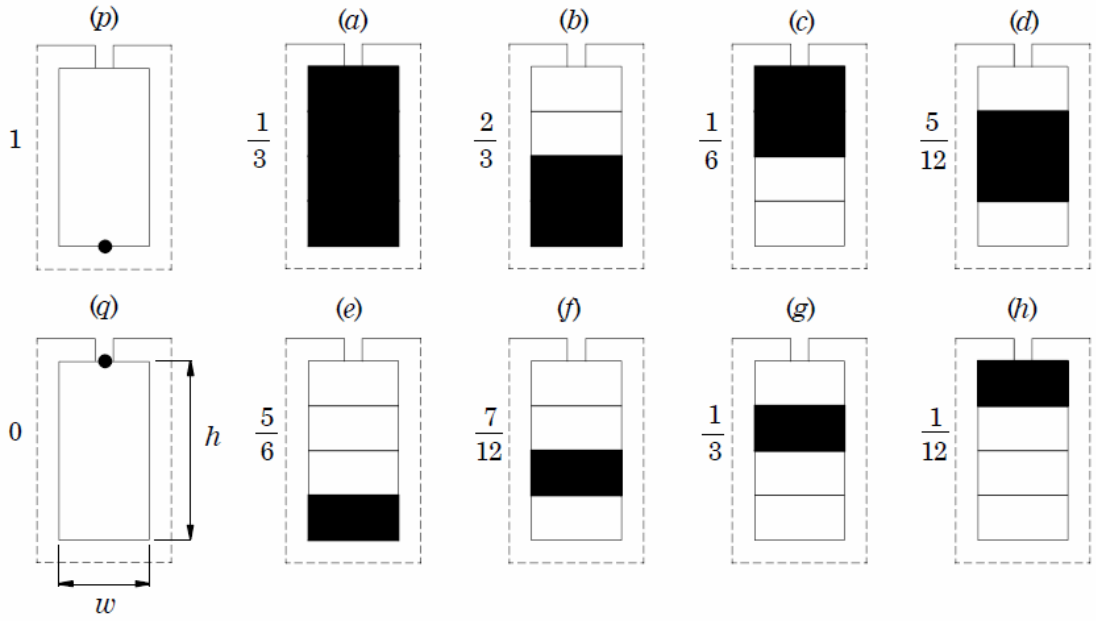

Figure 24. Slot Permeance Coefficients [17]

If we assume that the coils are evenly distributed throughout a rectangular slot, the normalized permeance coefficient is 1/3. Combining this coefficient with generalized expression for permeance, P and equation (3.41) the general expression of slot leakage inductance is:

$$L_{sr} = \frac{1}{3}\frac{\mu_0 L_{st} H_s N^2}{W_s} \tag{3.42}$$

where W_s is the width of the slot, H_s is the height of the slot and L_{st} is the active length of the motor. The last step in calculating the slot leakage component of inductance is to account for all of the slots in each of the motor stators. Assuming that all of the motor coils are wound in series, Slot Leakage inductance is given by:

$$L_s = \frac{1}{3}\frac{\mu_0 L_{st} H_s n_m^2 N_s}{P\, W_s} \tag{3.43}$$

While this equation is often a very good starting point, its utility increases by leaving the permeance coefficient as a variable and selecting the appropriate permeance coefficient from Figure 24:

$$L_s = P \frac{\mu_0 L_{st} H_s n_m^2 N_s}{P W_s} \tag{3.44}$$

3.3.4.3 End Turn Leakage Inductance

End turn leakage inductance is the last component of phase inductance that needs to be accounted for. This component of inductance is created from the magnetic field that surrounds the stator coils after it leaves one slot, but before it enters another. [13] develops a method of calculating radial field motor end turn inductance, which assumes the end turns are semicircular, allowing the use of a co-energy relationship for estimating end turn leakage inductance. Figure 25 presents the geometry assumption used in [13], (3.45) and (3.47).

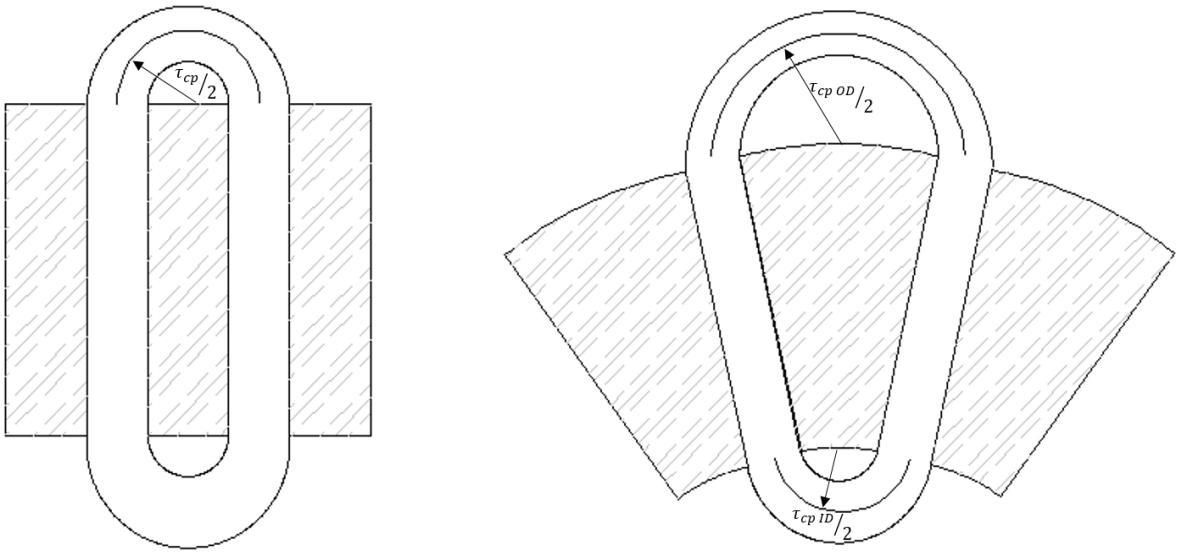

Figure 25. RFPM Motor Coil End Turn Geometry Assumption (Left), AFPM Coil End Turn Geometry (Right)

For the case of a radial field motor, where end turn geometry can be assumed symmetrical on both ends of the stator core, end turn inductance is given as:

$$L_{e1} = \frac{N_m \mu_0 \tau_{cp} n_m^2}{2} ln\left(\frac{\tau_{cp}\sqrt{\pi}}{\sqrt{2\,{}^{A_s}/_{CPS}}}\right) \tag{3.45}$$

where CPS is the number of coils per slots (e.g. 1, 2…) and τ_{cp} is the circumferential length of the end turns and is a function of the motor geometry described in Figure 25. In the case of a multi-pole motor, the coil end turns will bridge multiple slots, thus the Ns/P term has been added to account for this:

$$\tau_{cp} = \left(\frac{2\pi R_{avg}}{N_s}\right)\frac{N_s}{P} \tag{3.46}$$

As seen in Figure 25, there are slight geometric differences in an axial field motor vs. a typical radial field motor, of primary interest is that a different slot pitch exists at the top and bottom of the stator. To account for this difference, an average circumferential end turn length needs to be calculated and applied to equation (3-45):

$$\tau_{cp} = \left[\frac{\left(\frac{2\pi R_{ro}}{P}\right) + \left(\frac{2\pi R_{ri}}{P}\right)}{2}\right] \tag{3.47}$$

3.3.5 Overall Machine Efficiency

There are multiple sources of power loss in electric machines. Each of these motor loss mechanisms is a consequence of using non-ideal materials during construction (e.g. steel, copper, etc.) as well as impacts related to the dynamic motion of the motor. Generally, losses can be broken out into the following categories: 1) I^2R Losses 2) Core Losses 3) Rotational Losses and 4) Stray losses. Eddy Current losses in the magnets as well as PWM induced losses can also be present, but are not considered in this thesis. Each of the considered loss mechanisms will be characterized in the following sub-sections.

3.3.5.1 I^2R Losses

I^2R losses are a well understood and fundamental loss mechanism which occurs in all current carrying mediums. As the name implies these losses are proportional to the phase current squared multiplied by the phase resistance:

$$W_{I^2R} = I^2R \tag{3.48}$$

where R is the phases resistance provided by equation (3.7) and I is the motor RMS phase current. Phase current is proportional to the torque provided by the motor and the air gap flux density. Taking advantage of our earlier calculations of air gap flux density as well back-EMF, phase current is calculated as:

$$I = \frac{P}{2Q\frac{\varepsilon}{\sqrt{2}}} \tag{3.49}$$

where P is shaft power in Watts, Q is the number of phases per stator, ε is BEMF voltage provide by equation (3.23), the factor of 2 comes from the fact that there are two stators generating torque in a SRDS AFPM and the factor of square root of two is converting back-EMF to RMS so that Current is provided in RMS and assumes a sinusoidal back-EMF waveform. If the motor has significant harmonic distortion, such as Brushless DC motors, this Crest, or Waveform factor [55], [63] must be replaced with the appropriate value corresponding to the motor design.

3.3.5.2 Core Losses

Core losses are a consequence of using magnetic steels in the presence of a time varying magnetic field. In the case of the SRDS AFPM machine being analyzed in this thesis, there are no magnetic steels used in rotor construction and core losses will be limited to stator steel.

Core losses are the result of hysteretic and eddy-current losses in magnetic material. For a specific core material core losses can be generally expressed as [17]:

$$W_{core} = W_h + W_e = C_h f B^n + C_e B^2 f^2 \tag{3.50}$$

where variables C_e, C_h and n are empirically derived material properties, which are specific to the selected core material and thickness and are typically less than 1, f is electrical frequency and B is the peak value of flux density in the loss generating magnetic material. As can be seen from this relationship, the hysteretic component of losses is proportional to frequency multiplied by a small constant value; whereas the eddy current component of core loss is proportional to the square of both flux density and frequency. When the fundamental electrical frequency is high (>1 kHz) it is often said that eddy-current losses are proportional with the square of operational frequency and the square of air gap flux [17]:

$$W_{core} \propto C_e B^2 f^2 \tag{3.51}$$

While coefficients for equations (3.50) and (3.51) could be analytically derived for any material and thickness, the nature of hysteric and eddy current losses may lead to inaccuracies. In response to these inaccuracies and consumer demand, magnetic steel suppliers have addressed this concern by suppling empirically derived core loss characteristic data. Supplier core loss data is often supplied in table or curve form and provides the engineer with a core loss rate in watts per pound of steel vs. magnetic induction. Figure 26 presents core loss characteristic for M-10X, 0.35mm, non-grain oriented electrical steel provide by AK Steel Corporation.

Flux Density (kG)	D-C Field Strength (Oe)	Core Loss W/lb. – ASTM A343 and A348 50/50 Samples As Sheared								
		50	60	100	200	400	600	1000	2000	2500
1.0	0.241	0.00606	0.00764	0.0142	0.0360	0.0991	0.186	0.425	1.34	1.95
2.0	0.334	0.0249	0.0311	0.0581	0.146	0.393	0.724	1.604	4.87	6.95
3.0	0.417	0.0526	0.0656	0.124	0.310	0.838	1.535	3.37	10.0	14.3
4.0	0.467	0.0869	0.109	0.206	0.521	1.407	2.57	5.64	16.6	23.6
5.0	0.538	0.127	0.159	0.303	0.770	2.09	3.84	8.43	24.9	35.5
6.0	0.646	0.171	0.215	0.411	1.058	2.89	5.33	11.8	35.1	50.3
7.0	0.671	0.220	0.276	0.533	1.382	3.82	7.06	15.7	47.8	68.7
8.0	0.764	0.274	0.344	0.668	1.745	4.86	9.07	20.4	63.0	91.7
9.0	0.886	0.334	0.419	0.817	2.15	6.05	11.4	25.8	81.2	119
10.0	1.035	0.400	0.504	0.982	2.60	7.39	14.0	32.2	103	151
11.0	1.269	0.475	0.597	1.166	3.10	8.91	17.0	39.6	129	190
12.0	1.689	0.561	0.705	1.381	3.68	10.7	20.5	48.3	162	238
13.0	2.77	0.670	0.839	1.639	4.36	12.7	24.5	59.0	200	295
14.0	5.28	0.812	1.020	1.981	5.23	15.1	29.4	70.8	245	366
15.0	17.3	0.990	1.238	2.39	6.22	18.1	35.3	86.7		
16.0	42.3	1.171	1.455	2.81	7.21	20.9				
17.0	86.2	1.340	1.655	3.18	8.19	23.7				

Figure 26. M-10X Electrical Steel, Core Loss Rate Table [62]

As can be seen from Figure 26 core loss data is only supplied at discrete induction levels and frequencies. Magnetic steel suppliers will often offer testing services for additional frequencies or induction levels, but this is generally an expensive proposition. To effectively apply these core loss data sets the design engineer must use the data sets and interpolate or correlated a characteristic equation such as (3.50).

3.3.5.3 Rotational Losses

Rotational losses consist of mechanical frictional, windage and ventilation losses. Frictional losses are the result of bearing friction, where-as windage losses are the result air interaction with the rotating rotor and stationary stator inside of the motor and ventilation losses are the result of shaft mounted fans.

$$W_{rot} = W_{fr} + W_w + W_v \tag{3.52}$$

where W_{fr} is the frictional component of losses, W_w is the windage component of losses and W_v is the ventilation component of losses. For the axial field machine design under consideration, there will be no rotor mounted fan and thus the ventilation component of losses is assumed to be zero. The remaining

portions of rotation losses are non-linear by nature and often difficult to calculate accurately without conducting a very detailed analysis. As such, there are several empirically derived methods for estimating these losses [26]. For the axial field motor under consideration, equation (3.53) will be used to characterize rotational losses within the motor:

$$W_{rot} = 0.06 n_r k_{fb}(m_r + m_{sh}) + .5 C_f \rho (2\pi n_r)^3 \left(R_{ow}^5 - R_{sh}^5\right) \quad (3.53)$$

where n_r is the rotational shaft speed in rev/sec, k_{fb} is a windage factor assumed to be equal to 2 [26], m_r is the rotor assembly mass, including magnet mass in kilograms, m_{sh} is the shaft mass, ρ is the density of air in kg/m^2, R_{sh} is the shaft radius in meters and C_f is a coefficient of drag given by:

$$C_f = \frac{3.87}{Re^{0.5}} \quad ; \quad Re = \frac{2\pi n \rho R_{out}^2}{\mu} \quad (3.54)$$

where μ is the dynamic viscosity of air in Pa-S and Re is the calculated air-flow Reynold's Number.

3.3.5.4 Stray Losses

Stray losses are the result of high frequency losses in the core of AC machines which are the result of high order winding space and slot harmonics. Calculation of stray losses is difficult and inaccurate; thus such stray losses are often expressed as a small percentage of machine power which increases as machine power increases [27]. For the axial field motor under consideration in this thesis stray losses will be characterized as:

$$W_{str} = 0.005 * P \quad (3.55)$$

3.4 Analytical No-Load Waveform Prediction

When designing a new permanent magnet motor, it is desirable to understand the motor's airgap flux density and ultimately back-EMF characteristics. Quantifying these attributes is often time-consuming and resource intensive, which is not conducive during the early phases of machine design. This thesis presents an analytical model with respect to electrical angle of the rotor utilizing classic Fourier Series techniques

to represent an idealized, normal component of airgap flux density. The normalized component of airgap flux density is then used to develop a back-EMF model leveraging classical winding factors.

3.4.1 Idealized Air Gap Flux Density

If we consider that a SRDS AFPM magnet motor can be unwrapped to form a linear equivalent of itself the idealized, normal component of the air gap flux distribution for a motor with non-continuous permanent magnets is shown in Figure 27.

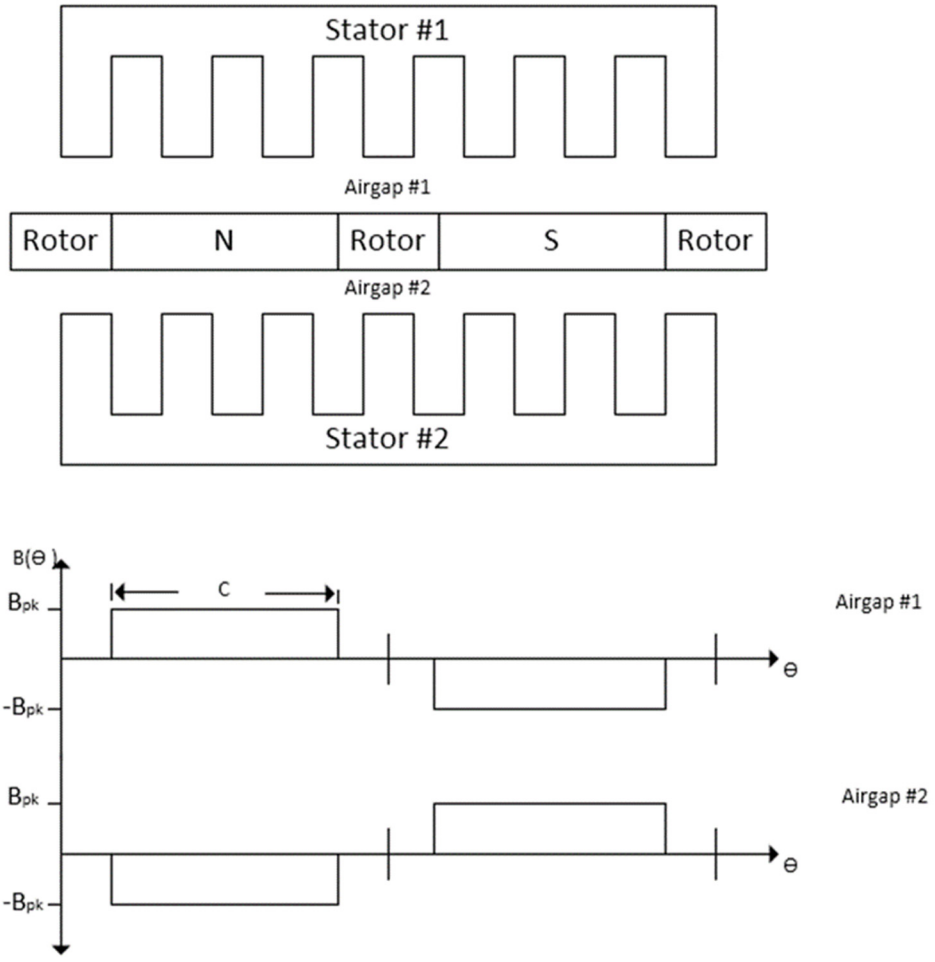

Figure 27. Idealized Air Gap Flux Distribution for Non-Continuous SRDS AFPM Motor

The Fourier Series representation of the idealized air gap flux density for the non-continuous rotor topology presented in Figure 27 as:

$$B(\theta) = \frac{2c}{L} B_{pk} \sum_{n=1}^{\infty} \sin\frac{n\pi}{2} \frac{\sin(\frac{1}{2}\frac{n\pi c}{L})}{\frac{1}{2}\frac{n\pi c}{L}} \sin\frac{n\pi\theta}{L} \tag{3.56}$$

where L is equal to the waveform period divided by 2 (π in both cases), C is the magnet width given in radians and B_{pk} is the analytical calculation of the peak value of the air gap flux density waveform. For a RFPM or standard SRSS AFPM these are given by:

$$c = M_{frac} * \pi \tag{3.57}$$

$$B_{pk} = \frac{B_r}{\frac{1 + \mu_r g'}{H_{mag}}} \tag{3.58}$$

Applying equations (3.56) and (3.57) to an SRDS AFPM is applicable, except that the equation of Bpk, (3.58) must be replaced with the previously developed equation (3.28). Combining these, the idealized representation of a dual stator, single rotor permanent magnet motor's air gap flux density is given as:

$$B(\theta) = \left(\frac{2M_{frac}\pi}{L}\right)\left(\frac{B_r}{1 + \mu_r \frac{2gK_c}{H_m}}\right) \sum_{n=1}^{\infty} \sin\frac{n\pi}{2} \frac{\sin(\frac{1}{2}\frac{n\pi(M_{frac}\pi)}{L})}{\frac{1}{2}\frac{n\pi(M_{frac}\pi)}{L}} \sin\frac{n\pi\theta}{L} \tag{3.59}$$

For the case of the dual stator, single rotor permanent magnet motor, equation (3.59) by itself is sufficient for describing the idealized flux density waveform, but by virtue of using a Fourier Series to generate a square wave, significant ringing and overshoot will be present [21] until n harmonics is high enough to minimize these effects.

To mitigate the ringing and overshoots a Lancoz Sigma Factor [22] will be applied to the Fourier Series using a normalized sinc function, σ. Equation (3.59) is modified as:

$$B(\theta) = \left(\frac{2M_{frac}\pi}{L}\right)\left(\frac{B_r}{1 + \mu_r \frac{2gK_c}{H_m}}\right)\sum_{n=1}^{N} \sin\frac{n\pi}{2} \ \frac{\sin(\frac{1}{2}\frac{n\pi(M_{frac}\pi)}{L})}{\frac{1}{2}\frac{n\pi(M_{frac}\pi)}{L}} \ \sin\frac{n\pi\theta}{L} \ \sigma \tag{3.60}$$

where:

$$\sigma = \frac{\sin {}^{n\pi}/_{m}}{{}^{n\pi}/_{m}} \tag{3.61}$$

and

$$m = N - 1 \tag{3.62}$$

Equations (3.60) – (3.62) can now be used to calculate the no-load spatial distribution flux distribution for the dual stator, single rotor permanent magnet motor. The next section of this thesis will further develop these equations for use in predicting the no-load back-electromotive force for SRDS AFPM motor.

3.4.2 Back-EMF Waveforms

The now established method of predicting the distribution of no-load flux density for the dual stator, single rotor axial field PM motor can now be combined with Faraday's Law and classical machine analysis techniques to determine the back-EMF waveform. The equation for back-EMF of a single rotor, single stator permanent magnet motor with integral slot-pole windings is given as:

$$V_{emf}(\theta, t) \tag{3.63}$$

$$= K_{n1}K_{p1}K_{b1} \ \frac{B_r}{\frac{1 + \mu_{r\,g'}}{H_{mag}}} \sum_{n=1}^{N} \sin\frac{n\pi}{2} \ \frac{\sin\left(\frac{1}{2}\frac{n\pi c}{L}\right)}{\frac{1}{2}\frac{n\pi c}{L}} \sin\frac{n\pi\theta}{L} \ \frac{2C}{L} \ \sigma \, K_{n,n} \, K_{p,n} \, K_{b,n} K_{sm,n} N_{turns} \, L_{act} \frac{dx}{dt}$$

where K_{n1}, K_{p1} and K_{b1} are taken as the fundamental components of equations the winding factors presented in section 3.3.2, N_{turns} is equal to the active number of turns per phase, B_{pk} is given by equation (3.28), and L_{act} is the motors active motor length in meters and dx/dt is the time rate of change of flux in meters per second. K_{sm} is the waveform smoothing function, α_{sm} is our derived smoothing variable, which is a function of our selected motor geometry. K_{sm} and α_{sm} are:

$$K_{sm} = \frac{\sin(n\,\alpha_{sm}/2)}{n\,\alpha_{sm}/2} \tag{3.64}$$

and

$$\alpha_{sm} = \frac{K}{3\,m\,\pi} \tag{3.65}$$

Similar to equation (3.56), equation (3.63) must be modified to account for a dual stator, single rotor motor configuration. The modifications are again limited to adjustment of B_{pk} variable to account for the multiple electromagnetic air gaps, and (3.63) becomes:

$$V_{emf}(\theta,t) \tag{3.66}$$
$$= K_{n1}K_{p1}K_{b1}\,\frac{B_r}{1+\mu_r\frac{2gK_c}{H_m}}\sum_{n=1}^{N}\sin\frac{n\pi}{2}\,\frac{\sin\left(\frac{1}{2}\frac{n\pi c}{L}\right)}{\frac{1}{2}\frac{n\pi c}{L}}\sin\frac{n\pi\theta}{L}\,\frac{2C}{L}\,\sigma\,K_{n,n}\,K_{p,n}\,K_{b,n}K_{sm,n}N_{turns}\,L_{act}\,\frac{dx}{dt}$$

The established method of predicting the no load back-EMF as well as the distribution of no-load flux density for the dual stator, single rotor axial field PM can now be used for predicting machine performance. These equations will be later exercised and compared with finite element and actual motor test results.

Chapter 4

Finite Element Performance Modeling

4.1 Introduction and Motivation for 2D Modeling of Axial Field Motors.

Modeling 3-D motors using 2-D models is common within the motor design industry. This practice is so commonplace that nearly all magnetic finite element packages support it and often 3-D analyses are not conducted during the motor design process. 2-D modeling is typically applied to radial field permanent magnet (RFPM) motors, under the assumption that the machine and subsequent models are axisymmetric, neglecting motor end turn and 3-D leakage effects. In the case of the AFPM machine, where the topology is not axisymmetric, classic 2-D modeling techniques cannot be utilized easily. Because of the inherently non-axisymmetric nature of AFPMs, this thesis investigates the development of a planar model, or series of planar models by unwrapping the axial field topology and constructing an equivalent axisymmetric linear motor model. Discretizing the AFPM into multiple planar models allows 2-D modeling to capture non-linear effects of saturation near the inside diameter of the AFPM, where saturation is most prevalent in the stator iron.

4.2 2D “Unwrapped” Modeling Approaches.

This fundamental concept of developing a planar 2-D model relies on development of an equivalent machine using average spatial parameters to build the finite element model. This linear motor model can then be used to develop flux linkage, phase inductances, and axial force predictions through the use of appropriate modeling and model boundary conditions. Axial force is then applied to an average magnetic moment arm to development motor torque following equation (4.1). This approach departs from the classic averaged model [60], [64] and leverages the equation of Lorentz Force (3.1) to calculate torque for each discrete segment and sum these predictions for overall machine performance (4.1). Using this same approach, machine phase voltage can be solved for using equation (4.2).

$$\mathrm{T} = \sum \vec{F}\ r_n \tag{4.1}$$

$$\mathrm{V} = \frac{d\sum \lambda_n}{dt} \tag{4.2}$$

where F is developed electromagnetic force, I is armature current, L is active magnetic length, B is air gap flux density, r_n is the average radius of the n discretized FEA model, described in Fig. 2, V is phase voltage and λ_n is phase flux linkage for n discretized FE model.

While reconfiguring the AFPM machine geometry into a planar linear model representation does achieve axisymmetry, this same technique introduces new modeling difficulties, such as excessive flux leakage and saturation. Rather than trying to analytically correct 2-D FE results [60], the focus of this research is to identify which configurations are least susceptible to these effects and what modeling changes can be implemented to address to non-conformities. An example of this conversion process, using anti-periodic boundary conditions is presented in Figure 28, Figure 29 and Figure 30.

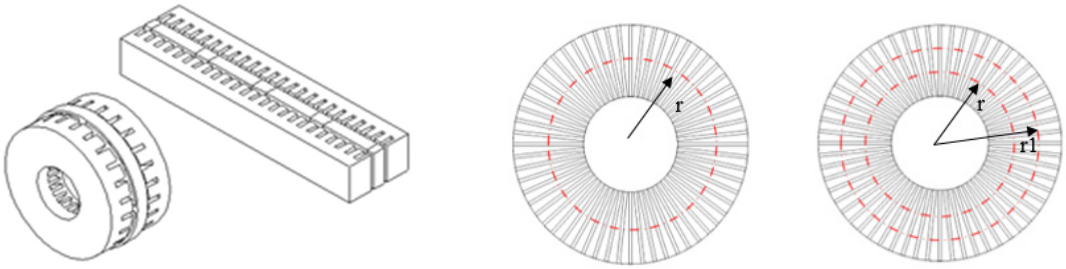

(a) (b) (c)

Figure 28. Axial flux motor assembly and equivalent 2-D planar representation (a), single planar model representation of axial flux motor (b) and planar model with two discrete segments (c).

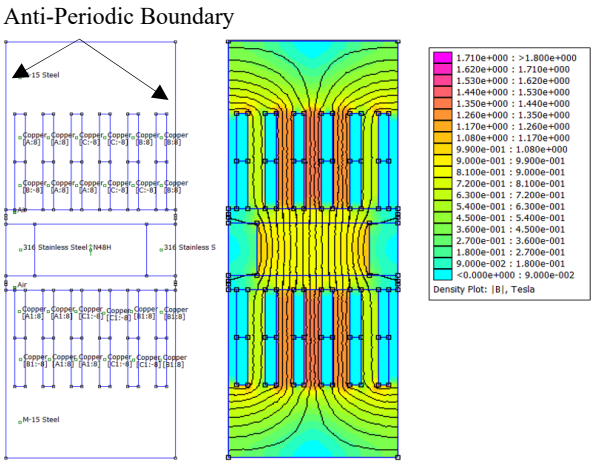

Figure 29. Single pole, single planar FEA model of AFPM

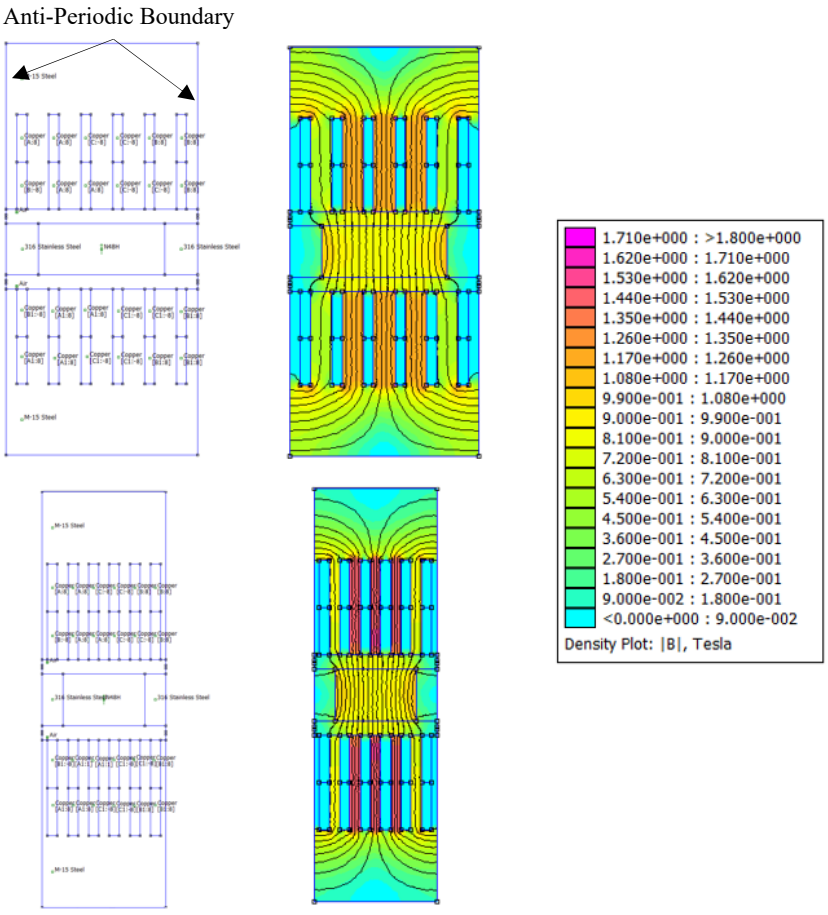

Figure 30. Single pole, two discrete segment FEA model representation of an AFPM

Figure 29 includes a single pole, single plane FEA model [66] with anti-periodic boundary conditions applied to both ends of the model. In this configration the boundary values at each extreme of the model

are of equal magnitiude, but opposite sign [65]. Figure 30 are the same single pole machine model, but it has been discretized into two distinct FE models, using the approach depicted in Figure 28. Each of the models presented in Figure 30 retains anti-periodic boundary conditioning, but has notably different geometry, a result of linearizing the model based on average spatial parameters of the inner and outer diamters chosen when discritizing the model.

The flux density plots presented in Figure 29 and Figure 30 use the same flux density scale showing how the discretized model better represents the flux density in an AFPM as you transverse from the inside diameter of the AFPM towards the outside. The top AFPM planar model of Figure 30 shows considerably less tooth saturation than the lower planar model, because it represents the upper radial portion of the AFPM, averaged on radius r1 of Figure 28 (c); where-as the lower planar model has significanty higher flux levels in the teeth because it represents the inner portion of the AFPM motor, averaged on radius r of Figure 28. While discretizing the AFPM motor into two discrete models helps model saturation effects, further discretization of the AFPM will be presented in the case studies of Chapter 5, to quantify benefits of further discretization.

While using single pole model with anti-periodic or dual pole model with periodic boundary conditions is an appropriate method of modeling an AFPM, it may be desireable to develop a 2D model without having to apply boundary conditions. A periodic boundary condition joins the two boundary joints by setting the boundary points equal to each other, while anti-periodic boundary conditions sets the boundary points to equal value and opposite sign [65]. Assuming the model is periodic or antiperiodic, these two boundary conditions conserve flux, ensuring Gauss's Law (2.1) is met and properly conditioning the model for analysis.

Using this basis of understanding, the following paragraphs investigate alternative, geometric implementaitions of suito-boudary conditions to produce accurate results. Figure 31 presents an improperly conditioned single plane 2-D FE model for a 4-pole, 12-slot AFPM. In Figure 31 flux is crowding on the leftmost teeth of both stators, where-as the rightmost stator teeth have almost no measurable flux present.

If this model were properly conditioned to represent an AFPM the flux would distributed between the leftmost and rightmost teeth of the stator and the leftmost tooth of each stator would have a flux density close to that of the 4th or 7th tooth from the left portion of the figure. However, since this model is improperly conditioned the rightmost teeth have a flux density of less than 0.2 Tesla, where-as the right most teeth have a maximum flux density of approximately 1.5 Tesla.

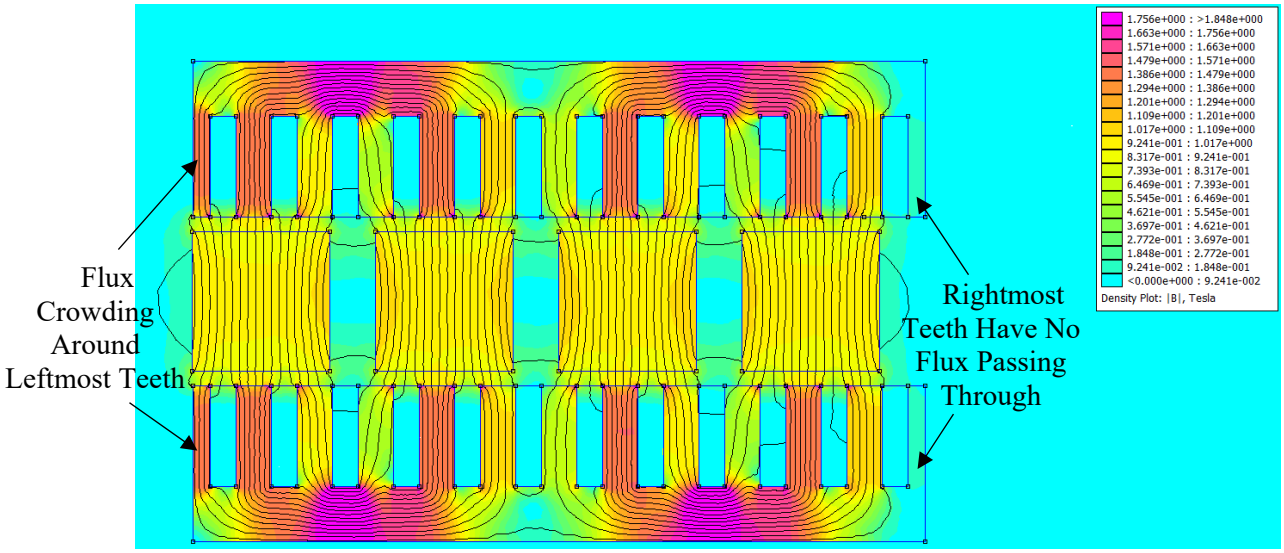

Figure 31. Improperly conditioned 2D, 4-pole AFPM FE Model

Improperly conditioned, unbounded models do not provide a magnetic path for the flux wrap around all the coils causing magnetic saturating at the extents of the laminations stack, reducing the accuracy of predicted phase flux linkage and AFPM performance. Figure 32 seeks to address model boundary conditions through the addition of six extra slots and two magnets. These values were selected as they represent a full 360 electrical degrees for the 4 pole, 12 slot AFPM modeled, allowing the FE model to be analyzed over one full electrical cycle.

The addition of poles and stator teeth address the flux linkage concerns presented in Figure 31, however they do not fully address the accuracy of FE torque calculations. As the magnets transition beyond the extents of planar stator core, a vertical component of magnetic attraction will result from the magnet flux

passing through the stator extents. The flux wrapping will result in unbalanced magnetic pull and ultimately impact accuracy of torque predictions from the FE Model. To address the impacts of flux wrapping on FE model torque predictions, Figure 33 adds an additional six teeth to the model, allowing a full 360 electrical degrees of analysis before magnetic flux wrapping and unbalanced forces occur.

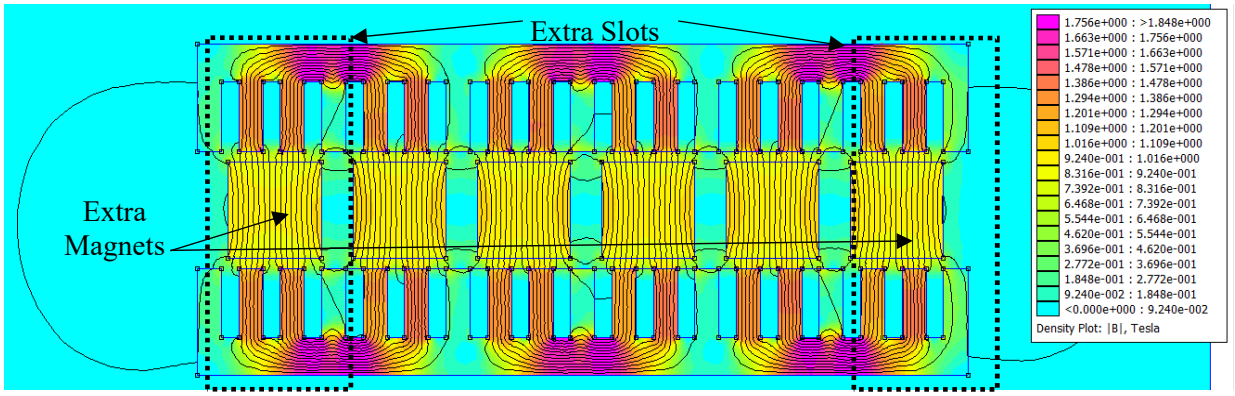

Figure 32. 4-pole AFPM FE Model with two extra magnets and 6 extra slots.

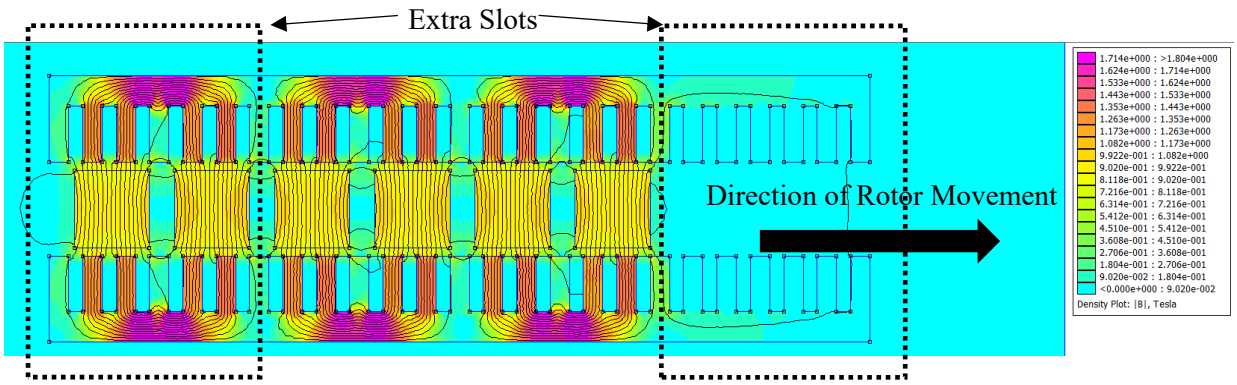

Figure 33. 4-pole AFPM FE Model with two extra magnets and 12 extra slots.

The AFPM model considered in Figure 33 will help address the unbalanced magnetic force, but by virtue of adding additional magnets and teeth, the cogging torque will be marginally increased due to the additional attractive and repulsive forces of the two magnets and the six additional teeth. Figure 34 seeks to solve the problem of additional cogging torque through replacement of the additional 12 slots with a laminated steel flux wrapper. This flux wrapper is the same thickness and laminated steel material of stator yoke, guiding the flux so that it wraps around the 2D AFPM model.

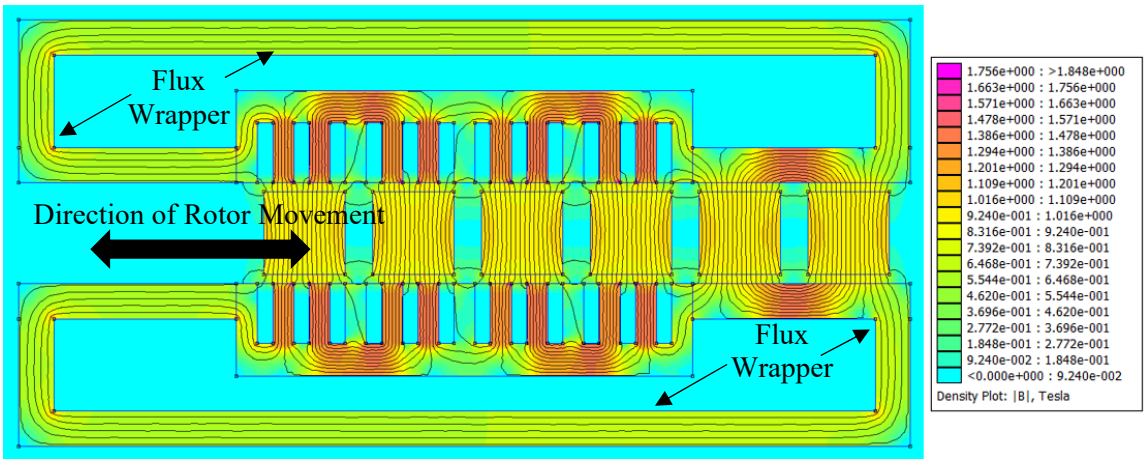

Figure 34. 4-pole AFPM FE Model with two extra magnets and Flux Wrappers

While Figure 31 through Figure 34 attempt to solve the boundary related inaccuracies of 2D AFPM modeling though utilization of alternative geometry, while leaving the model extents unbounded; Figure 35 seeks to solve the model boundary condition through utilization of more classical FE model constraints. In Figure 35 the same 2D AFPM model of Figure 31 is presented, now with the application of antiperiodic boundaries conditions and half width stator teeth at the model extends. The approach of Figure 35 mimics the approach presented in the single pole model of Figure 29, except that it represents the entire AFPM; making it more analogous to the typical full 2D FE model of a RFPM. While not presented in Figure 35, this same model can be discretized using the approach presented in Figure 28 and Figure 30.

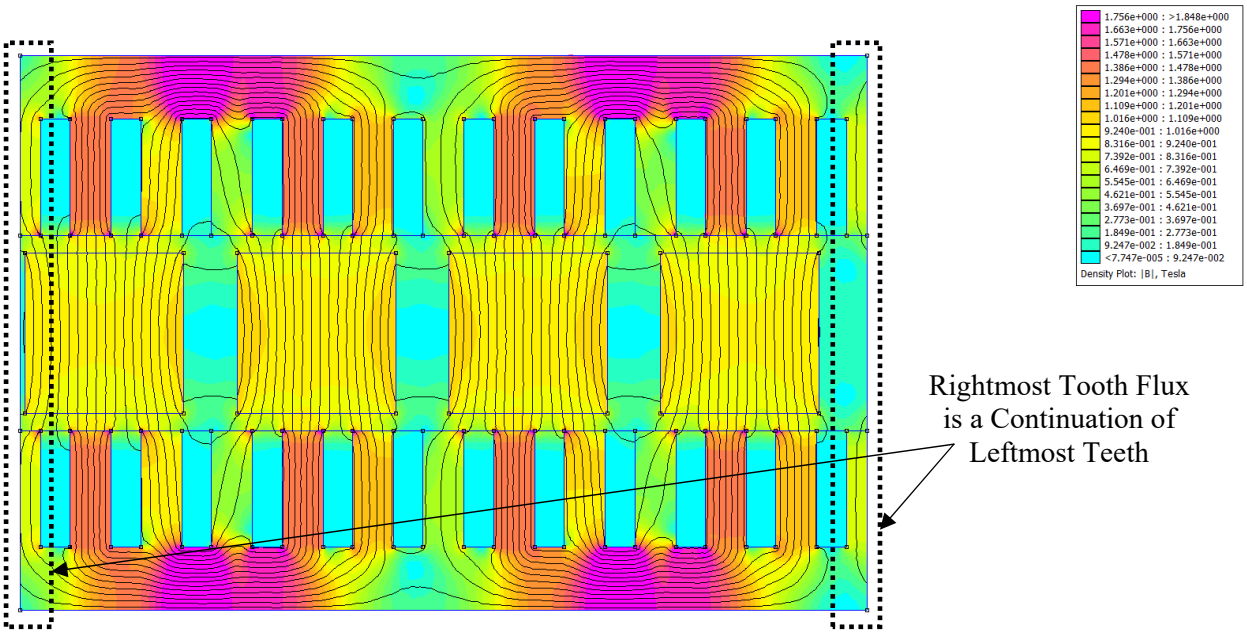

Figure 35. 4-pole AFPM FE Model with antiperiodic boundary conditions

This chapter has presented several approaches to model AFPMs using 2D finite element techniques. The presented approaches use modeling boundary conditions, geometric identities, or both to develop 2D planar models. Chapter 5 will compare the results of each of the proposed methods against analytical and 3D finite element results for a SRDS AFPM which features 10 poles and 60 slots. Lastly Chapter 6 will compare model predictions against a prototype of the SRDS AFPM.

Chapter 5

Machine Design and Performance Case Study

This chapter presents the design and performance case study for a SRDS AFPM. This chapter will first start by describing the machine under consideration. Subsequent sections will use the analytical and finite element methods developed in Chapter 3 and Chapter 4 to characterize the machine under consideration. Lastly this chapter will compare each of the analysis methods and their accuracy relative to more standard 3D finite element modeling results.

5.1 Machine under Evaluation

The machine under consideration is an integral slot-pole SRDS AFPM which features ten magnetic poles and two stators, each featuring sixty stator slots with fractionally pitched, distributed three-phase windings. The machine design parameters are presented below in Table II and a conceptual model is presented in Figure 36.

Table II. SRDS AFPM Machine Parameters

Design Specification - SRDS AFPM			
Parameter	***Value***	***Parameter***	***Value***
Number of Poles	10 (Poles)	Rated Power	3,728 (W)
Number of Slots	60 (Slots)	Rated Speed	1,800 (RPM)
Airgap Height	3.8 (mm)	Outside Diameter	191.7 (mm)
Slot Depth	25.4 (mm)	Inside Diameter	75.5 (mm)
Slot Opening	2.67 (mm)	Average Tooth Width	4.34 (mm)
Magnet Grade	N48H	Magnet Fraction	66.0 (%)
Magnet Remnant Flux Density at 20ºC, Br	1.375 (T)	Magnet Recoil Permeability at 20ºC, μr	1.011
Winding Configuration	5/6 Short Pitched	Winding Connections	Series-Wound

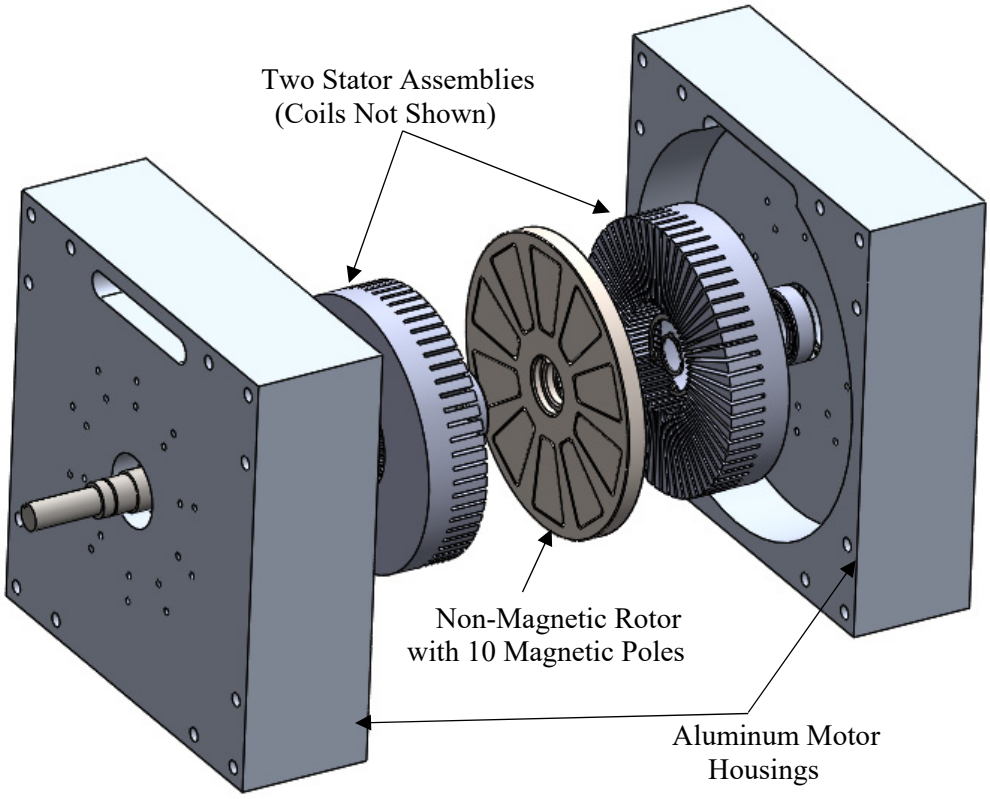

Figure 36. Exploded View of 60-Slot, 10-Pole SRDS AFPM

To ensure an adequate basis of comparison for the analytical and 2D models, a more traditional 3D model of the AFPM was constructed using Altar's Flux 3D software [67]. To reduce the computational time the 3D FE model took advantage of periodicity and was modeled as a periodic two pole section of the motor. In addition to leveraging periodicity, the 3D FE model also took advantage of Flux's Non-Meshed Coil functionality, further reducing computation time. The 3D FE model, including the non-meshed coils, is presented below in Figure 37. The 2D modeling efforts of this thesis were conducted utilizing Finite Element Method Magnetics (FEMM) software [66].

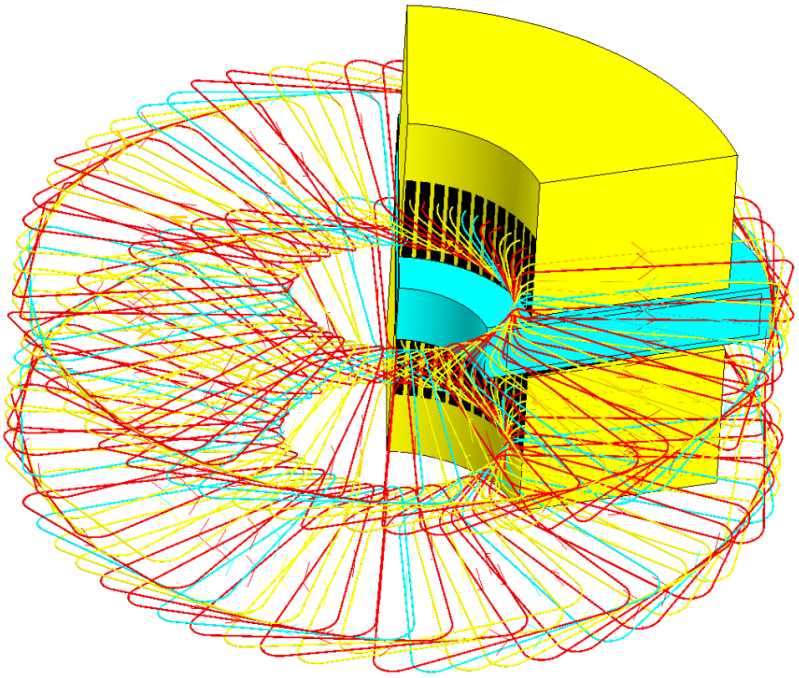

Figure 37. Flux 3D Model of 60-Slot, 10-Pole SRDS AFPM

5.2 Analytical Performance Predictions

The methods developed in Chapter 3 were used for the purpose of generating analytical performance predictions for the 5hp (3,278 W), 1,800 RPM motor. Due to the highly iterative nature of motor design, a Microsoft Excel-based spreadsheet was developed for conducting performance calculations and to generate efficiency estimates. Analytical performance predictions for the 60 Slot, 10 Pole SRDS AFPM are presented in Figure 38. Analytical estimates of the SRDS AFPM's efficiency are presented in Figure 39. These results do not take into account the temperature rise of the machine, and assume that the machine is operating at room temperature, 20ºC. The core loss data presented in Figure 26 were used for core loss predictions of the SRDS AFPM.

Design Outputs - Machine Performance Summary			
Motor Design:	5hp , 1800 RPM SRDS AFPM	**Design Engineer:**	C. Corey

Single Stator Electrical Performance	
BackEMF, L-N [Vpk]	188.93
BackEMF, L-N [Vrms]	133.60
Inductive Voltage,L-N [Vpk]	9.87
Inductive Voltage, L-N [Vrms]	6.98
Resistive Drop, L-N [Vrms]	2.70
Terminal Voltage, L-N [Vpk]	185.38
Terminal Voltage, L-N [Vrms]	131.08
Terminal Voltage, L-L [Vrms]	227.04
Irms [Arms]	4.65
Irms [Apk]	6.58
Power Factor, PF	0.999
Effic. Est.	95.09%

Mechanical Performance	
Mechanical Pout, [Hp]	5.00
Mechanical Pout, [W]	3,728
Mechanical TRQ [ft-lbs]	14.59
Mechanical TRQ [n-m]	19.78
Speed [RPM]	1,800
Cu Losses [W]	75.37
Core Losses [W]	64.22
Stray Losses [W]	37.28
Friction & Windage [W]	15.47
Total Losses [W]	192.34
Electrical Pin [W]	3,920.84

Equivalient Circuit Parameters	
R (L-N) @ 20ºC [Ω]	0.58060
R (L-N) @ Temp. [Ω]	0.58060
R (L-L) @ 20ºC [Ω]	1.16121
L-L inductance [mH]	3.1846
L-N inductance [mH]	1.5923
Electrical Time Constant, Ƭe [Sec]	0.00274

Other Parameters of Interest		
$\tau_{Air\ Gap}$	1.06	psi
Stator Voltage Constant, Ke	0.074	Vrms/RPM
Stator Voltage Constant, Ke	0.105	Vpk/RPM
Stator Torque Constant, Kt	1.568	Ft-lb /Arms
Stator Torque Constant, Kt	1.109	ft-lb/Apk
Current Desity, J	4.79	Apk/mm^2
Current Desity, J	3.39	Arms/mm^2
Motor Weight Estimate [lbs]	72.8	

Analytical Waveform Estimates	
Recommended Crest Factor	1.403
Magnet Fraction, m_{frac}	0.66

Figure 38. SRDS AFPM Motor Performance Summary, 5Hp at 1800 RPM Operation

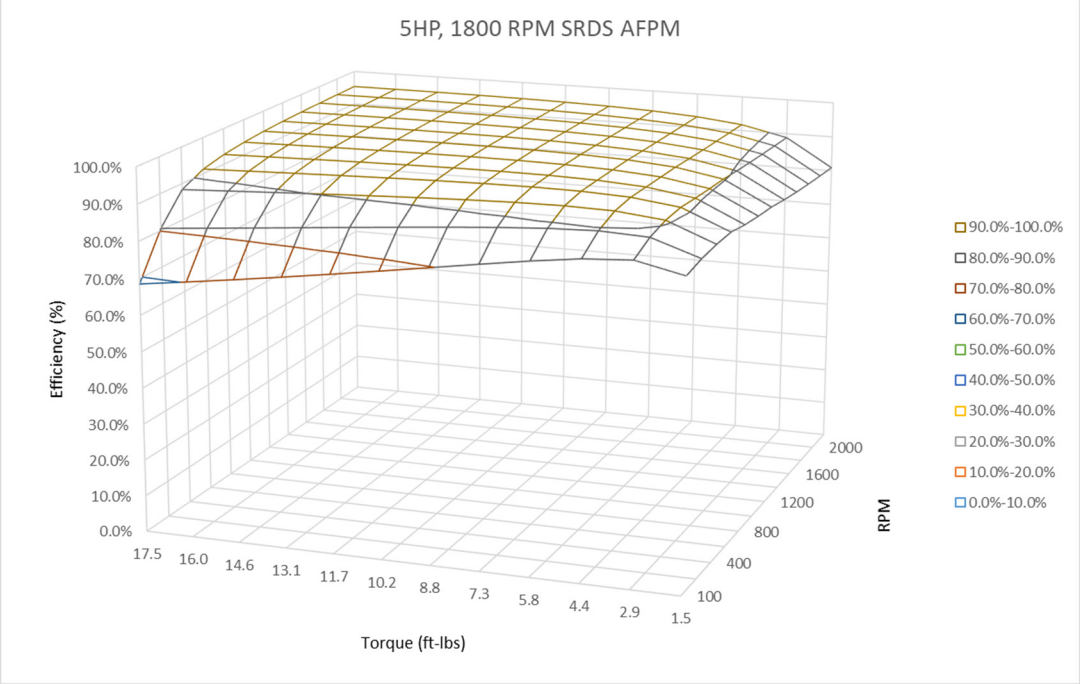

Figure 39. SRDS AFPM Motor Efficiency Map

Studying Figure 38 and Figure 39 we see that the motor's predicted overall efficiency at its rated operational point is 95.1% and that it has a very broad range of high efficiency over a typical speed-torque range that a 5hp, 1800 RPM machine would experience.

Figure 40 presents the analytical waveform estimate performed using the method of equation (3.68) vs. the 3D FEA prediction. Figure 41 presents the Fast Fourier Transform (FFT) of each waveform, for comparison of each waveform's spectral content.

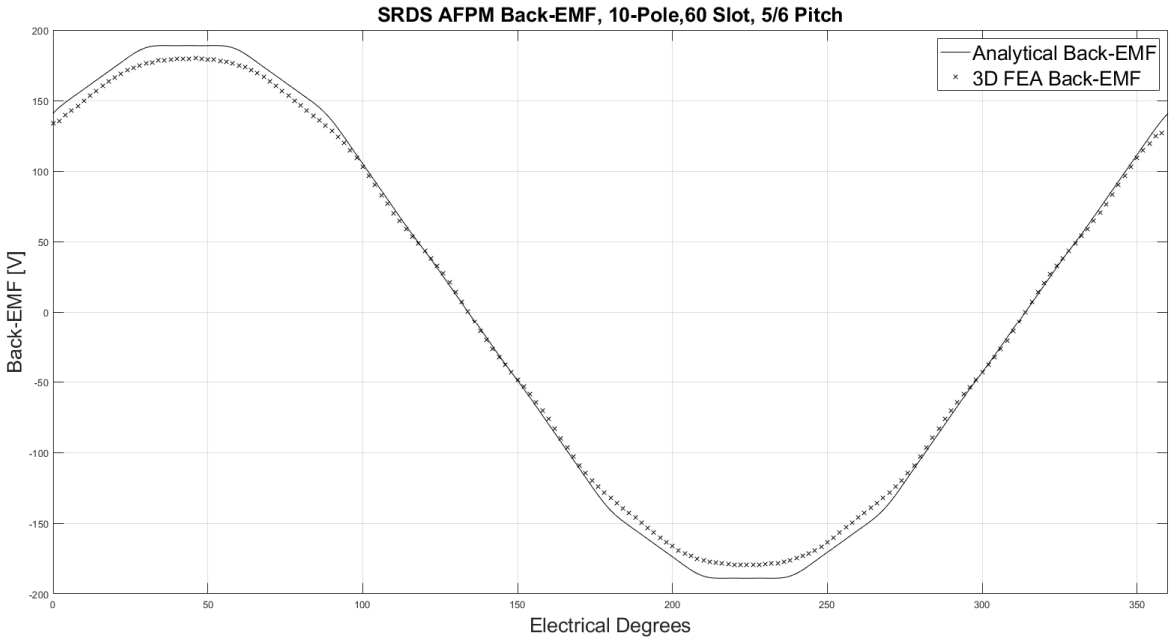

Figure 40. Analytical Back-EMF vs. 3D FEA Back-EMF at 1800 RPM

Reviewing Figure 40, we see that the analytical model predicts a peak voltage of 188.9 volts and an RMS voltage of 134.8 volts; where-as the 3D finite element model predicts a peak voltage of 179.8 volts and RMS voltage of 128.4 volts at 1800 RPM. The analytical model does not include effects such as saturation and approximates leakage flux through use of a Carter coefficient. As such, the observed 4.6% error between the analytical and 3D FE indicates good overall correlation. From Figure 41 we can see that this particular design has a relatively low harmonic distortion. Following equation (5.1) the Total Harmonic

Distortion (THD) of the analytical waveform is 1.62% and the THD of the 3D finite element model is 1.31%, indicating good overall correlation between the two methods.

$$\text{THD} = \frac{\sqrt{V_2^2 + V_3^2 + V_4^2 \ldots V_{20}^2}}{V_1} \tag{5.1}$$

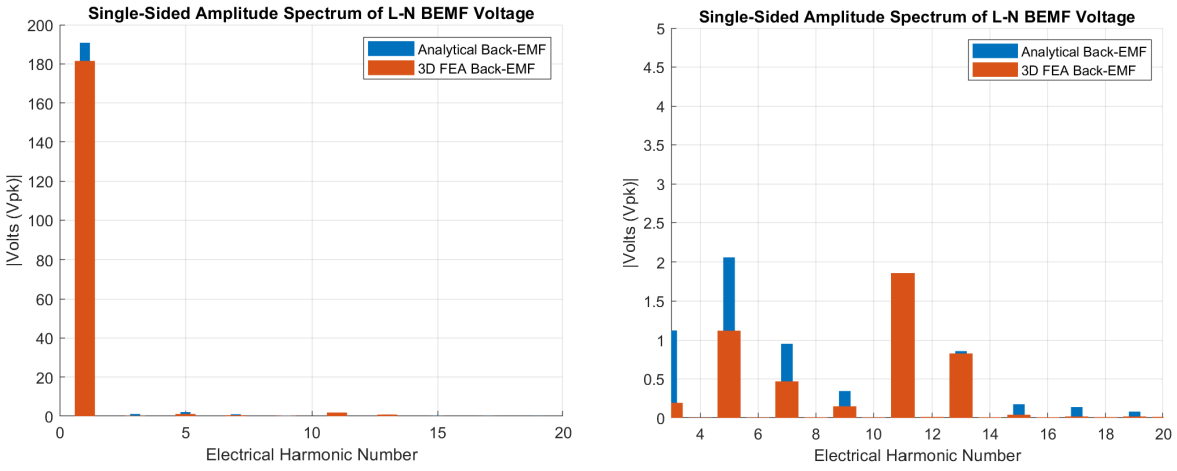

(a) (b)

Figure 41. FFT of Analytical Back-EMF vs. FFT of 3D FEA Back-EMF at 1800 RPM, (a) 1st through 20th Harmonic, (b) 3rd through 20th Harmonic.

5.3 2D Finite Element Performance

Chapter 4 explored different modeling 2D modeling techniques for the SRDS AFPM, the following sub-sections will be used to analyze the machine present in section 5.1 utilizing each method for comparison against each other, analytical and 3D FE predictions. Subsequent to these analyses, and discussion section will compare results and validate 2D predictions with an alternative finite element software package.

5.3.1 Planar Modeling of Axial Flux Machines

The first modeling method presented is the single plane, or single slice 2-D FE model. This is the simplest 2-D model to implement as it is an equivalent linear motor model, derived using average spatial parameters

of the SRDS AFPM. When modeling the SRDS AFPM in a single slice 2D FE model the radius in equation (4.1) simplifies simply the average stator radius, as shown in Figure 28 (b). Below Figure 42 through Figure 49 compare results of single slice 2D FEA modeling against 3D FEA and analytic results.

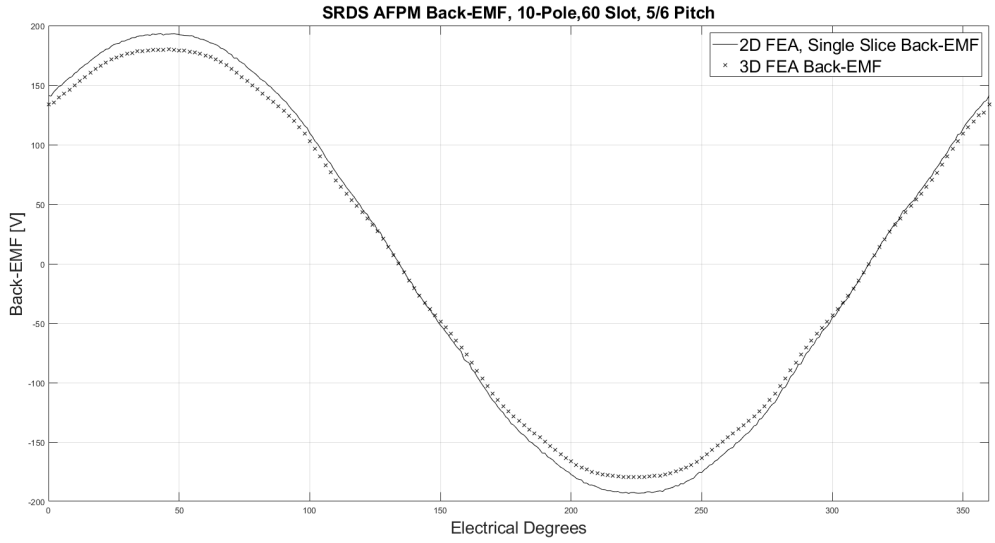

(a)

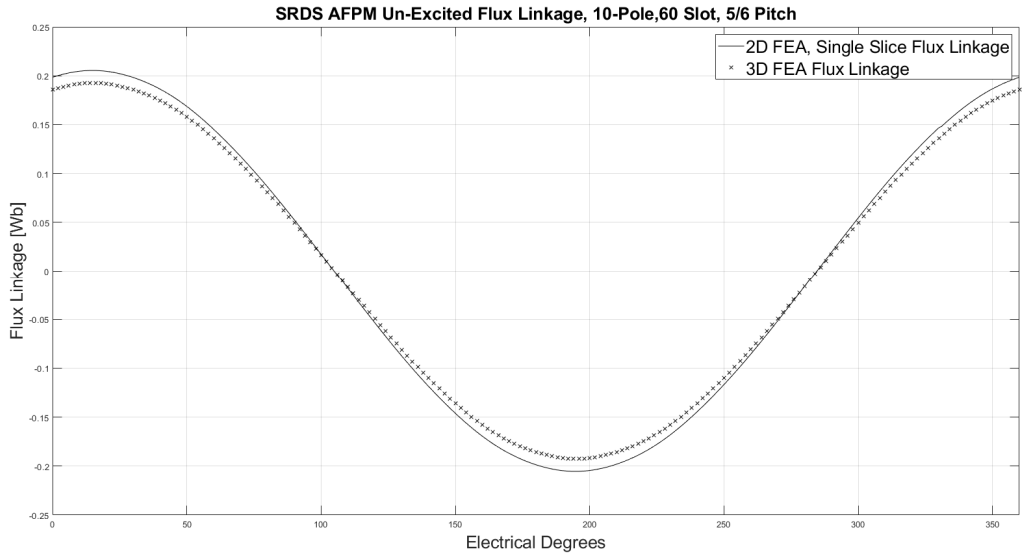

(b)

Figure 42. (a) Single Slice 2D FEA vs. 3D FEA Back-EMF at 1800 RPM and (b) Single Slice 2D FEA vs. 3D FEA Flux Linkage at 1800 RPM

Reviewing Figure 42(a), we see that the single slice 2D model predicts a peak BEMF voltage of 193.2 Volts and an RMS voltage of 137.1 Volts; where-as the 3D finite element model predicts a peak voltage of 179.8 Volts and RMS voltage of 128.4 Volts at 1800 RPM, a 6.7% difference between the two predicted RMS voltages. In Figure 42(b), as expected we see a corresponding difference in the predicted flux linkage between the two modeling techniques. The peak flux linkage of the 2D finite element model is 0.2054 Wb, where the 3D model peak flux linkage is 0.1926 Wb, a difference of 6.7%. Interestingly, this 2D method correlates slightly less than analytical predictions, but the overall spectral content appears to be in good agreement with the 3D FE model.

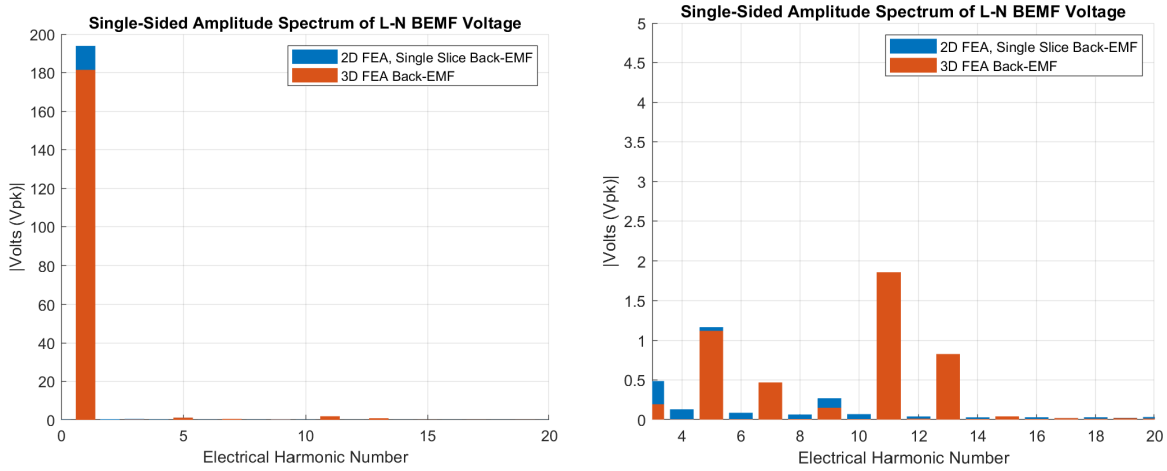

(a) (b)

Figure 43. FFT of 2D FEA, Single Slice Model Back-EMF vs. FFT of 3D FEA Back-EMF at 1800 RPM, (a) 1st through 20th Harmonic, (b) 3rd through 20th Harmonic

Again following (5.1) the THD prediction for the single slice, 2D FEA is 0.99% vs. the 3D FEA prediction of 1.31%. The purpose of a motor is to generate torque, Figure 44 through Figure 47 compare performance predictions of the 2D and 3D FEA results when a sinusoidal stator current of 5A to 100A is applied to that stator terminals. The SRDS AFPMs rated stator current is 6.58A, thus the 100A case presented in Figure 47 looks at an extreme case of saturation, where approximately 15 times rated current is being supplied to the machine.

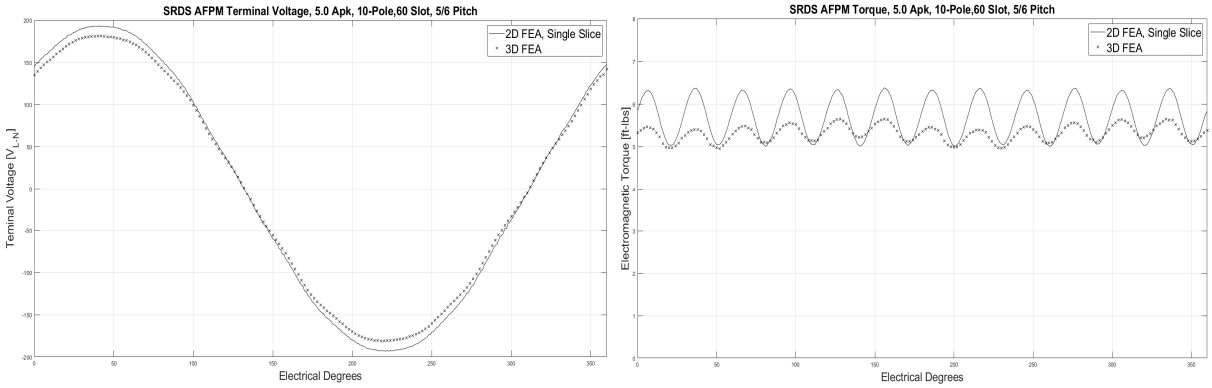

(a) (b)

Figure 44. 2D FEA, Single Slice Model Terminal Voltage vs 3D FEA Terminal Voltage, 1800 RPM, 5.0Apk excitation (a), Resulting Electromagnetic Torque (b)

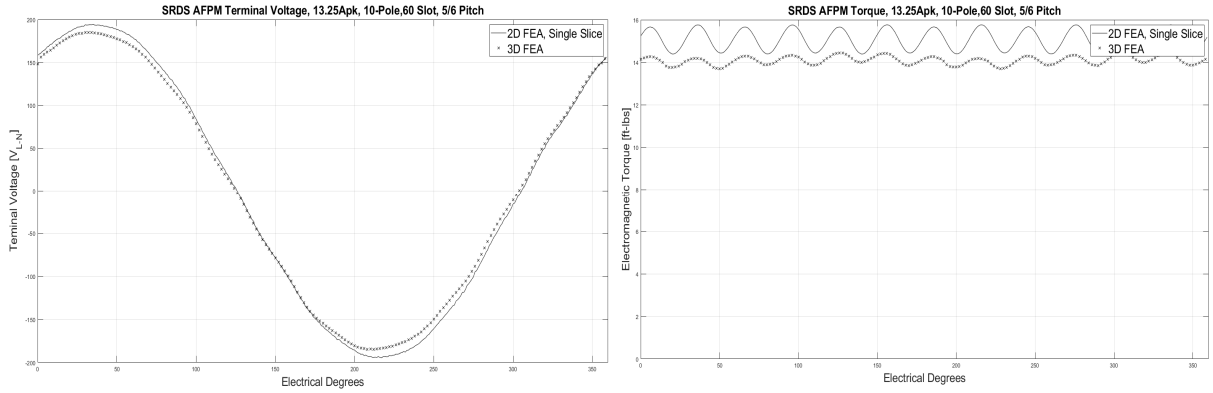

(a) (b)

Figure 45. 2D FEA, Single Slice Model Terminal Voltage vs 3D FEA Terminal Voltage, 1800 RPM, 13.25Apk excitation (a), Resulting Electromagnetic Torque (b)

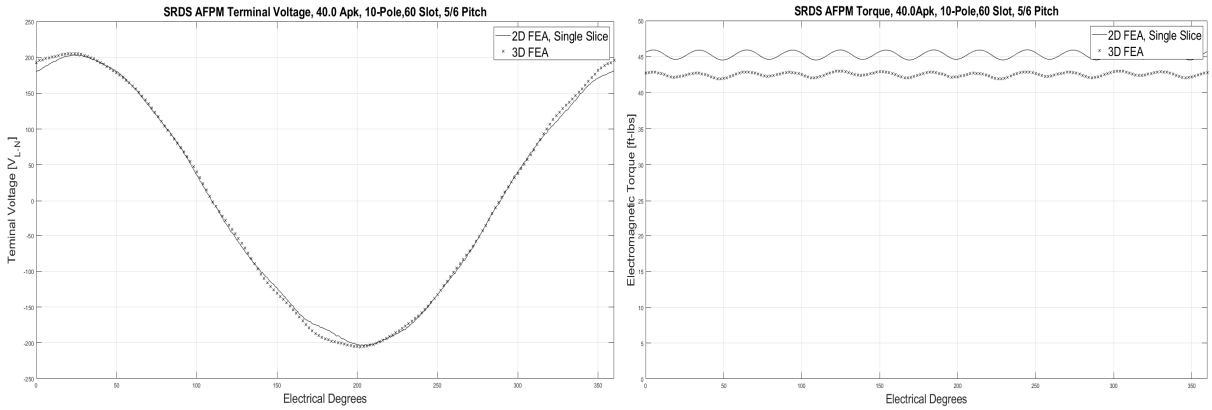

(a) (b)

Figure 46. 2D FEA, Single Slice Model Terminal Voltage vs 3D FEA Terminal Voltage, 1800 RPM, 40.0Apk excitation (a), Resulting Electromagnetic Torque (b)

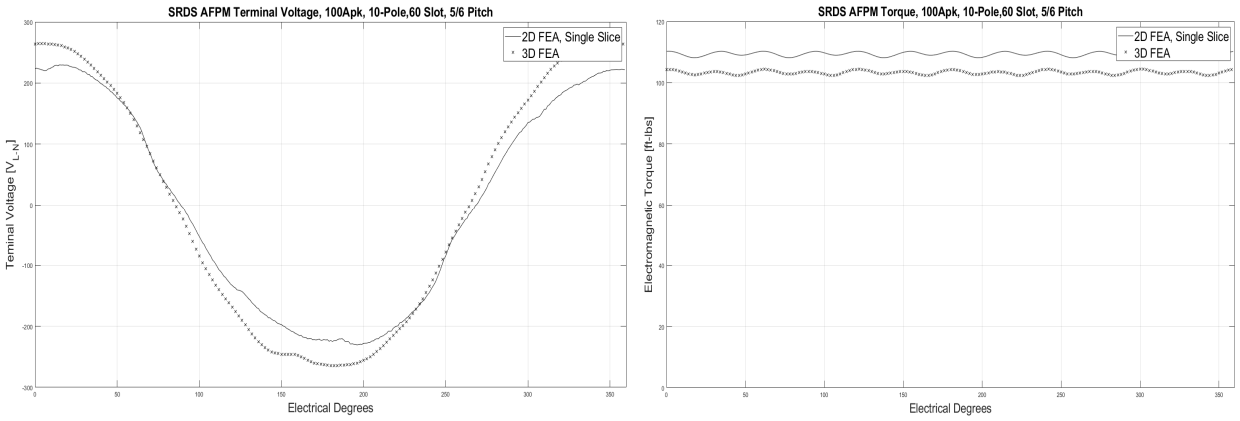

(a) (b)

Figure 47. 2D FEA, Single Slice Model Terminal Voltage vs 3D FEA Terminal Voltage, 1800 RPM, 100Apk excitation (a), Resulting Electromagnetic Torque (b)

Studying Figure 44 we see that the 3D model predicts an RMS voltage of 129.1 volts where the 2D FEA predicts 137.2 volts, a difference of 6.2% in predicted voltage, indicating slightly better correlation than that of BEMF predictions. The average electromagnetic torque predicted by the 2D model is 5.7 ft-lbs, where-as the 3D model is slightly less at 5.3 ft-lbs, an error of 7.5%.

Presented in Figure 45 we can see that the 3D FE model is now predicting and RMS voltage of 131.2 volts, and the 2D FEA predicts 137.2 volts, nearly halving the error from back EMF to 4.5%. The average electromagnetic torque produced by the 2D Single Slice FE model is 15.1 ft-lbs, where-as the 3D FEA is slightly less at 14.1 ft-lbs, an error of approximately 7%.

Figure 46 provides a comparison of the stator being excited by 40Apk of current. When excited by this current, the 3D FE predicts an RMS voltage of 145.7 volts, while the 2D FE model predicts 142.7 volts, a difference of 2.1%. The 3D FE model predicts an average torque of 42.5 ft-lbs, where the 2D FE model predicts and average torque of 45.3 ft-lbs, for a difference of 6.5%.

Lastly, Figure 47 looks at the 100A excitation model. When excited by 100A, the 3D FEA now predicts a RMS terminal voltage of 198.5 volts, versus the 2D model prediction of 170.1 volts, for a difference of 14.3%. While this represents a large increase in terminal voltage variance, the average torque correlation did not parallel this change. The 3D FE model predicts an average torque of 103.3 ft-lbs, versus the 2D FE model prediction of 109.4 ft-lbs, for a variance of only 5.9%.

To further evaluated how the 2D model is representing saturation Figure 48 presents the 2D FEA model's predicted torque constant, Kt, vs. the 3D FEA model prediction and lastly an analytical prediction which does not include saturation effects.

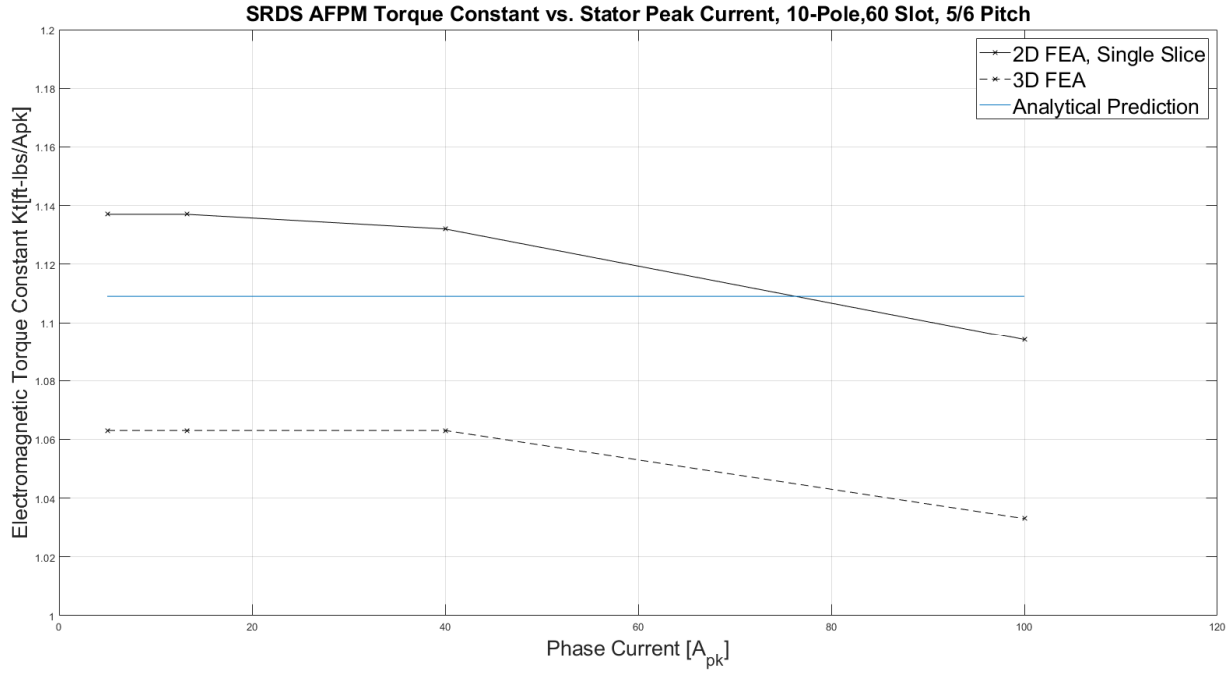

Figure 48. 2D FEA, Single Slice Model Kt vs. vs 3D FEA Kt vs. Analytical Kt

The last attribute evaluated for the single slice 2D FEA model was cogging torque. Figure 49 presents the cogging torque prediction from the 2D single slice FEA versus the 3D FEA. Referring to Figure 49 we see that the 3D model predicts a quasi-sinusoidal cogging torque with a peak amplitude of 0.54 ft-lbs, where-as the 2D model also predicts a quasi-sinusoid, with an amplitude of 0.64 ft-lbs.

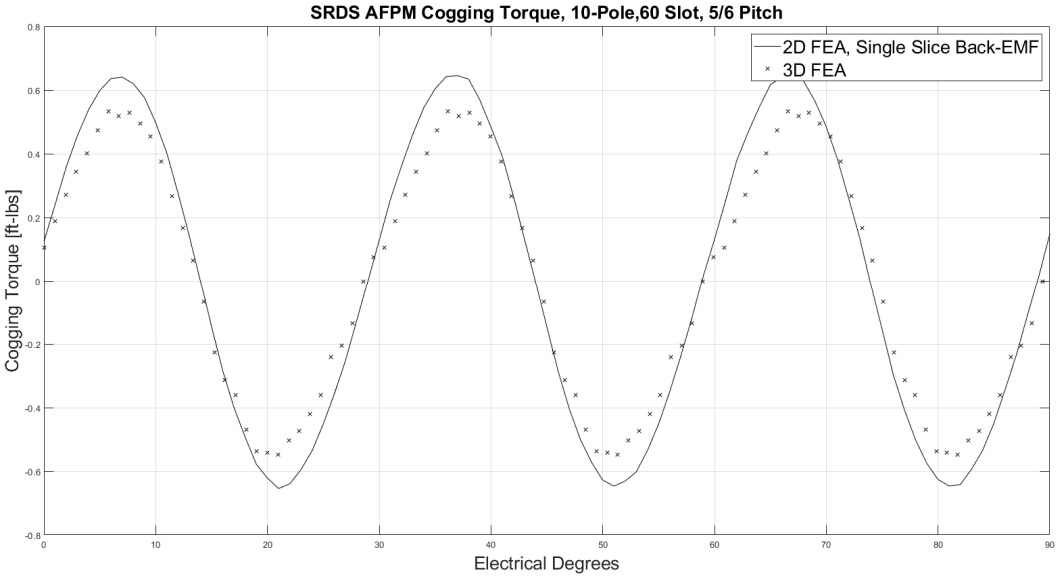

Figure 49. 2D FEA, Single Slice Cogging Torque vs. 3D FEA Cogging Torque Predictions

The next configuration evaluated was discretizing the motor under consideration into two planar, or a two slice 2D FE model and repeating the same set of analyzes. Below Figure 50 through Figure 58 compare results of 2-slice 2D FEA modeling again 3D FEA and analytic results.

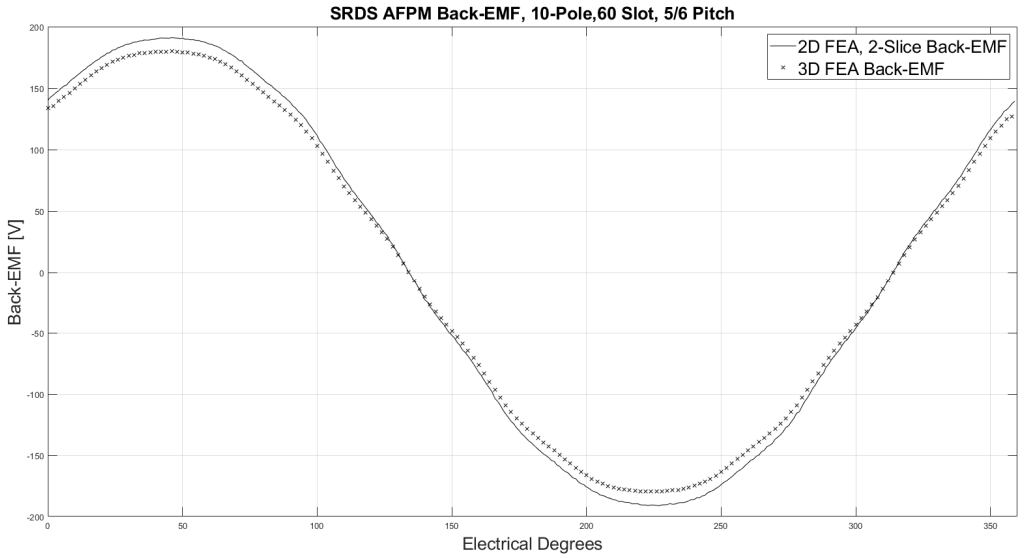

Figure 50. 2-Slice 2D FEA vs. 3D FEA Back-EMF at 1800 RPM

Reviewing Figure 50, we see that the 2-slice 2D model predicts a peak voltage of 191.2 volts and an RMS voltage of 136.5 volts; compared to the 3D finite element model predictions of 179.8 peak volts and RMS voltage of 128.4 volts at 1800 RPM, a 6.3% difference between the two methods and slightly better correlation than was found using the single slice method. Comparing Figure 50 and Figure 51 to Figure 42 and Figure 43 we observer that while the RMS value of the back EMF waveform reduced when increasing to a 2-slice model, the voltage harmonic content also increased. The predicted THD of the 2D, 2-Slice FEA model is now 1.40% vs the 1.31% of the 3D FEA, indicating good agreement between the two modeling techniques.

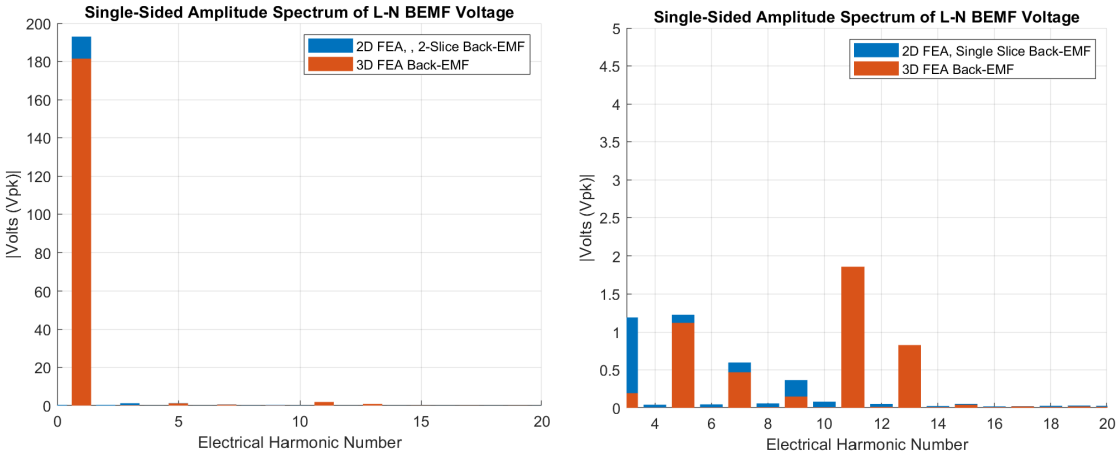

(a) (b)

Figure 51. FFT of 2D FEA, 2-Slice Model Back-EMF vs. FFT of 3D FEA Back-EMF at 1800 RPM, (a) 1st through 20th Harmonic, (b) 3rd through 20th Harmonic

Unlike the single 2D planar model case, the 2-Slice 2D representation will not just have one flux linkage for comparison against 3D modeling efforts. Each of the two independent models will have their own corresponding flux linkage, which needs to be summed, in accordance with (4.2). Below Figure 52 presents each of the individual 2D finite element models flux linkage as well as the sum of the 2D model flux linkages and the 3D model flux linkage for comparison. Figure 53 through Figure 56 provide a comparison

of performance predictions for the 2-Slice 2D FE and 3D FE models when a sinusoidal stator current of 5A to 100A is applied to that stator terminals.

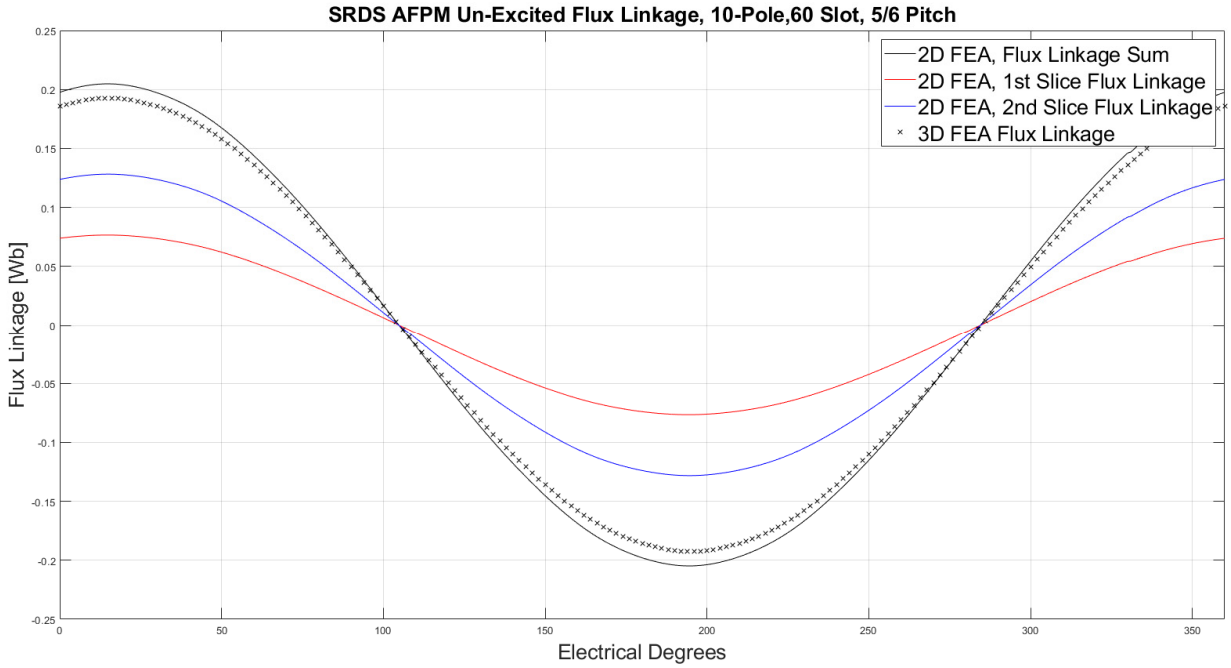

Figure 52. Two Slice 2D FEA vs. 3D FEA Flux Linkage at 1800 RPM

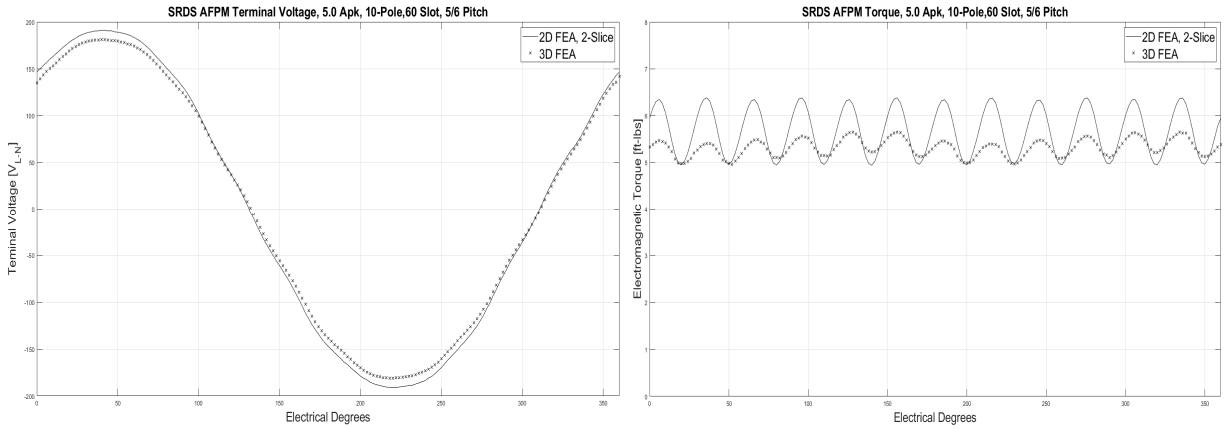

(a) (b)

Figure 53. 2D FEA, 2-Slice Model Terminal Voltage vs 3D FEA Terminal Voltage, 1800 RPM, 5.0Apk Excitation (a), Resulting Electromagnetic Torque (b)

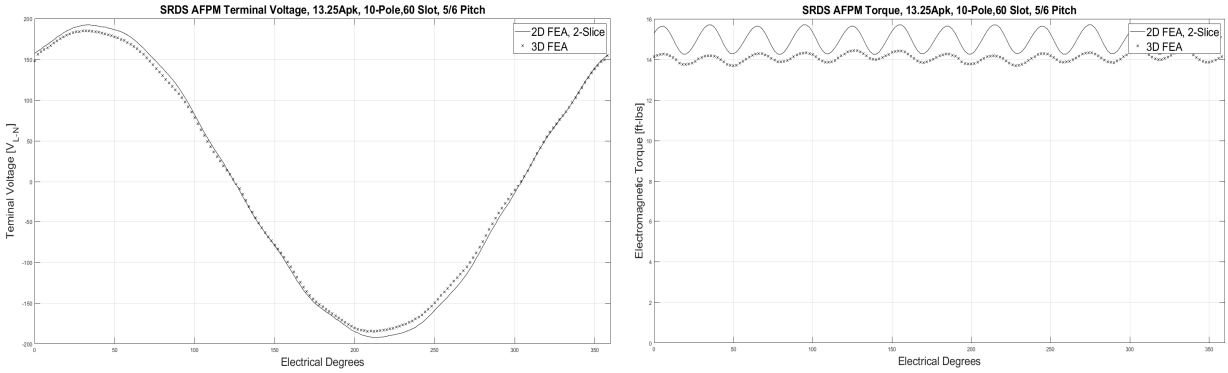

(a) (b)

Figure 54. 2D FEA, 2-Slice Model Terminal Voltage vs 3D FEA Terminal Voltage, 1800 RPM, 13.25Apk excitation (a), Resulting Electromagnetic Torque (b)

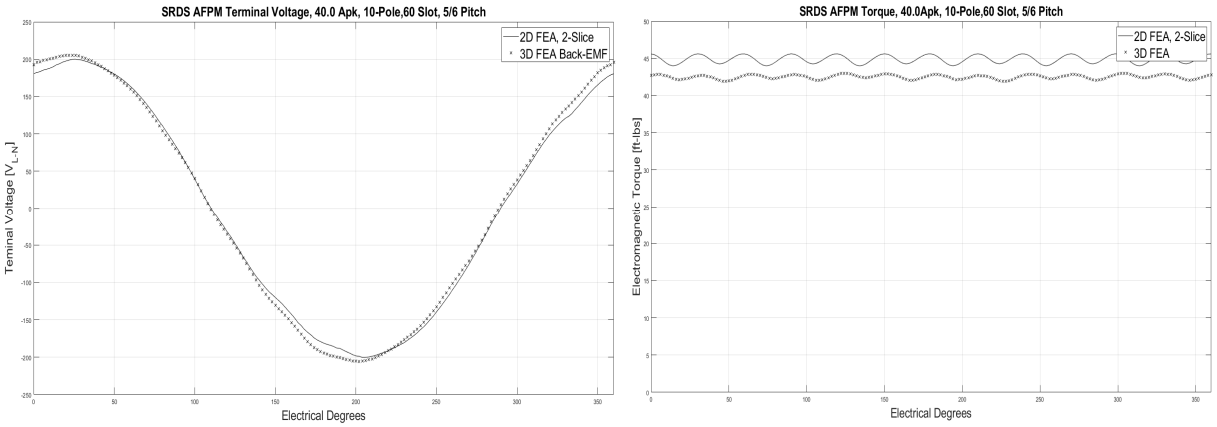

(a) (b)

Figure 55. 2D FEA, 2-Slice Model Terminal Voltage vs 3D FEA Terminal Voltage, 1800 RPM, 40.0Apk excitation (a), Resulting Electromagnetic Torque (b)

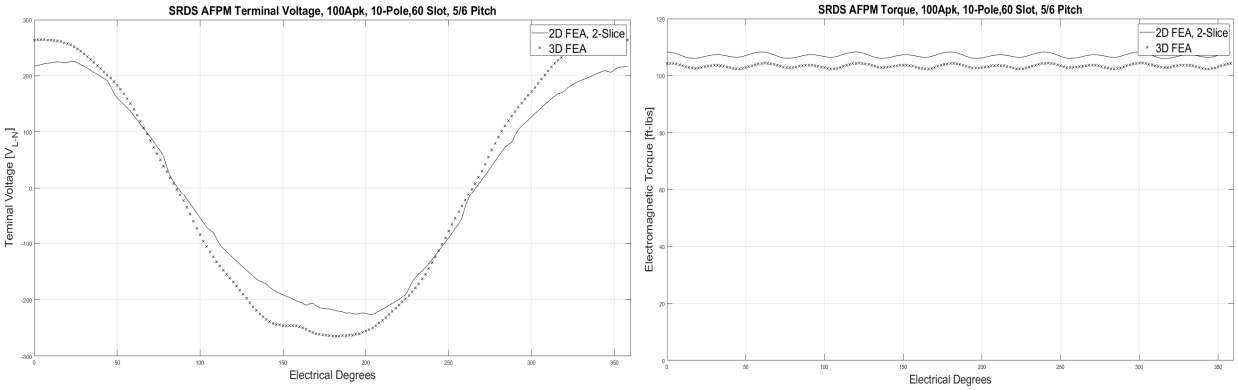

(a) (b)

Figure 56. 2D FEA, 2-Slice Model Terminal Voltage vs 3D FEA Terminal Voltage, 1800 RPM, 100Apk excitation (a), Resulting Electromagnetic Torque (b)

Reviewing Figure 53 we can again see that the 3D FEA model is again predicting and RMS voltage of 129.1 volts, while the 2-Slice 2D FEA is predicting 136.2 volts, an of 7.1%. The average electromagnetic torque produced by the 2D, 2-Slice FE model is 5.6 ft-lbs, versus the 3D FE prediction of 5.3 ft-lbs, reducing the error to 5.6% between the two models.

Presented in Figure 54 we can see that the 3D FE model is now predicting 131.2 Vrms, and the 2-Slice, 2D FEA is predicting 136.5Vrms, reducing the error to 4.0%. The average electromagnetic torque produced by the 2D 2-Slice FE model is 15.0 ft-lbs, where-as the 3D FEA is slightly less at 14.1 ft-lbs, an error of approximately 6.4%.

Figure 55 provides a comparison of the stator being excited by 40Apk of current. When excited by this current, the 3D FE predicts an RMS voltage of 145.7 volts, while the 2D FE model predicts 141.5 volts, a difference of 3.0%. The 3D FE model predicts an average torque of 42.5 ft-lbs, where the 2D FE model predicts and average torque of 44.9 ft-lbs, for a difference of 5.6%.

Lastly, Figure 56 looks at the 100A excitation model. When excited by 100A, the 3D FEA now predicts a terminal voltage of 198.5 Vrms, versus the 2D model prediction of 165.5, for a difference of 16.6%. While this represents a large increase in terminal voltage variance, the average torque correlation did not parallel this change. The 3D FE model predicts an average torque of 103.3 ft-lbs, versus the 2D FE model prediction of 107.1 ft-lbs, for a variance of only 3.6%.

To further evaluated how the 2-Slice 2D model is representing saturation Figure 57 presents the 2D FEA model's predicted torque constant, Kt, vs. the 3D FEA model prediction and last an analytical prediction which does not include saturation effects.

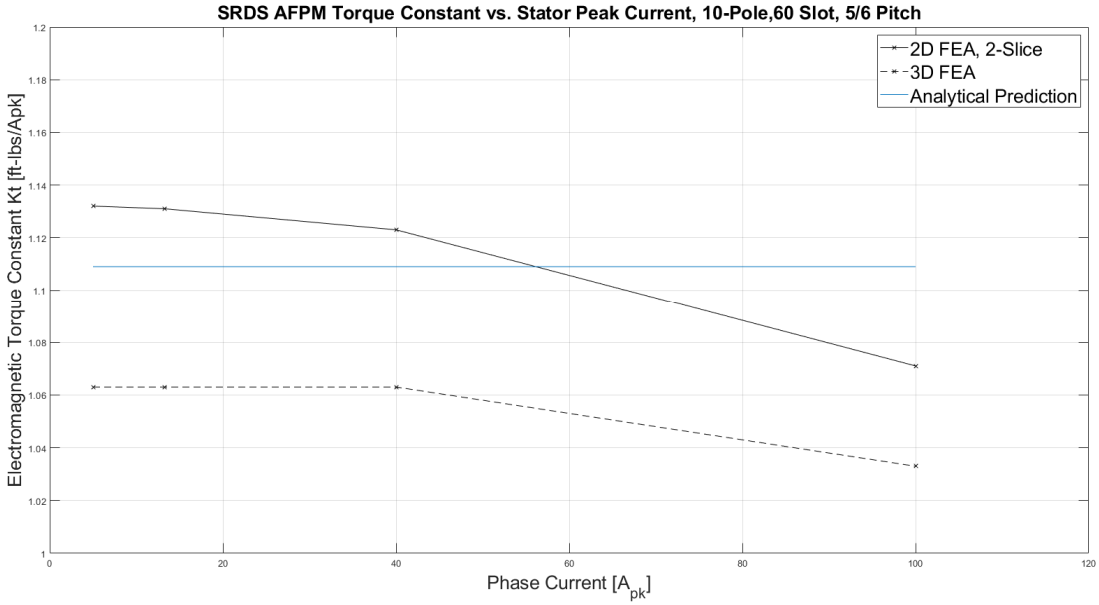

Figure 57. 2D FEA, 2-Slice Model Kt vs. vs 3D FEA Kt vs. Analytical Kt

The last attribute evaluated for the 2-slice 2D FEA model was cogging torque. Figure 58 presents the cogging torque prediction from the 2D single slice FEA versus the 3D FEA. Referring to Figure 58 we can see that the 2-Slice, 2D model predicts a quasi-sinusoidal cogging torque, similar to Figure 49 predictions, with a slightly higher amplitude prediction of 0.70 ft-lbs versus the 3D FEA prediction of 0.54 ft-lbs max.

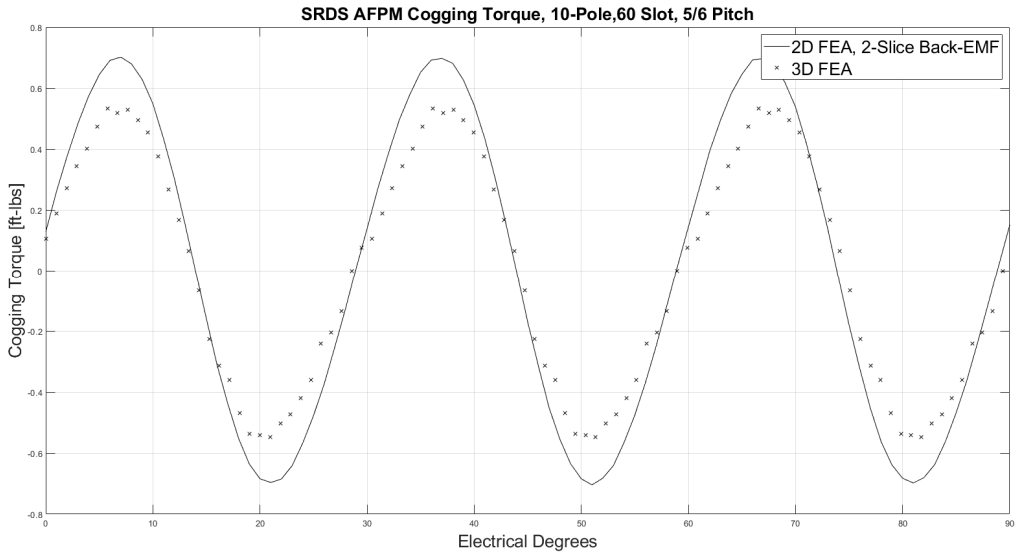

Figure 58. 2D FEA, 2-Slice Cogging Torque vs. 3D FEA Cogging Torque Predictions

The next configuration evaluated was discretizing the motor under consideration into four discrete 2D FEA models, and repeating the same set of analyzes. Below Figure 59 through Figure 67 compare results of 4-slice 2D FEA modeling again 3D FEA and analytic results.

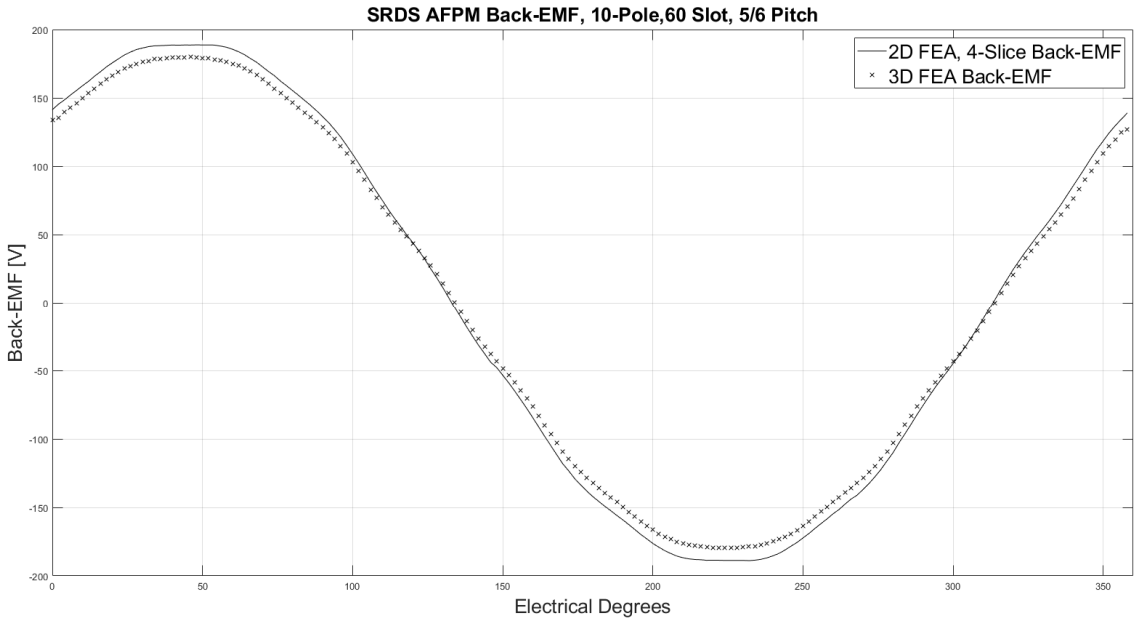

Figure 59. 4-Slice 2D FEA vs. 3D FEA Back-EMF at 1800 RPM

Reviewing Figure 59, we see that the four slice 2D model predicts a peak voltage of 188.7 Volts and an RMS voltage of 136.2 Volts; compared to the 3D finite element model predictions of 179.8 peak Volts and RMS voltage of 128.4 Volts at 1800 RPM, a 6.1% difference between the two methods and again slightly better correlation than was found using the single and 2-slice 2D FEA methods.

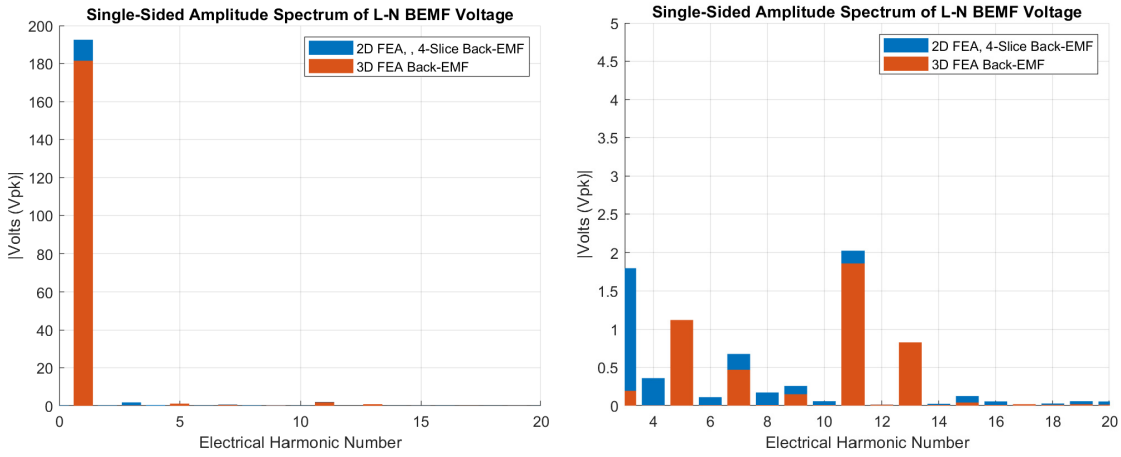

(a) (b)

Figure 60. FFT of 2D FEA, 4-Slice Model Back-EMF vs. FFT of 3D FEA Back-EMF at 1800 RPM, (a) 1st through 20th Harmonic, (b) 3rd through 20th Harmonic

The 4-Slice method seems to have picked up significant even harmonic content in the FFT, likely a result of combining four different models, with 180 magnetostatic analyses per full sweep. However, the even harmonics have little impact on the THD predictions. Including even harmonics, the THD prediction for the 4-Slice 2D FEA is 1.60%, removing the even harmonics it reduces slightly to 1.58%.

Similar to the 2-Slice 2D representation, the 4-Slice 2D representation will have multiple flux linkages, one for each 2D model. The sum of all the models, again following (4.2) will be used for comparison against the 3D flux linkage prediction. Below Figure 61 presents each of the individual 2D finite element models flux linkage as well as the sum of the 2D model flux linkages and the 3D model flux linkage for comparison. Figure 62 through Figure 65 provide a comparison of performance predictions for the 4-Slice 2D FE and 3D FE models when a sinusoidal stator current of 5A to 100A is applied to that stator terminals.

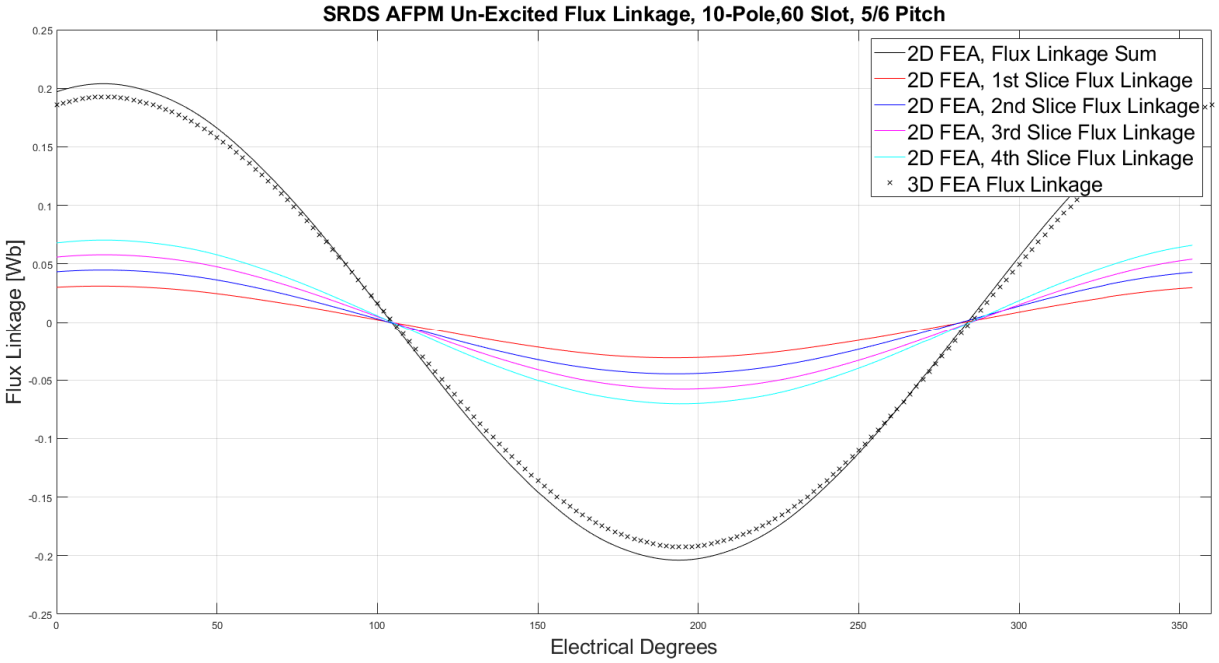

Figure 61. Four Slice 2D FEA vs. 3D FEA Flux Linkage at 1800 RPM

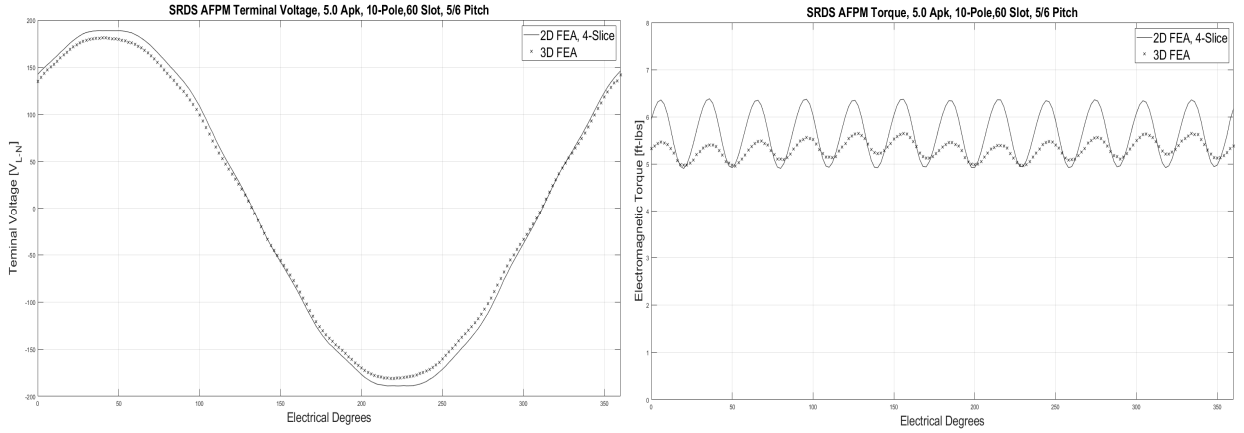

(a) (b)

Figure 62. 2D FEA, 4-Slice Model Terminal Voltage vs 3D FEA Terminal Voltage, 1800 RPM, 5.0Apk excitation (a), Resulting Electromagnetic Torque (b)

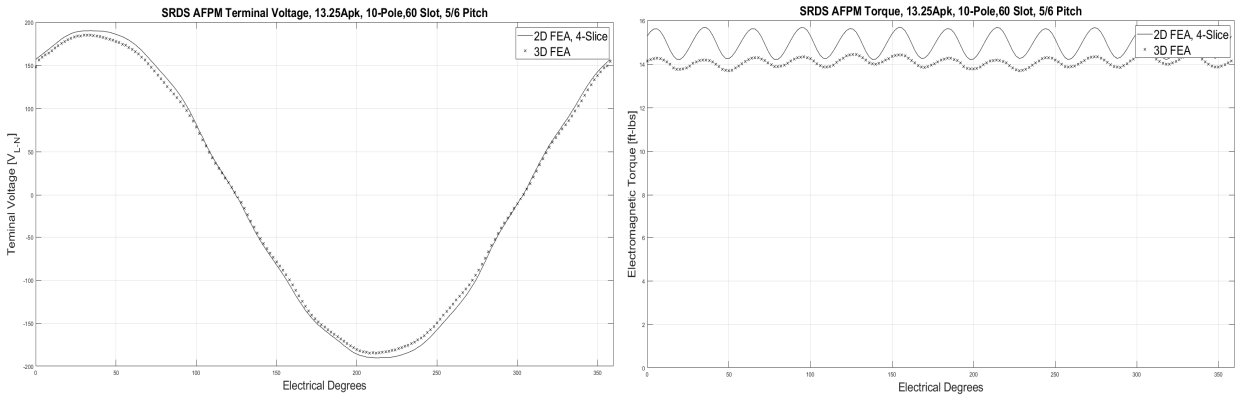

(a) (b)

Figure 63. 2D FEA, 4-Slice Model Terminal Voltage vs 3D FEA Terminal Voltage, 1800 RPM, 13.25Apk excitation (a), Resulting Electromagnetic Torque (b)

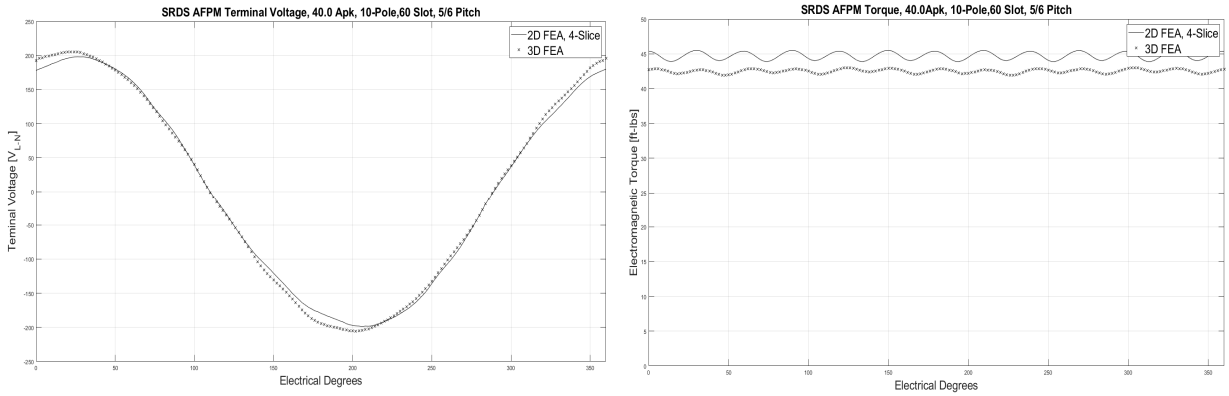

(a) (b)

Figure 64. 2D FEA, 4-Slice Model Terminal Voltage vs 3D FEA Terminal Voltage, 1800 RPM, 40.0Apk excitation (a), Resulting Electromagnetic Torque (b)

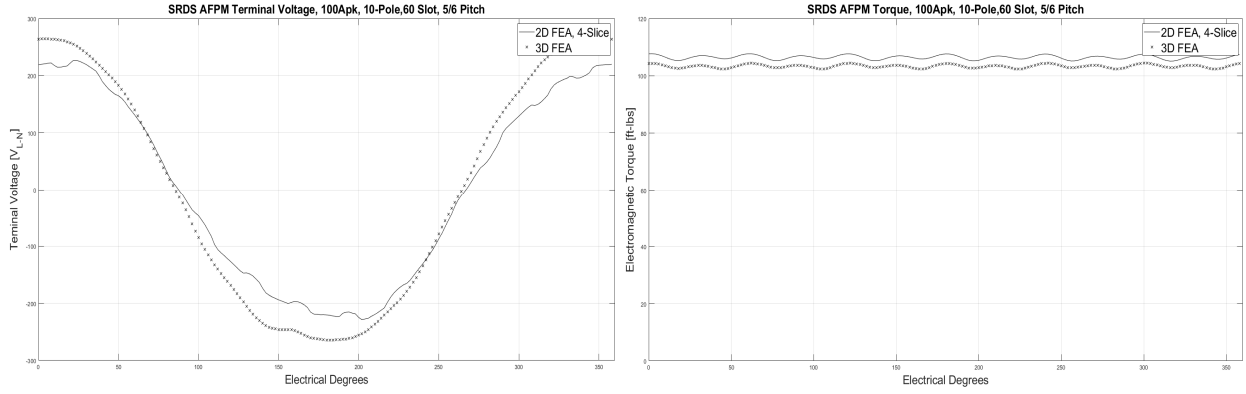

(a) (b)

Figure 65. 2D FEA, 4-Slice Model Terminal Voltage vs 3D FEA Terminal Voltage, 1800 RPM, 100Apk excitation (a), Resulting Electromagnetic Torque (b)

Reviewing Figure 62 we can again see that the 3D FEA model is again predicting and RMS voltage of 129.1 volts, while the 4-Slice 2D FEA is predicting the same 136.2 volts observed using the 2-Slice model, an error of 7.1%. The average electromagnetic torque produced by the 2D, 4-Slice FE model is again 5.6 ft-lbs, versus the 3D FE prediction of 5.3 ft-lbs, and error of 5.6% between the two models.

Presented in Figure 63 we can see that the 3D FE model predicts and RMS voltage of 131.2 volts, while the 4-Slice, 2D FEA is again predicting 136.5Vrms, an error to 4.0%. The average electromagnetic torque produced by the 2D 4-Slice FE model is 15.0 ft-lbs, where-as the 3D FEA is slightly less at 14.1 ft-lbs, an error of approximately 6.4%.

Figure 64 provides a comparison of the stator being excited by 40Apk of current. When excited by this current, the 3D FE predicts an RMS voltage of 145.7 volts, while the 4-Slice 2D FE model predicts 141.4 volts, a difference of 2.9%. The 3D FE model predicts an average torque of 42.5 ft-lbs, where the 4-Slice 2D FE model predicts and average torque of 44.7 ft-lbs, for a difference of 5.2%.

Lastly, Figure 65 looks at the 100A excitation model. When excited by 100A, the 3D FEA predicts a RMS terminal voltage of 198.5 volts, versus the 4-slice 2D model prediction of 164.7 volts, for a difference of 17.0%. While this represents a large increase in terminal voltage variance, the average torque correlation did not parallel this change. The 3D FE model predicts an average torque of 103.3 ft-lbs, versus the 2D FE model prediction of 106.5 ft-lbs, for a variance of only 3.1%.

To further evaluated how the 4-Slice 2D model is representing saturation Figure 66 presents the 2D FEA model's predicted torque constant, Kt, vs. the 3D FEA model prediction and last an analytical prediction which does not include saturation effects.

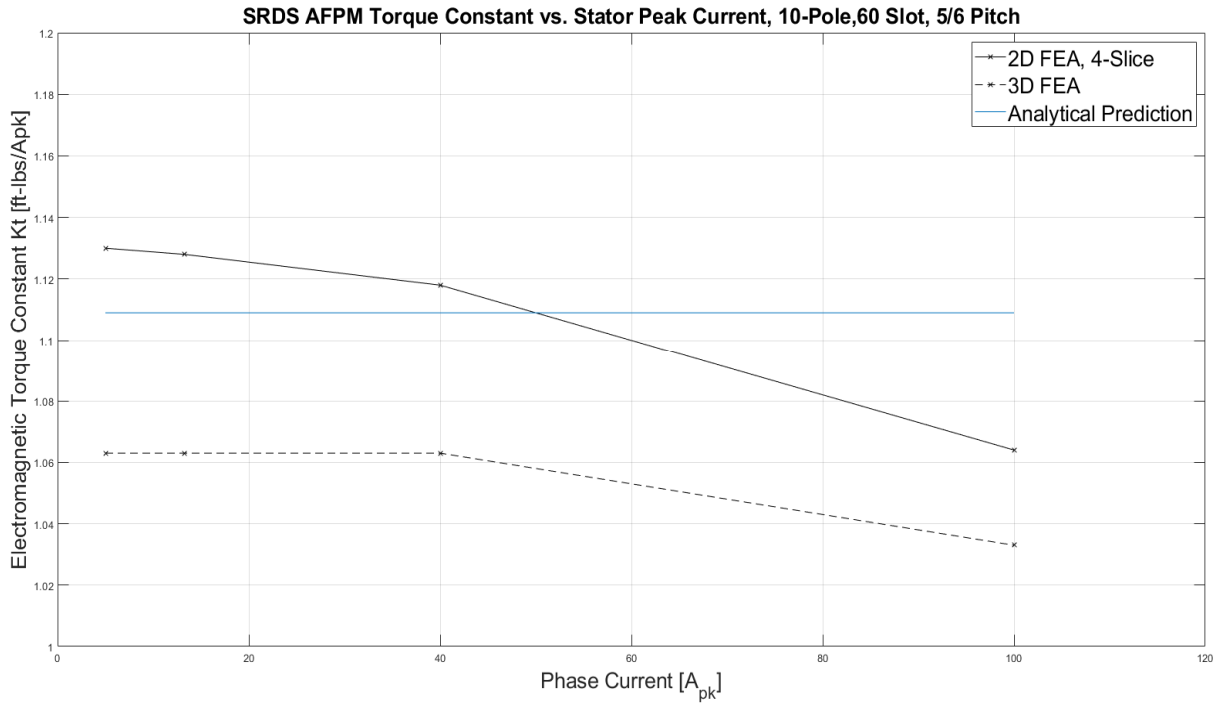

Figure 66. 2D FEA, 4-Slice Model Kt vs. vs 3D FEA Kt vs. Analytical Kt

The last attribute evaluated for the 4-slice 2D FEA model was cogging torque. Figure 67 presents the cogging torque prediction from the 2D 4-slice FEA versus the 3D FEA. Referring to Figure 67 we can see that the 4-Slice, 2D model predicts a quasi-sinusoidal cogging torque, similar to Figure 49 predictions, with an again slightly higher amplitude prediction of 0.72 ft-lbs versus the 3D FEA prediction of 0.54 ft-lbs max.

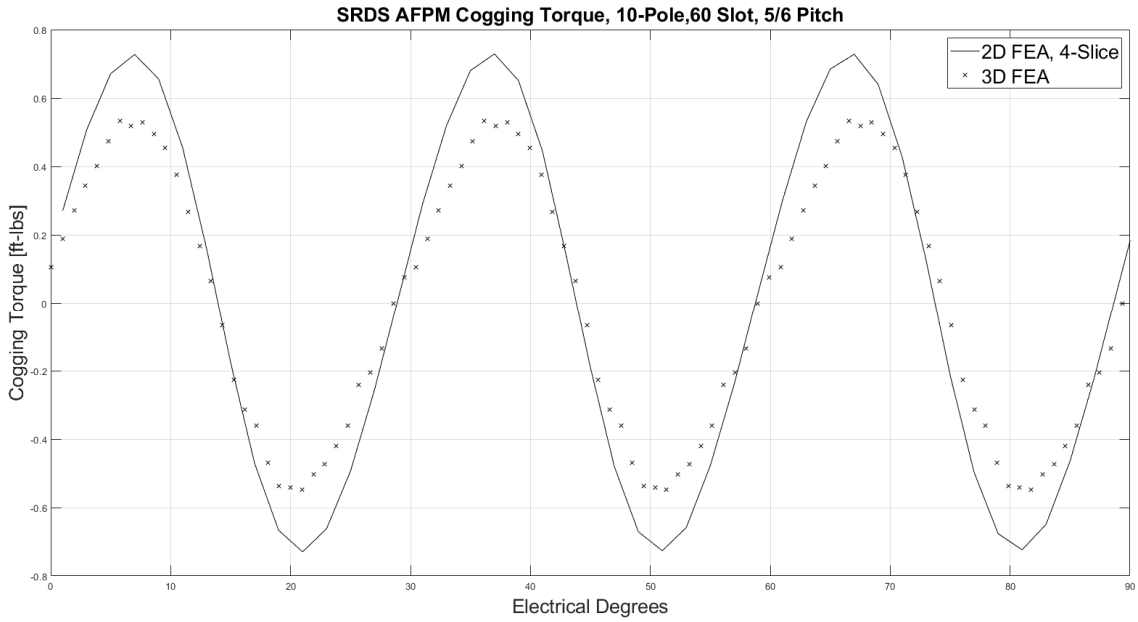

Figure 67. 2D FEA, 4-Slice Cogging Torque vs. 3D FEA Cogging Torque Predictions

The next configuration evaluated was discretizing the motor under consideration into four discrete 2D FEA models, and repeating the same set of analyzes. Below Figure 59 through Figure 67 compare results of 8-slice 2D FEA modeling again 3D FEA and analytic results.

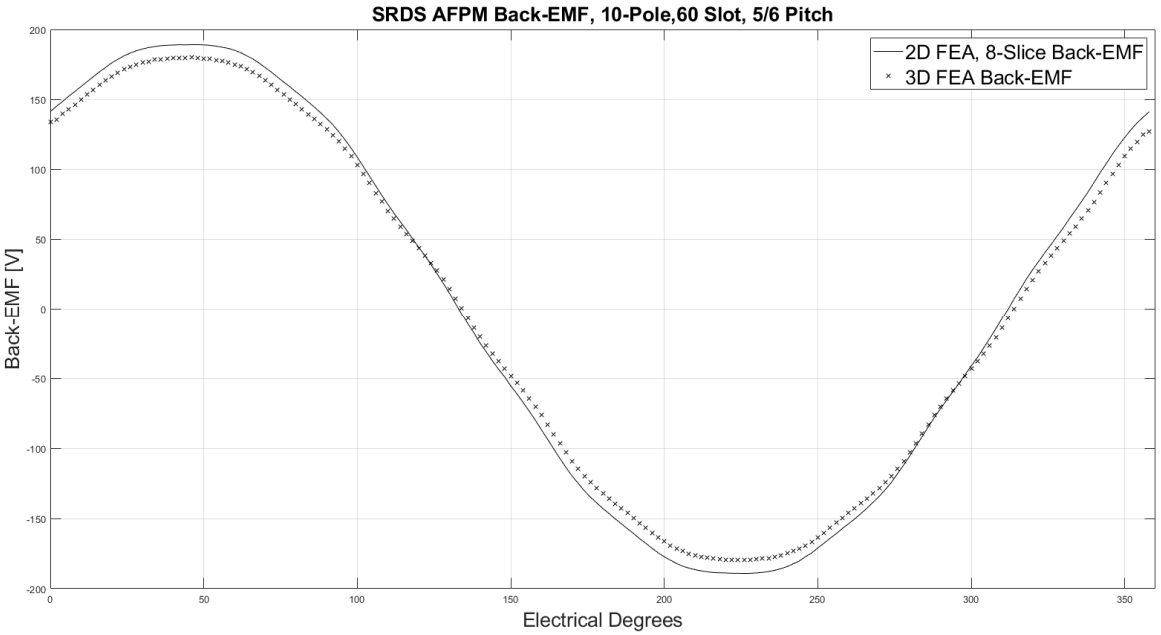

Figure 68. 8-Slice 2D FEA vs. 3D FEA Back-EMF at 1800 RPM

Reviewing Figure 68, we see that the 4-slice 2D model FE predicts a peak voltage of 189.1 volts and an RMS voltage of 136.2 volts; compared to the 3D finite element model predictions of 179.8 peak volts and RMS voltage of 128.4 volts at 1800 RPM, a 6.1% difference between the two methods and again slightly better correlation than was found using the single and 2-slice 2D FEA methods.

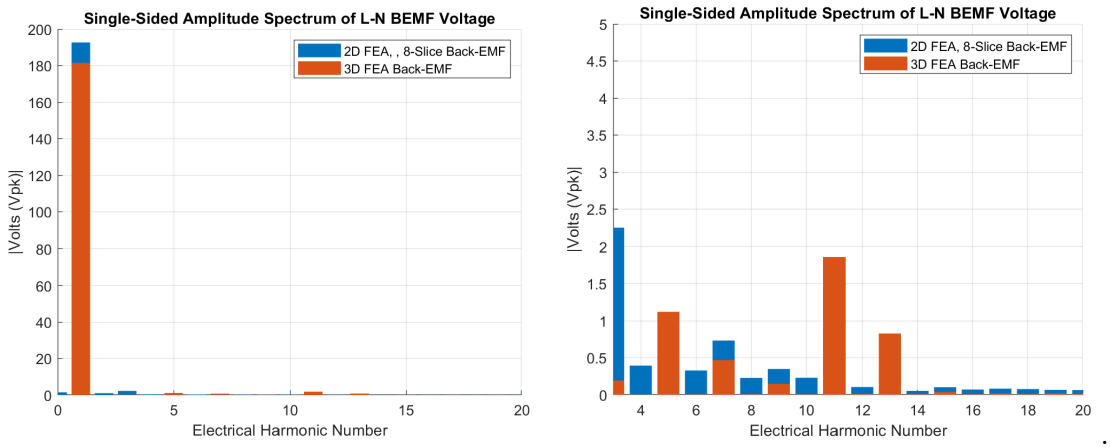

(a) (b)

Figure 69. FFT of 2D FEA, 8-Slice Model Back-EMF vs. FFT of 3D FEA Back-EMF at 1800 RPM, (a) 1st through 20th Harmonic, (b) 3rd through 20th Harmonic

The 8-Slice method seems retained the even harmonic content observed in the 4-slice method, again likely a result of combining four different models, with 180 magnetostatic analyses per full sweep. Including the artificial even harmonics, the THD prediction for the 8-Slice 2D FEA is 1.65%, removing this artificial harmonics it reduces slightly to 1.62%.

Again, similar to the 2-Slice and 4-Slice 2D representation, the 8-Sice 2D representation will not have multiple flux linkages, one for each 2D model. The sum of all eight models, again following (4.2) will be used for comparison against the 3D flux linkage prediction. Below Figure 70 presents each of the individual 2D finite element models flux linkage as well as the sum of the 2D model flux linkages and the 3D model flux linkage for comparison. Figure 71 through Figure 74 provide a comparison of performance predictions

for the 8-Slice 2D FE and 3D FE models when a sinusoidal stator current of 5A to 100A is applied to that stator terminals.

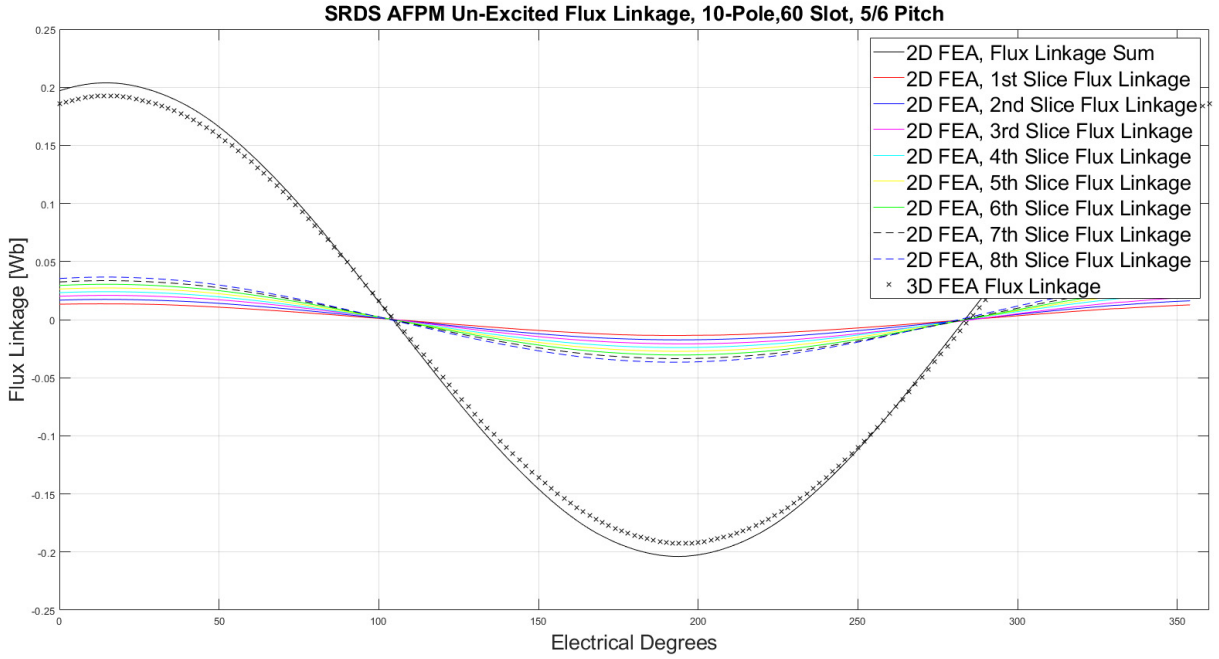

Figure 70. 8-Slice 2D FEA vs. 3D FEA Flux Linkage at 1800 RPM

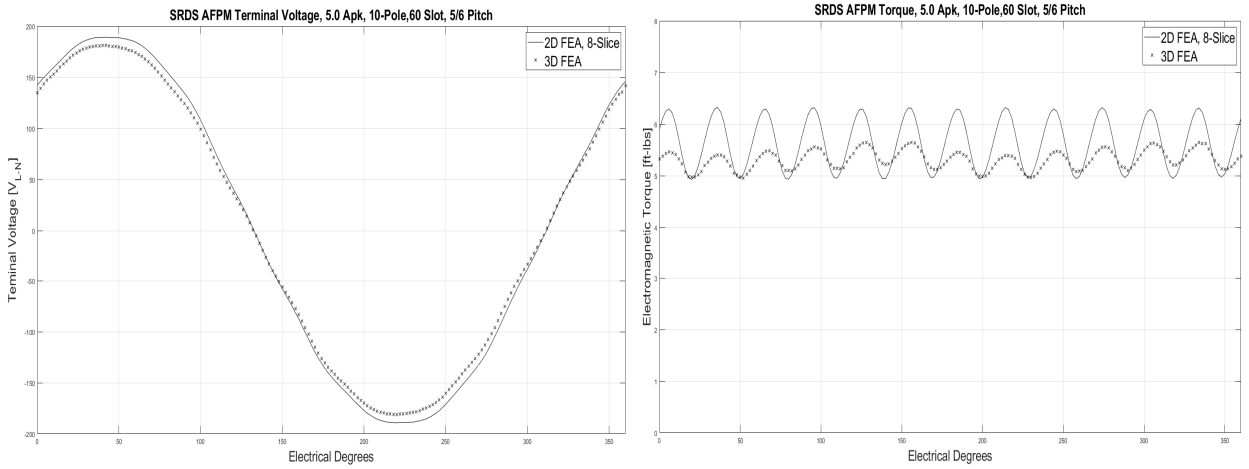

(a) (b)

Figure 71. 2D FEA, 8-Slice Model Terminal Voltage vs 3D FEA Terminal Voltage, 1800 RPM, 5.0Apk excitation (a), Resulting Electromagnetic Torque (b)

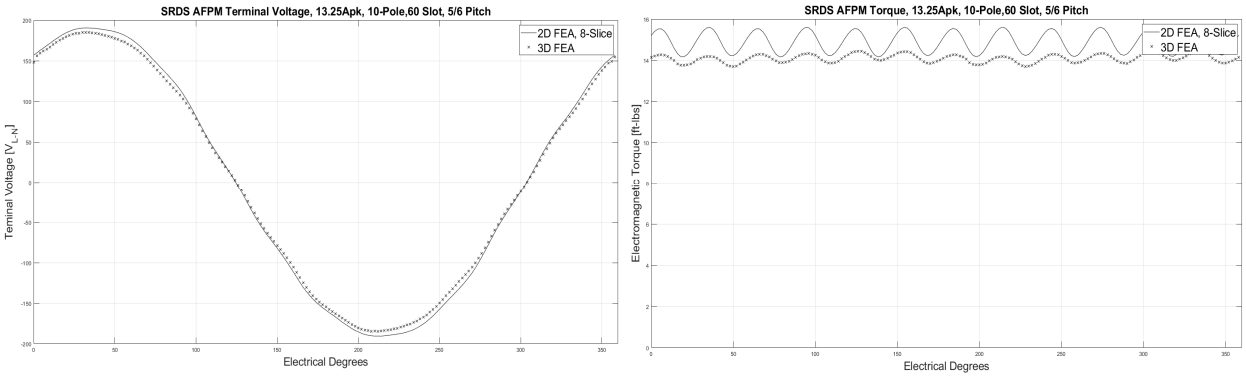

(a) (b)

Figure 72. 2D FEA, 8-Slice Model Terminal Voltage vs 3D FEA Terminal Voltage, 1800 RPM, 13.25Apk excitation (a), Resulting Electromagnetic Torque (b)

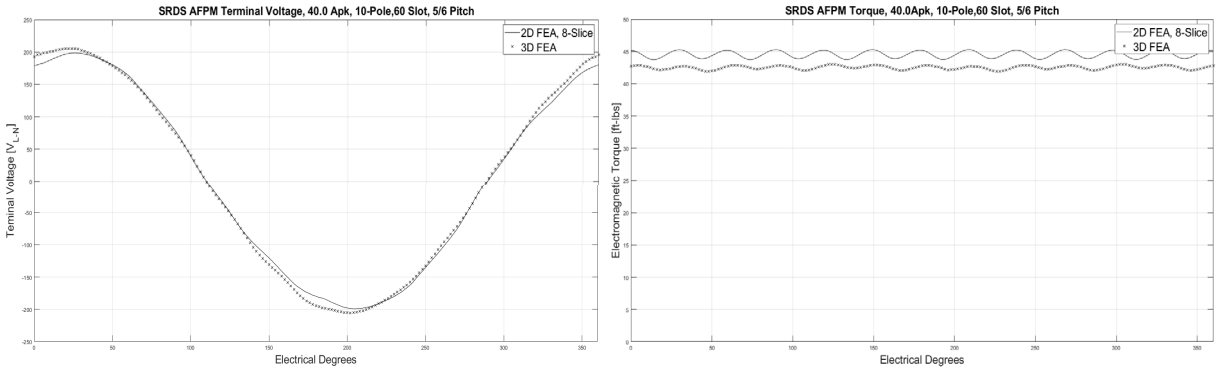

(a) (b)

Figure 73. 2D FEA, 8-Slice Model Terminal Voltage vs 3D FEA Terminal Voltage, 1800 RPM, 40.0Apk excitation (a), Resulting Electromagnetic Torque (b)

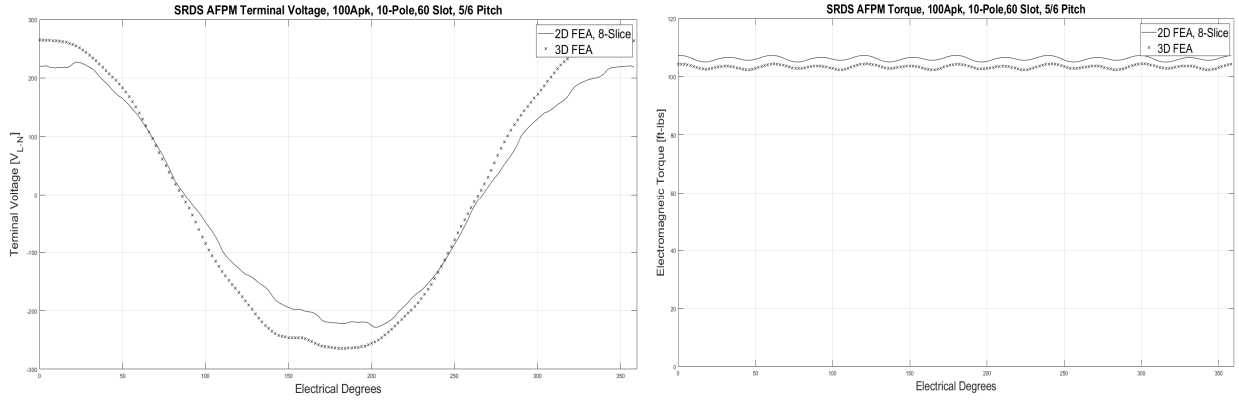

(a) (b)

Figure 74. 2D FEA, 8-Slice Model Terminal Voltage vs 3D FEA Terminal Voltage, 1800 RPM, 100Apk excitation (a), Resulting Electromagnetic Torque (b)

Reviewing Figure 71 we can again see that the 3D FEA model is again predicting and RMS voltage of 129.1 volts, while the 8-Slice 2D FEA is predicting the same 136.2 volts observed using the 2-Slice and 4-slice models, an error of 7.1%. The average electromagnetic torque produced by the 2D, 8-Slice FE model is again 5.6 ft-lbs, versus the 3D FE prediction of 5.3 ft-lbs, and error of 5.6% between the two models.

Presented in Figure 72 we can see that the 3D FE model predicts and RMS voltage of 131.2 volts, while the 8-Slice, 2D FEA is again predicting 136.5Vrms, an error to 4.0%. The average electromagnetic torque produced by the 2D 8-Slice FE model is 14.9 ft-lbs, where-as the 3D FEA is slightly less at 14.1 ft-lbs, an error of approximately 5.7%.

Figure 73 provides a comparison of the stator being excited by 40Apk of current. When excited by this current, the 3D FE predicts an RMS voltage of 145.7 volts, while the 8-Slice 2D FE model predicts 141.5 volts, a difference of 2.9%. The 3D FE model predicts an average torque of 42.5 ft-lbs, where the 8-Slice 2D FE model predicts and average torque of 44.5 ft-lbs, for a difference of 4.7%.

Lastly, Figure 74 looks at the 100A excitation model. When excited by 100A, the 3D FEA predicts a RMS terminal voltage of 198.5 volts, versus the 8-slice 2D model prediction of 165.4 volts, for a difference of 16.7%. While this represents a large increase in terminal voltage variance, the average torque correlation did not parallel this change. The 3D FE model predicts an average torque of 103.3 ft-lbs, versus the 2D FE model prediction of 106.2 ft-lbs, for a variance of only 2.8%.

To further evaluated how the 8-Slice 2D model is representing saturation Figure 75 presents the 2D FEA model's predicted torque constant, Kt, vs. the 3D FEA model prediction and last an analytical prediction which does not include saturation effects.

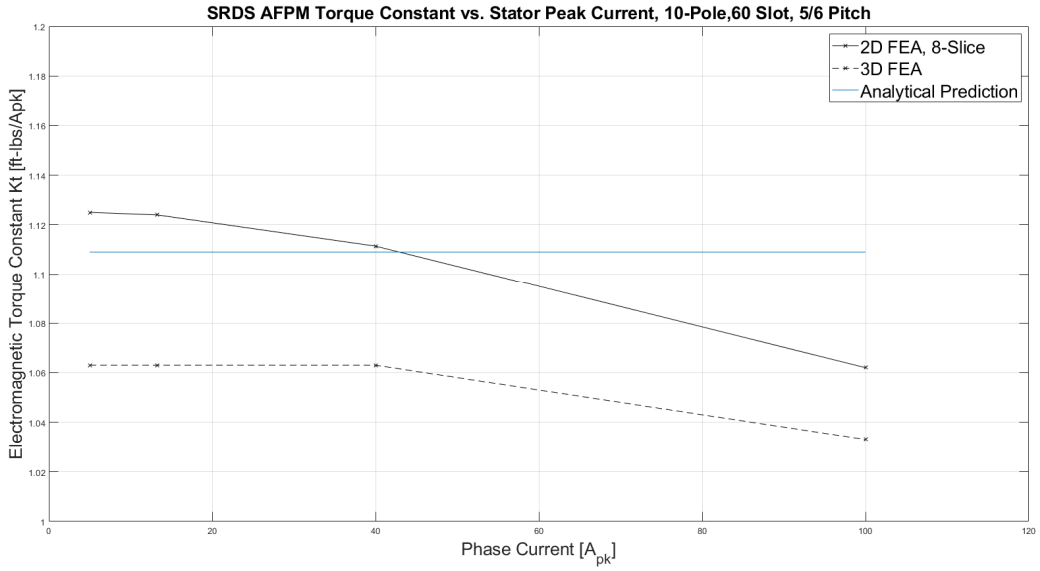

Figure 75. 2D FEA, 8-Slice Model Kt vs. vs 3D FEA Kt vs. Analytical Kt

The last attribute evaluated for the 8-slice 2D FEA model was cogging torque. Figure 76 presents the cogging torque prediction from the 2D 8-slice FEA versus the 3D FEA. Referring to Figure 76 we can see that the 8-Slice, 2D model predicts a quasi-sinusoidal cogging torque, similar to Figure 49 predictions, with an again slightly higher amplitude prediction of 0.69 ft-lbs versus the 3D FEA prediction of 0.54 ft-lbs max.

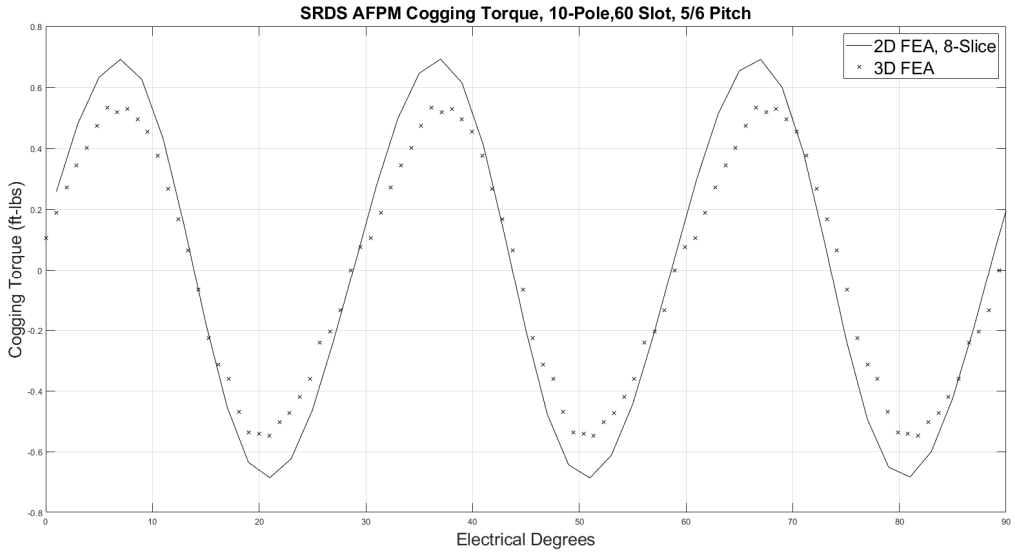

Figure 76. 2D FEA, 8-Slice Cogging Torque vs. 3D FEA Cogging Torque Predictions

The next, and final configuration evaluated was discretizing the SRDS AFPM under consideration into sixteen discrete 2D FEA models, and repeating the same set of analyzes. Below Figure 77 through Figure 85 compare results of 16-slice 2D FEA modeling again 3D FEA and analytic results

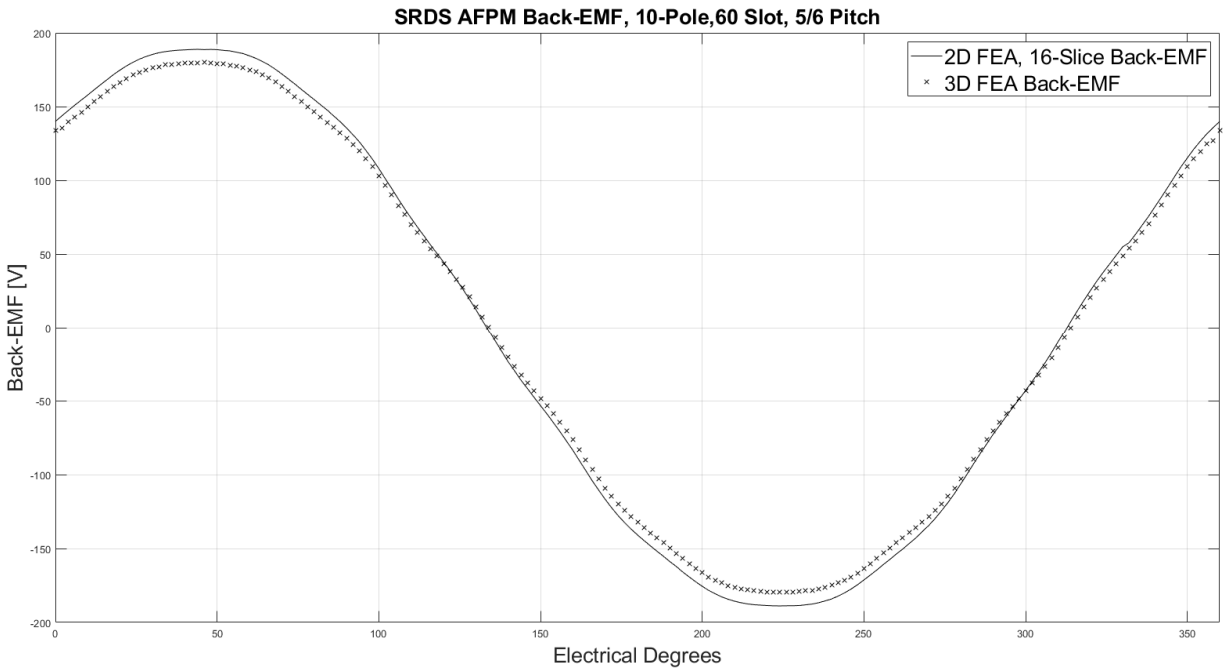

Figure 77. 16-Slice 2D FEA vs. 3D FEA Back-EMF at 1800 RPM

Reviewing Figure 77, we see that the single slice 2D model predicts a peak voltage of 188.8 volts and an RMS voltage of 135.2 volts; compared to the 3D finite element model predictions of 179.8 peak volts and RMS voltage of 128.4 volts at 1800 RPM, a 5.2% difference between the two methods, yielding the best correlation observed using 2D FEA methods.

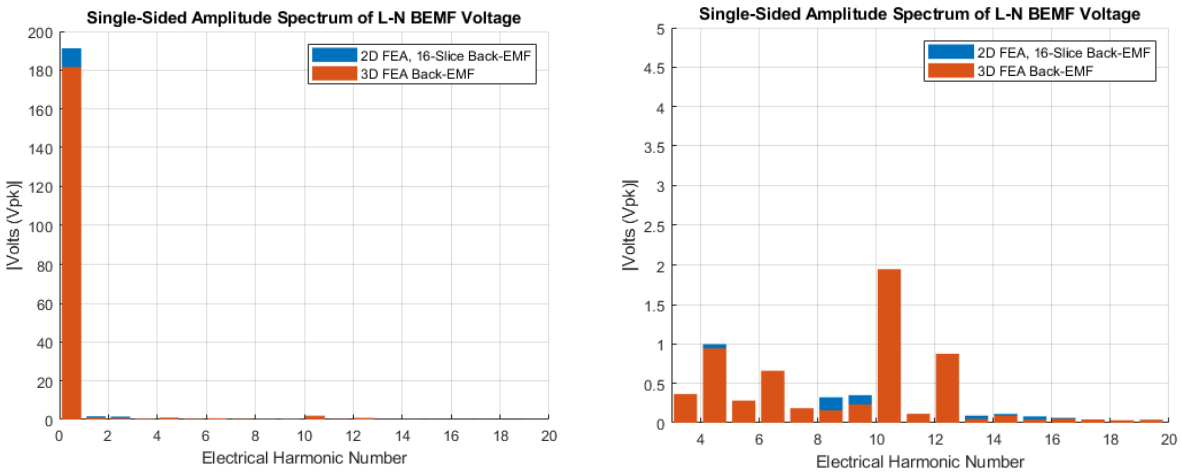

Figure 78. FFT of 2D FEA, 16-Slice Model Back-EMF vs. FFT of 3D FEA Back-EMF at 1800 RPM, (a) 1st through 20th Harmonic, (b) 3rd through 20th Harmonic

The 16-Slice method seems retained the even harmonic content observed in the 4-slice method, again likely a result of combining four different models, with 180 magnetostatic analyses per full sweep. Including even harmonics, the THD prediction for the 16-Slice 2D FEA is 1.48%, removing the even harmonics THD reduces slightly to 1.45%. For comparison, the 3D FEA predicts a THD of 1.31%.

Again, similar to the 2-Slice, 4-Slice and 8-Slice 2D FE models, the 16-Sice 2D representation will not have multiple flux linkages, one for each 2D model. The sum of all the models, again following (4.2) will be used for comparison against the 3D flux linkage prediction. Below Figure 79 presents each of the individual 2D finite element models flux linkage as well as the sum of the 2D model flux linkages and the 3D model flux linkage for comparison. Figure 80 through Figure 83 provide a comparison of performance predictions for the 16-Slice 2D FE and 3D FE models when a sinusoidal stator current of 5A to 100A is applied to that stator terminals.

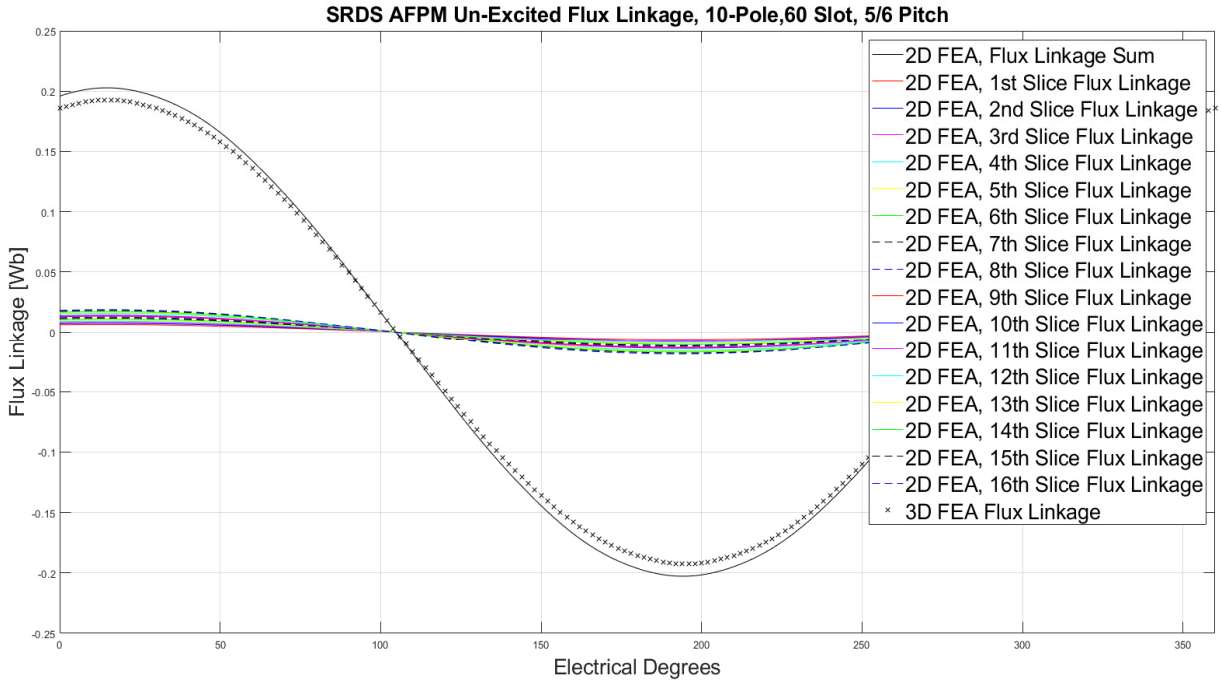

Figure 79. 16-Slice 2D FEA vs. 3D FEA Flux Linkage at 1800 RPM

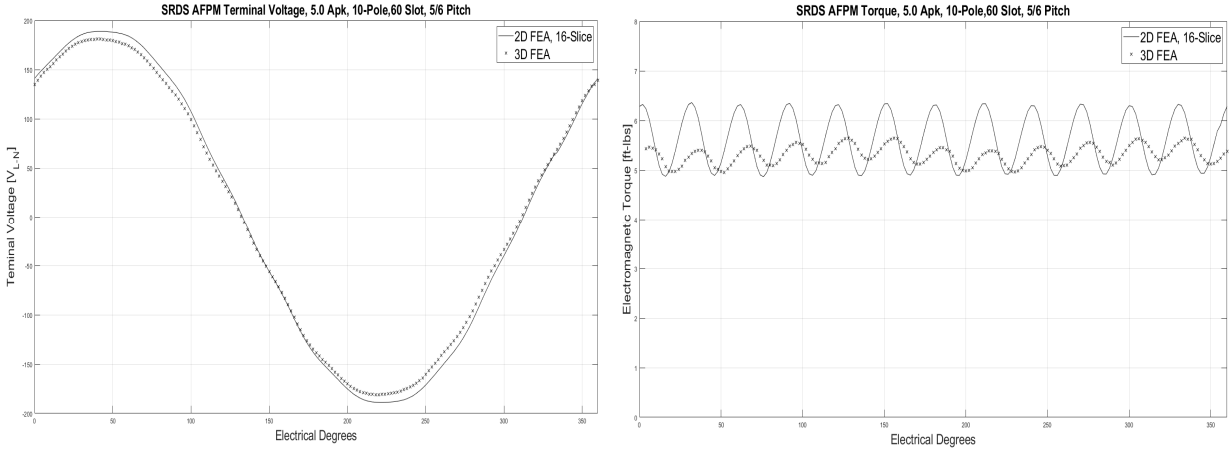

(a) (b)

Figure 80. 2D FEA, 16-Slice Model Terminal Voltage vs 3D FEA Terminal Voltage, 1800 RPM, 5.0 Apk excitation (a), Resulting Electromagnetic Torque (b)

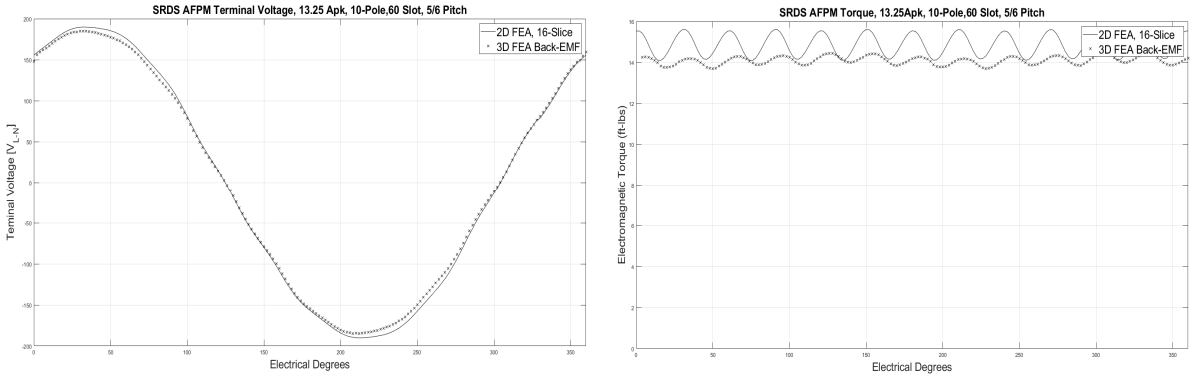

(a) (b)

Figure 81. 2D FEA, 16-Slice Model Terminal Voltage vs 3D FEA Terminal Voltage, 1800 RPM, 13.25 Apk excitation (a), Resulting Electromagnetic Torque (b)

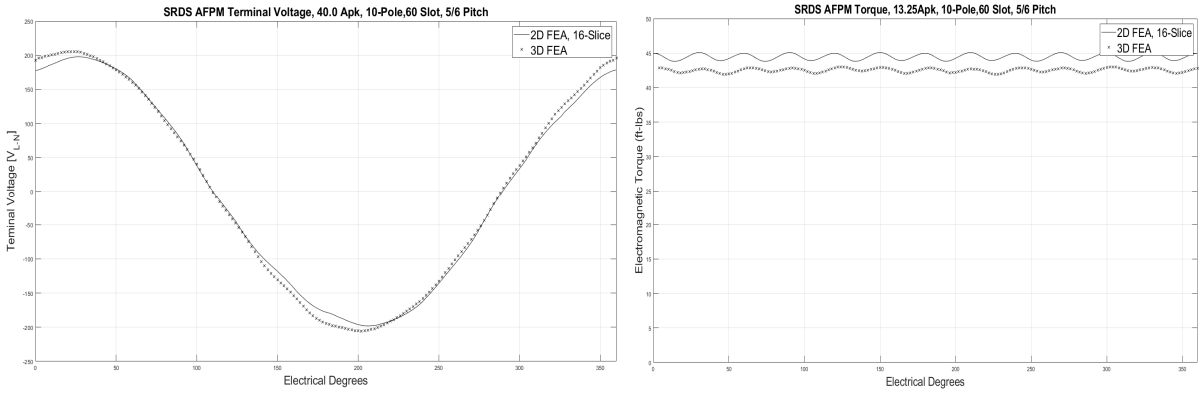

(a) (b)

Figure 82. 2D FEA, 16-Slice Model Terminal Voltage vs 3D FEA Terminal Voltage, 1800 RPM, 40.0 Apk excitation (a), Resulting Electromagnetic Torque (b)

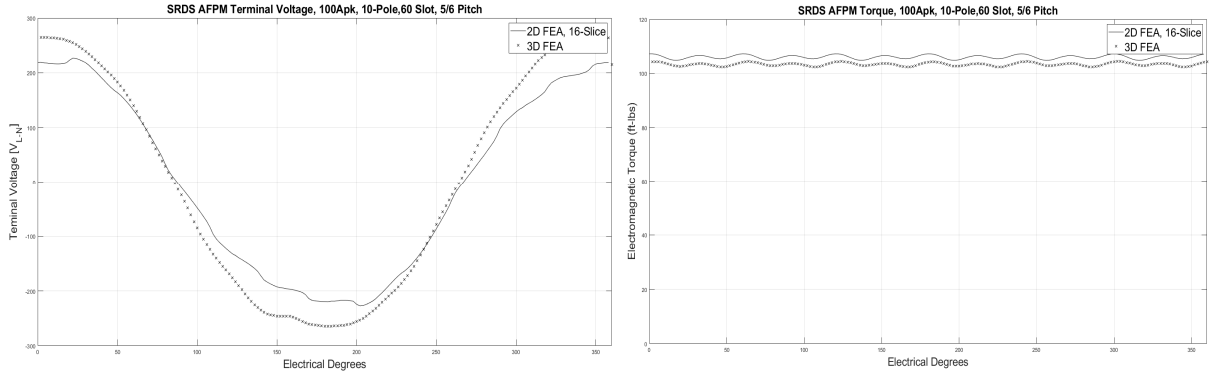

(a) (b)

Figure 83. 2D FEA, 16-Slice Model Terminal Voltage vs 3D FEA Terminal Voltage, 1800 RPM, 100.0 Apk excitation (a), Resulting Electromagnetic Torque (b)

Reviewing Figure 80 we can see that the 2D FEA model is now predicting 135.1 Vrms, and the 3D FEA is again predicting 129.1Vrms, a voltage error from the 16-Slice modeling of 4.6%. The average electromagnetic torque produced by the 2D, 16-Slice FEA model is 5.6 ft-lbs, versus the 3D FEA prediction of 5.3 ft-lbs, an error of 5.6% between the two models.

Reviewing Figure 81 we can see that the 2D FEA model is now predicting an RMS voltage of 135.4 volts and the 3D FEA is again predicting 131.2Vrms, a voltage error from the 16-Slice modeling of 3.2%. The average electromagnetic torque produced by the 2D, 16-Slice FEA model is 14.9 ft-lbs, versus the 3D FEA prediction of 14.1 ft-lbs, an error of 5.6% between the two models.

Reviewing Figure 82 we can see that the 2D FEA model is now predicting 140.5 Vrms, and the 3D FEA is again predicting 145.8Vrms, a voltage error from the 16-Slice modeling of 3.6%. The average electromagnetic torque produced by the 2D, 16-Slice FEA model is 44.5 ft-lbs, versus the 3D FEA prediction of 42.5 ft-lbs, an error of 4.7% between the two models.

Reviewing Figure 83 we can see that the 2D FEA model is now predicting 163.8 Vrms, and the 3D FEA is again predicting 198.2Vrms, a voltage error from the 16-Slice modeling of 17.4%. The average electromagnetic torque produced by the 2D, 16-Slice FEA model is 106.0 ft-lbs, versus the 3D FEA prediction of 103.3 ft-lbs, an error of 2.6% between the two models.

To further evaluated how the 16-Slice 2D model is representing saturation Figure 84 presents the 2D FEA model's predicted torque constant, Kt, vs. the 3D FEA model prediction and last an analytical prediction which does not include saturation effects.

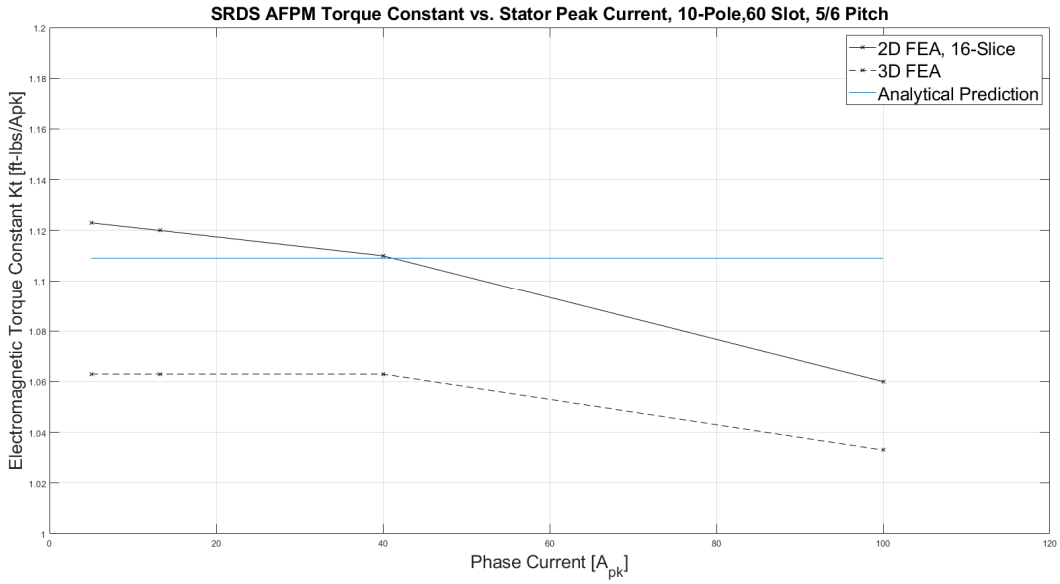

Figure 84. 2D FEA, 16-Slice Model Kt vs. vs 3D FEA Kt vs. Analytical Kt

Lastly, cogging torque was evaluated for the 16-slice 2D FEA model. Figure 85 presents the cogging torque prediction from the 2D 16-slice FEA versus the 3D FEA. Referring to Figure 85 we can see that the 16-Slice, 2D model predicts a quasi-sinusoidal cogging torque, similar to Figure 49 predictions, with an again slightly higher amplitude prediction of 0.74 ft-lbs versus the 3D FEA prediction of 0.54 ft-lbs max.

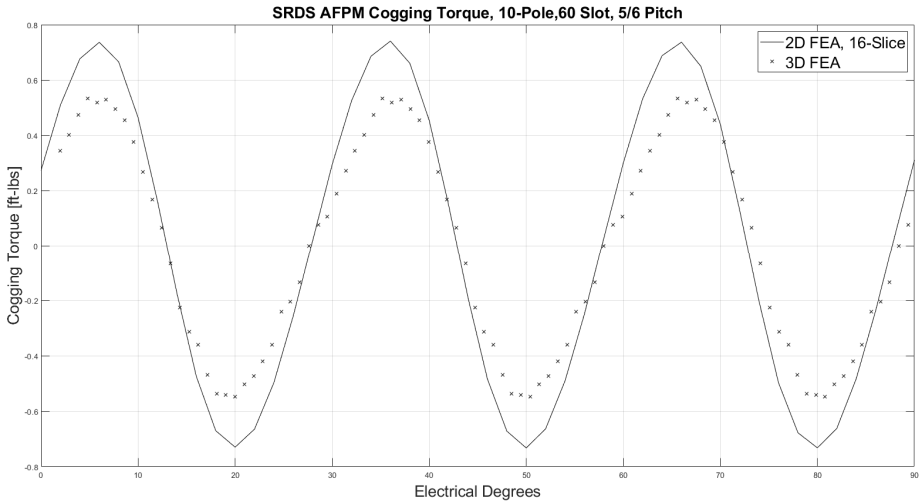

Figure 85. 2D FEA, 16-Slice Cogging Torque vs. 3D FEA Cogging Torque Predictions

5.3.1.1 2D FE Modeling of SRDS AFPM Inductance

In addition to BEMF, cogging torque, loaded electromagnetic torque and terminal voltage, the single plane 2D FE model was utilized to predict motor self-inductance. The single plane 2D model self-inductance was calculated by first measuring the open circuit flux linkage of a single motor phase. After measuring the open circuit flux linkage the same phase was excited with a DC current of 1 ampere. The resulting change in flux linkage divided by the DC current to attain the inductance prediction.

The 2D FE model does account for air-gap and slot leakage components of phase inducatance, but does not include end-turn effects. Analytical inductance predictions as well as analytical end turn calculations were performed using the method described in Section 3.3.4. Table III summarizes and compares the 2D FE self-inductance prediction with 3D and analytical predictions. The 3D FEA model includes end-turn effects and was again excited by 1 ampere of current for prediction of the SRDS AFPM's self-inductance.

Table III. Phase Self Inductance Comparison (2D vs. 3D vs. Analytical)

Phase Self-Inductance				
	Analytical Self-Inductance Prediction [mH]	**2D Finite Element Self-Inductance Prediction [mH]**	**2D Finite Element Self-Inductance with Analytical End Turns [mH]**	**3D FEA Self-Inductance Prediction [mH]**
Prediction	1.592	1.517	1.554	1.547
% Variance From 3D FEA	+2.91%	-1.94%	+0.45%	0.00%

Comparing all of the methods we see that each prediction deviated less than 5% from the 3D FE predictions and that the 2D FE with analytical end-turns was within 0.5% of the 3D FE model predictions. Later, Section 6.3.2 will compare these predictions against a prototype SRDS AFPM.

5.3.2 Unconstrained and Flux Wrapper Full Models:

Section 5.3.1 conducted a thorough analysis of the SRDS AFPM under consideration us properly conditioned and bounded 2D FE models. The following paragraphs summarize results of alternative, geometric implementaitions of suito-boudary conditions present in Section 4.2. Figure 86 presents the results of Back-EMF for each 2D FEA approach versus each other and the 3D FEA model.

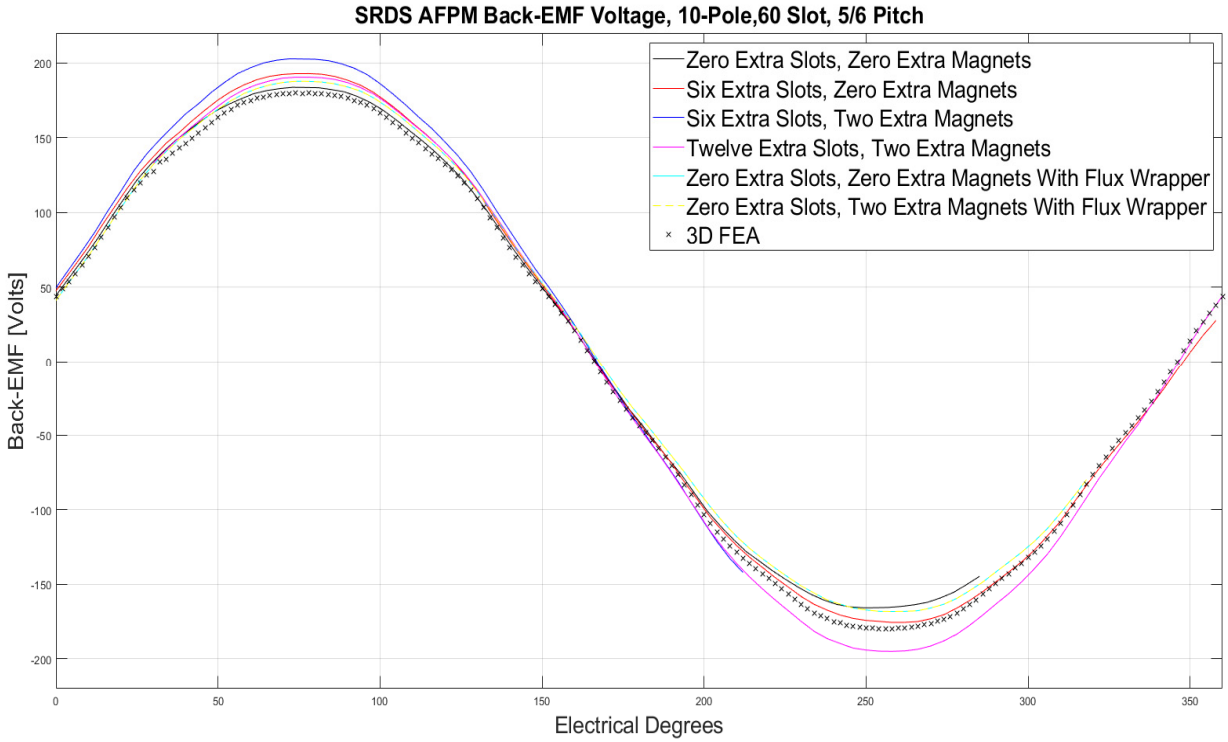

Figure 86. Back-EMF 1800 RPM, Unconstrained and Flux Wrapper 2-D FEA

Studying Figure 86 we see that over the first half cycle of the BEMF waveforms each of the presented approaches produces waveforms which correlated with the 3D FE model, as well as the 2D FE modeling approaches presented in Section 5.3.1 of this thesis. However, over the second half cycle a significant majority of the results become asymmetric, with a change in amplitude, relative to the first half cycle.

Further review of these results illustrates the asymmetry concerns presented in Section 4.2 and associated with improperly conditioned models. All of the presented alternative boundaries produced asymmetric BEMF predictions, including both of the flux wrapper modeling approaches. The closest prediction to that of the 3D FEA was the 2D FE model with 12 additional slots and two additional magnets; in this case the first half cycle reached its maxima at 190.4 volts, with its minima occurring at -195.0 volts. For comparison, the 3D model predicts a peak maximum and minimum voltage of 179.8 volts.

Figure 87 presents the corresponding cogging torque predictions for each of the unconstrained 2D modeling techniques presented in section 4.2. Similar to Back-EMF a significant portion of the results includes some asymmetries, a result of the quasi-boundary conditions applied to each model.

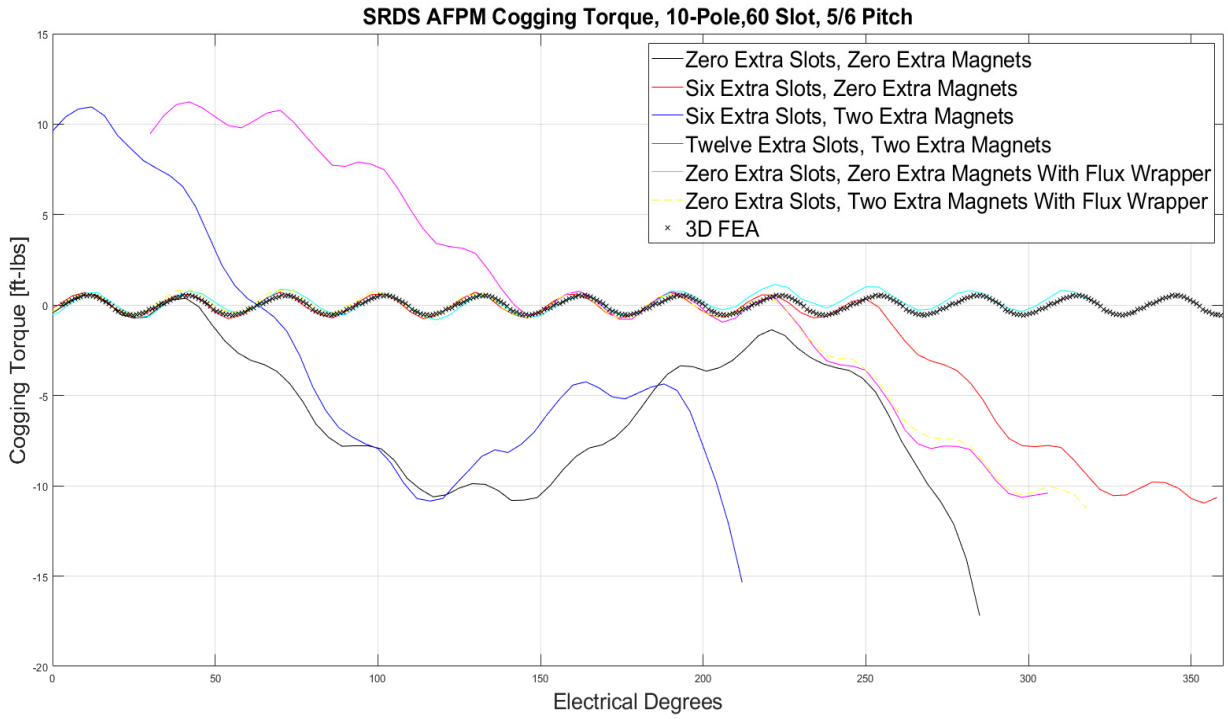

Figure 87. Cogging Torque, Unconstrained and Flux Wrapper 2-D FEA.

Examining Figure 87 we see gross differences in predicted cogging torque from each model, with a few notable exceptions. The 2D FE model with zero extra slots, and zero extra magnets initially trends the 3D FE model, then abruptly dips and oscillates as the magnet moves beyond the extents of the lamination stack. A similar phenomenon appears in the both of the six extra slot model, as well as the 12 extra slot, two extra magnet and zero extra slots, zero extra magnet model with flux wrapper.

However, unlike the BEMF case, adding the flux wrapper, with zero extra magnets increased the accuracy of cogging torque predictions, closer to the 2D FE predictions presented in Section 5.3.1. Below Figure 88

present the same cogging data as was presented in Figure 87, with the x and y-extents adjusted for a closer observation and correlation to previous analyses.

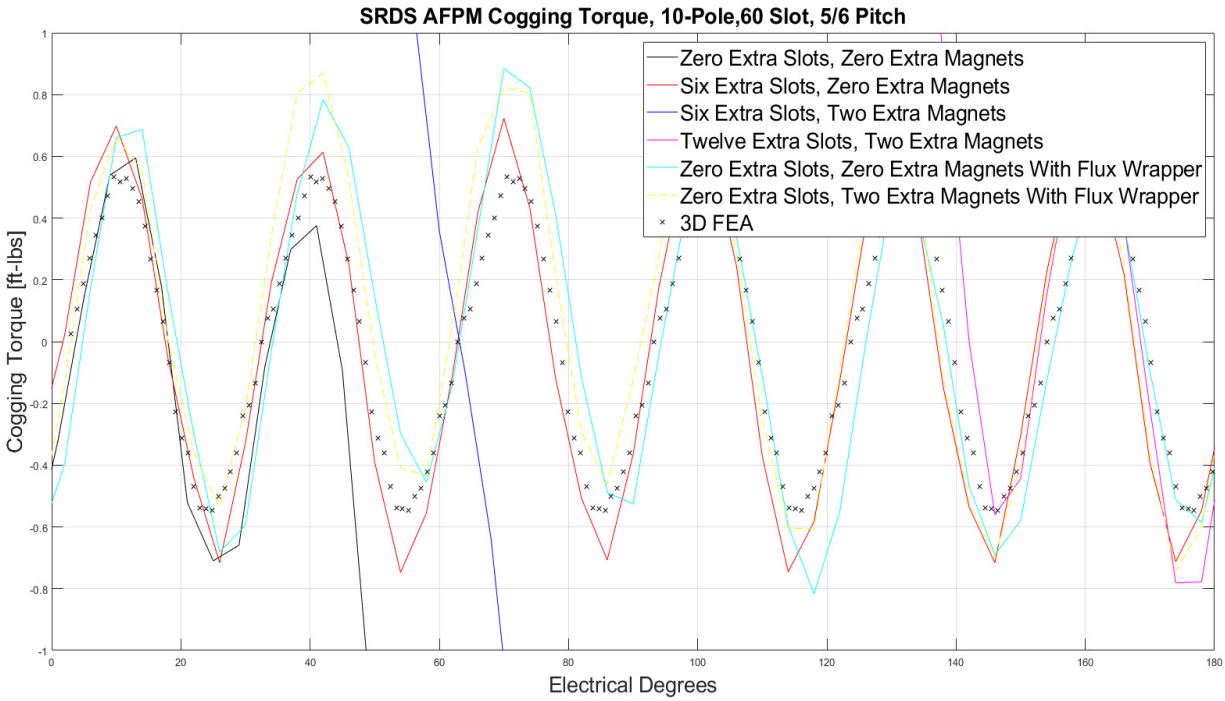

Figure 88. Cogging Torque, Unconstrained and Flux Wrapper 2-D FEA, 0-180 Electrical Degrees

The 2D FE models with suito-boudary conditions applied did not increase the accuracy beyond what was observed using properly bounded models. As such these approaches were not considered for further analysis.

5.4 Discussion of Case Study Results

Chapter 5 has presented analytical as well as 2D and 3D performance predictions for the SRDS AFPM under consideration. While analytical and 2D FE results did not exactly match the precision of the 3D FE results, the rapidness with which these alternative approaches can be conducted, coupled with their ability to provide the design engineer with design insight can be instrumental when selecting an optimal SRDS

AFPM design. The following sub-section provides discussion on the results of Chapter 5 and provide FE computation times.

5.4.1 Performance Comparison

Chapter 5 has presented analytical and 2D FE methods which allow the motor designer to optimize machine performance without the need to generate 3D FE models. These approaches could be especially beneficial and applicable for AFPM Design of Experiment (DOE) and optimization studies. Below, Table IV compares the RMS value of BEMF voltage as well its THD for each discretized, planar 2D FE modeling approach. Figure 89 provides a comparisons of models predicted torque constant for comparison against analytic and 3D FE predictions.

Table IV. Comparison of 2D FEA Voltage Predictions vs. 3D FEA Predictions

1800 RPM Back-EMF Comparison, 2D FE Prediction vs. 3D FE Prediction							
	Analytical	**2D FEA, Single Slice Model**	**2D FEA, 2-Slice Model**	**2D FEA, 4-Slice Model**	**2D FEA, 8-Slice Model**	**2D FEA, 16-Slice Model**	**3D FEA**
RMS Voltage Prediction [Vrms]	134.8	137.2	136.5	136.2	136.2	135.2	128.4
RMS Voltage Error [%]	5.0%	6.8%	6.3%	6.1%	6.1%	5.3%	0.0%
THD Prediction	1.62%	0.99%	1.40%	1.60% / 1.58%[1]	1.65% / 1.62%[1]	1.48% / 1.45%[1]	1.31%
Δ THD	+0.31%	-0.32%	+0.09%	+0.29% / + 0.27%	+0.34% / +0.31%	+0.17% / +0.14%	0.00%

[1] This total harmonic distortion prediction does not include even harmonics. See section 5.3.1 for additional details.

Studying the voltage predictions presented in Table IV, it is evident that the 2D models prediction of RMS voltage increased in accuracy as the number of discretized models increase. When a single slice 2D model is analyzed, the resulting voltage prediction is within 6.8%, however, when 16 individual planar models are used, the voltage error is reduced to 5.3%, a 1.5% reduction in model error. Interestingly, we also see a significant increase in THD correlation between the two modeling approaches.

Again reviewing Table IV, we also see that increasing the number of 2D models from one, to two has a large impact in correlation. When a single 2D model is used for performance predictions, the RMS voltage error is 6.8% and the delta-THD is 0.32%; however, when two average models are used the voltage error

is reduce to 6.5% and the delta-THD to 0.09%. This change in voltage correlation between a single model and two models is so significant it can be visible seen when comparing Figure 42(a) and Figure 50 where a notable increase in waveform harmonic content is present.

The benefit of going from one discrete 2D FE model, to two models is again seen in the torque constant data of Figure 89. Studying this data we see that overall torque constant, Kt, is afforded a significant increase in accuracy, across a 100 amp range of excitation.

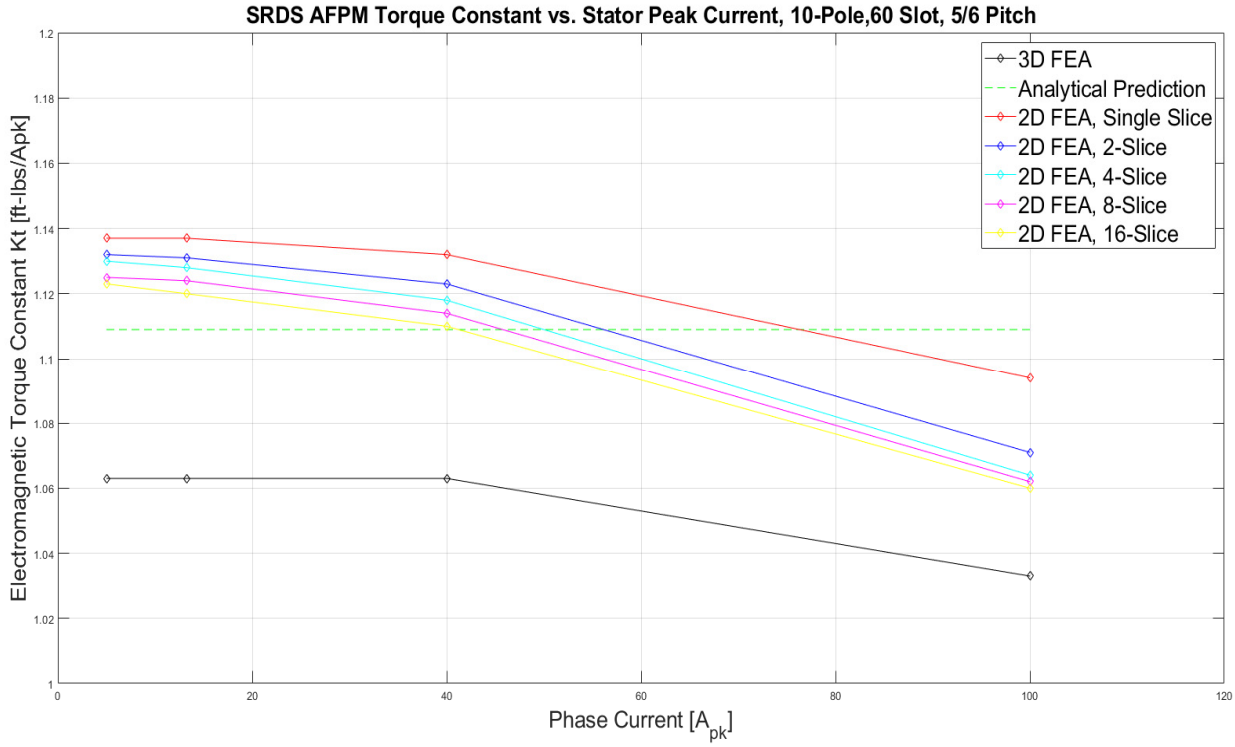

Figure 89. Comparison of all 2D FEA Kt Predictions vs. 3D Kt Predictions vs. Analytical Kt Predictions

Throughout the 2D FE modeling efforts cogging torque was presented. Interestingly the 2D FE model correlation did not improved as the number of models increase. While the 2D FEA did a good job predicting overall shape and frequency of cogging, on a percentage basis the predicted peak value of cogging could have correlated better. The SRDS AFPM under consideration has a relatively low peak value of cogging torque, as such it is not clear if this correlation is actually poor, skewed by a relatively small difference in

torque or if the percentage would remain constant on a machine with higher torque. This is something to be considered in future 2D FE modeling work.

5.4.1.1 Variance between 2D and 3D Modeling Techniques

This thesis has provided analytical evidence that discretized and AFPM into several 2D FE models can provide more accurate performance predictions, than that of a single average 2D FE model. However, this increased accuracy seems to be limited to terminal voltage and torque production, but not cogging torque.

One can hypothesize that this must be a result of 3D effects not captured through utilization of the 2D model. 3D effects of particular suspicion are end effects near the extremities of the rotor and stator lamination stack. In addition to end effects, it is possible that the tapered AFPM stator teeth are allowing magnetic flux to cross the air gap with radial and tangential components, not captured in the magnetic flux. These non-axial, off axis components would reduce the effective flux linked and potentially explaining the 3D FEA's consistently lower prediction of torque per ampere of current and terminal voltage.

5.4.1.2 Software Verification

Throughout this thesis, finite element predictions from two different software packages, using two different solvers have been considered. FEMM utilizes a weighted Maxwell Stress Tensor method [25], [65], [68], [69] where-as Flux 2D and Flux 3D use a Virtual Works method [24], [25], [70] to solve for magnetic forces. Figure 90 present a comparison of single slice 2D FE model BEMF predictions generated using FEMM and Flux 2D, for comparison against Flux 3D BEMF voltage predictions. Figure 91 presents the same comparison, but this time compares the cogging torque predictions from each software package.

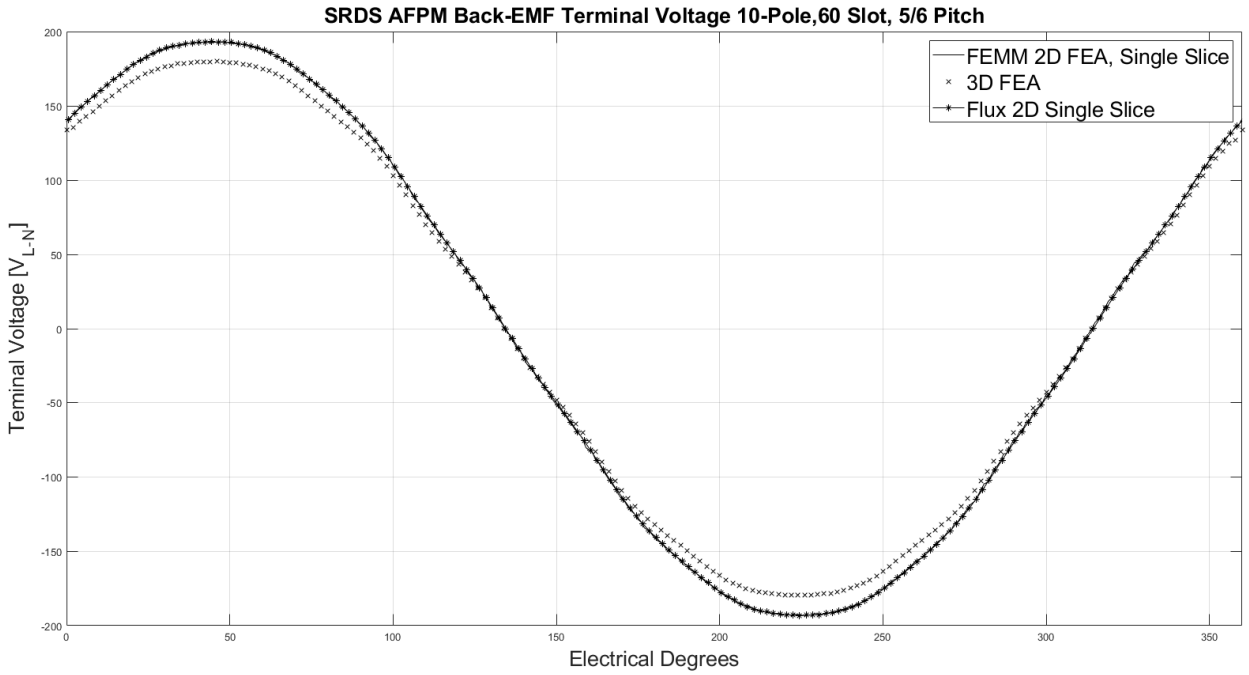

Figure 90. Single Slice FEMM 2D FEA vs. Single Slice Flux 2D FEA vs. 3D FEA Back-EMF at 1800 RPM

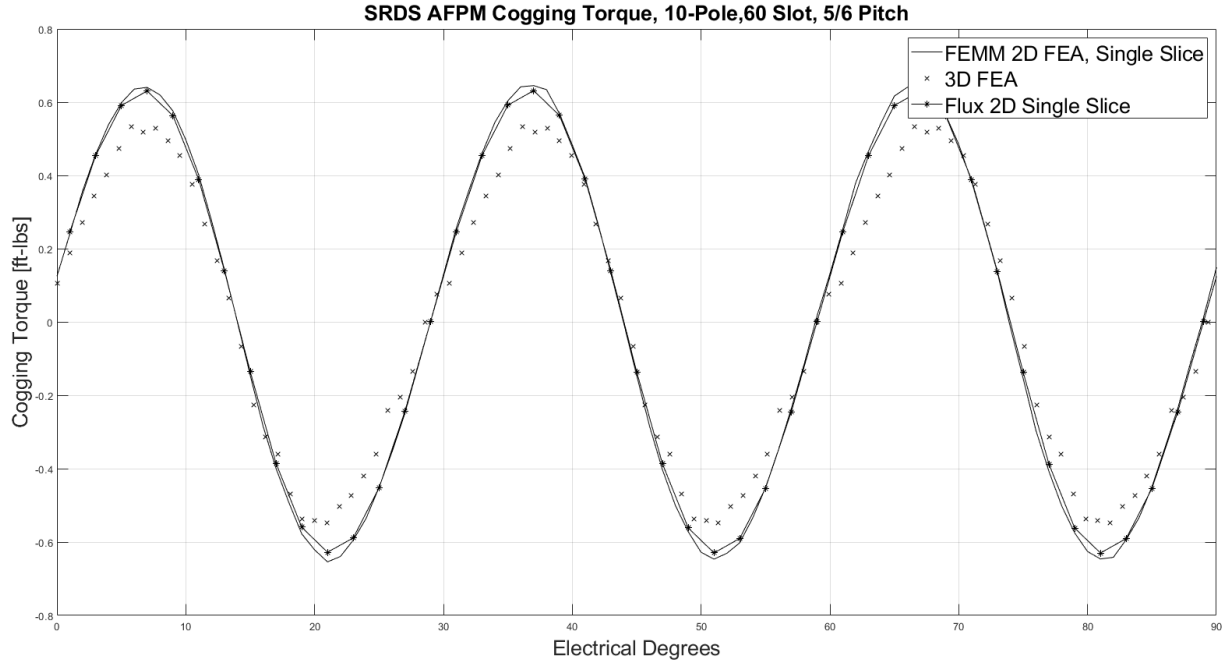

Figure 91. Single Slice FEMM 2D FEA vs. Single Slice Flux 2D FEA vs. 3D FEA Cogging Torque

Comparing the Flux 2D and FEMM 2D FE BEMF predictions of Figure 90 it is difficult to see any variation between the two methods, as the two data sets lie almost directly on top of each other. FEMM predicts a maximum BEMF voltage of 193.2 volts and RMS BEMF voltage of 137.1 Volts. Flux 2D predicts a peak BEMF voltage of 193.1 Volts and an RMS voltage of 137.2 volts. The RMS voltage error between the two predictions is less than 0.1%, indicating good overall correlation between the two software packages.

Cogging torque predictions offer a very similar correlation between both 2D FE modeling software packages. Reviewing Figure 91 we see that Flux 2D predicts a peak cogging torque of 0.63 ft-lbs, where-as FEMM predicts peak cogging of 0.64 ft-lbs, resulting in a prediction difference of 0.01 ft-lbs between the two software packages. This trend of correlation continued as the Flux 2D Model was excited with the same phase currents used in FEMM, below Figure 92 presents a comparison of the two methods terminal voltage while Figure 93 compares predicted torque.

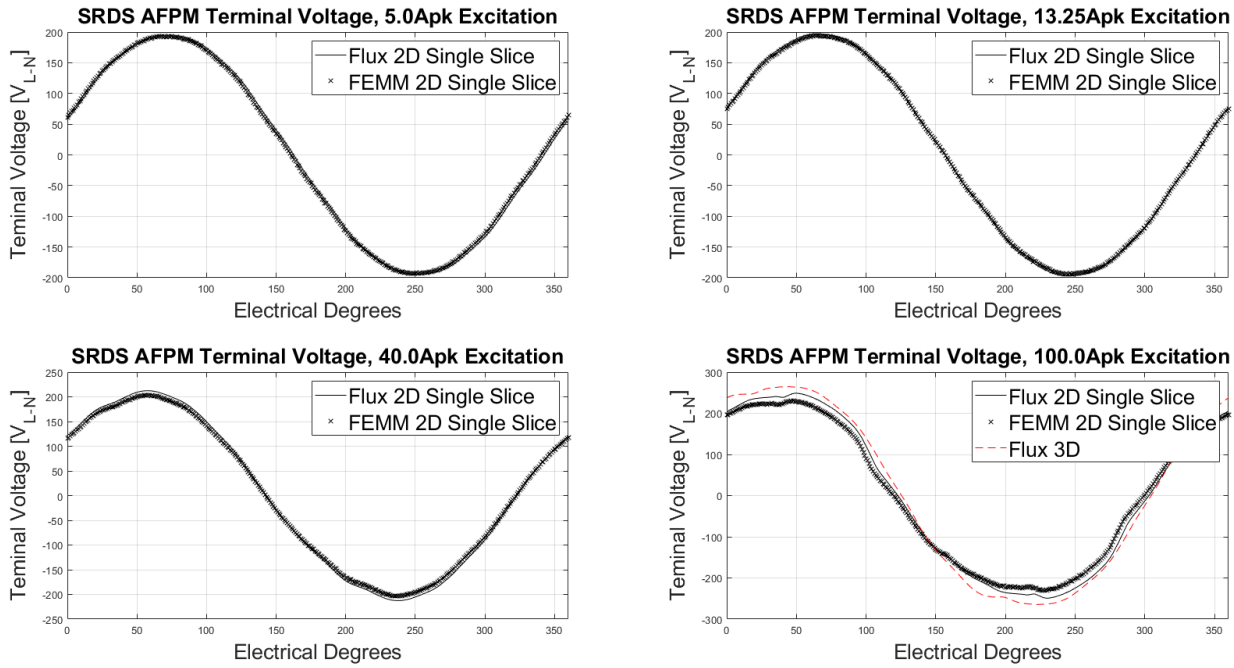

Figure 92. SRDS AFPM Loaded Terminal Voltages, Flux 2D vs. FEMM

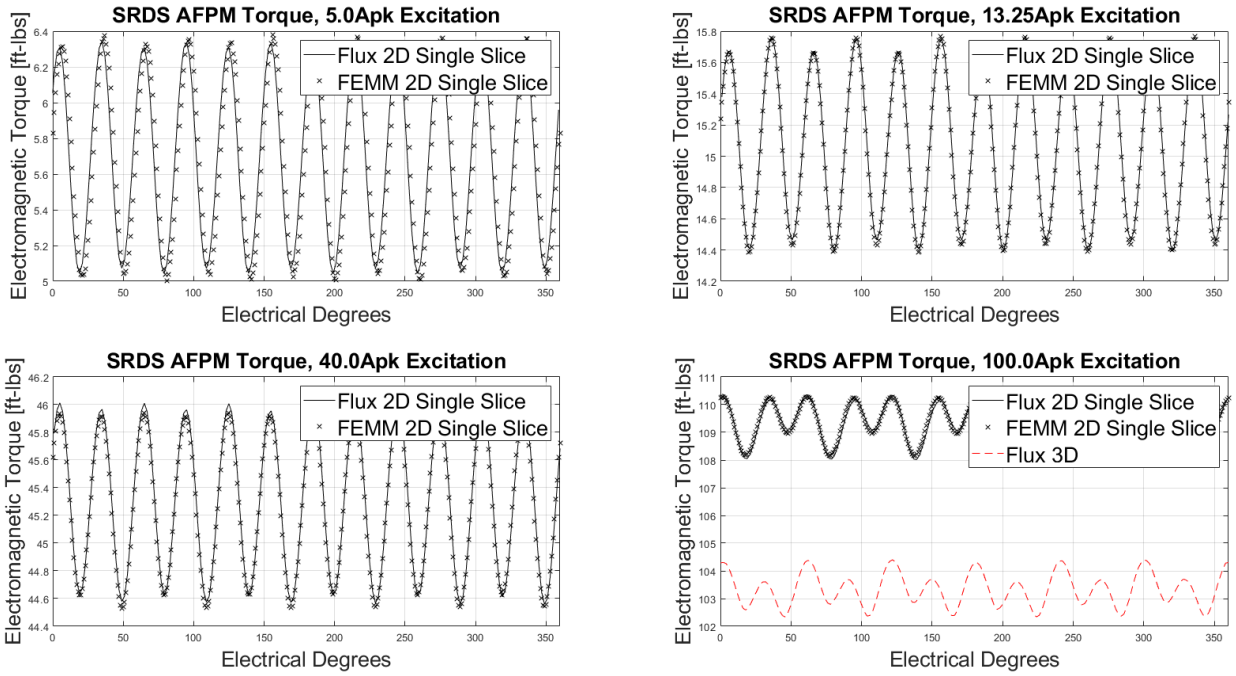

Figure 93. SRDS AFPM Electromagnetic Torque, Flux 2D vs. FEMM

Studying Figure 92 and Figure 93, the two software packages predicts the same resulting average torque, same torque waveforms and nearly the same voltage waveforms. Under heavy saturation a slight deviation in predicted voltage is observed in the 100Apk case. This could be a result of the two different solvers, or perhaps a consequence of FEMM's magnetostatic analysis vs. the true transient magnetic analysis being conducted with Flux 2D. Overall the two different software packages produced nearly identical results, validation the use of FEMM and verifying accuracy of the reported 2D results.

5.4.2 Analysis Computation Time

One of the most significant benefits of conducting 2D FE predictions is the significant reduction in computation time required to run each mode. Each of the analysis presented in this thesis were conducted with a computer with the following specifications.

Table V. Computer Hardware Used For Analysis

Machine Used to Perform Analysis			
Parameter	***Value***	***Parameter***	***Value***
CPU	Intel Xeon(R) E5-2643 v3	Operating System	Windows 10 Enterprise
Dedicated CPU Cores	2 (Cores)	RAM	128 (GB)

Each of the presented finite element analysis runs times were conducted at 2 electric degree increments and swept for 360 electrical degrees. Using the computer hardware defined in Table V, approximate computational times for each modeling method, including the time to generate mesh are presented in Table VI.

Table VI. Approximate Computation Time of Each Analysis Method

Approximate Analysis Computation Time					
	Analytical	**2D FEA, Standard Mesh**	**2D FEA, Fine Mesh**	**3D FEA, Standard Mesh**	**3D FEA, Fine Mesh**
Analysis Computation Time	< 1 (Sec)	< 5 (min) per model	< 25 (min) per model	< 4 (hours)	< 60 (hours)

The 2D and 3D models were analyzed using coarse and fine mesh. Coarse mesh refers to models with physically larger mesh elements than the fine mesh model, and were used to analyze cogging torque. Reviewing Table VI it clear that conducting 2D models has the potential to save significant computation time over 3D FE model and that analytical solutions will reduce computation time even further. Also noteworthy is that when discretizing the SRDS AFPM into multiple the analysis computational time did not simply multiply by the quantity of models. A single Instance of FEMM did not take advantage of multiple CPU cores, however FEMM did respond well to running multiple software instances. In cases where multiple FEMM instances were run in parallel there was not an appreciable increase in computational time.

5.5 Summary of SRDS AFPM Modeling Efforts

Chapter 5 has presented a case study which includes several analysis techniques for analyzing a SRDS AFPM. The first portion of this chapter defined the SRDS AFPM under evaluation and provided analytical

estimates of machine performance for comparison against 3D FE predictions. Initial analysis results show that the analytical waveform predictions of RMS voltage as well as the analytical estimate of phase self-inductance were within 5% of 3D FE predictions.

The next portion of Chapter 5 reviewed 2D FE modeling of the SRDS AFPM through utilization of a planar model or series of planar ("Slice") models for prediction of motor performance. This section provided validation that modeling an SRDS AFPM in 2D provides reasonable accuracy, relative to 3D FE and evidence that discretizing the AFPM into multiple 2D models can improve prediction accuracy relative to overall machine torque production as well as voltage harmonic predictions. Additionally, 2D FE predictions of phase self-inductance were conducted, yielding results within 2% of 3D predictions and within 0.5% of 3D predictions with the addition of analytical end turn inductance, validating the use 2D modeling for prediction of SRDS AFPM motor self-inductance.

The last portion of Chapter 5 evaluated alternative, suito-boudary conditions approaches to modeling SRDS AFPMs in 2D. This section concluded that alternative modeling approaches do not result in increase correlation with 3D FE modeling predictions and often lead to asymmetric waveform predictions.

Chapter 6

Experimental Results

This section will present performance test results for the case study for a SRDS AFPM presented in Chapter 5. This chapter will first start by describing the machine under test. Subsequent sections will use the documented test methods and setups used to perform evaluation testing. Lastly this chapter will summarize testing results and accuracy relative to the analysis techniques developed in this thesis.

6.1 Prototype SRDS AFPM Characteristics

The machine under test is the same 5hp, 1800 RPM machine present in Section 5.1. The machine consists of two M-10x silicon steel tape wound cores, random copper windings and ten N48H NdFeB magnets nestled inside of a stainless steel rotor assembly. The machine under test is shown below in Figure 94.

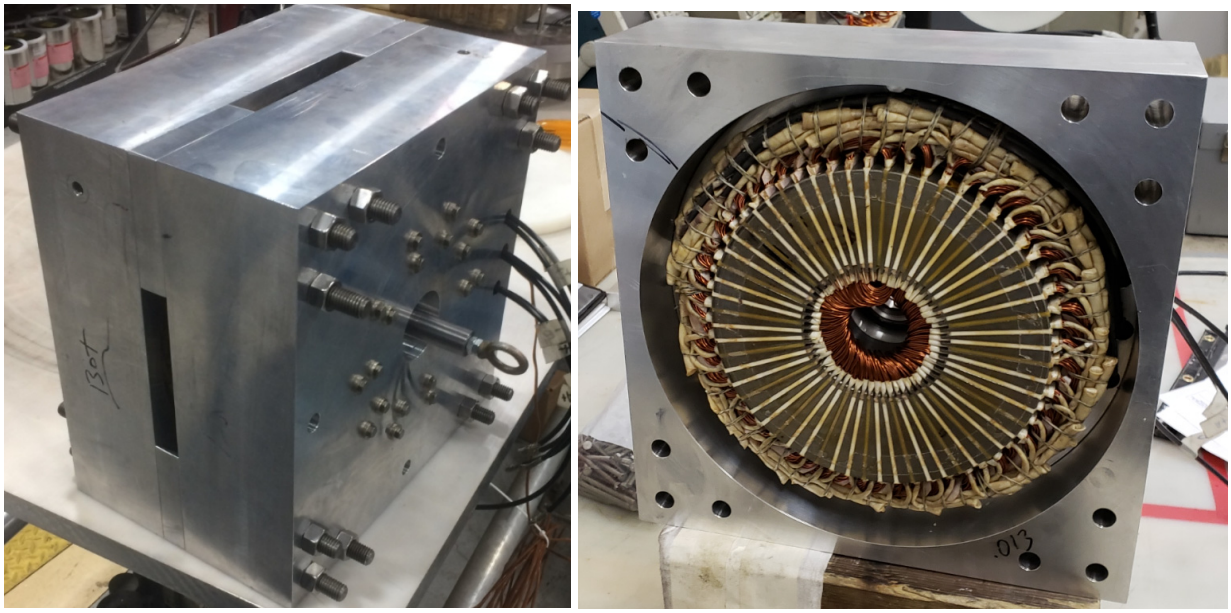

(a) (b)

Figure 94. Prototype 10-Pole, 60-Slot, SRDS AFPM Assembly (a), One of the SRDS AFPM Stators Before Assembly (b).

6.2 Machine Performance Testing: Setup and Test Conditions.

Testing of the SRDS AFPM took place in three different configurations. The first configuration was for static tests, where the motor was placed on a laboratory bench and static tests were conducted (e.g. inductance and resistance measurements). The second test setup utilized was a back to back setup where the SRDS AFPM was driven by an induction motor for the purpose of capturing BEMF measurements at constant speed. The last test setup was used to load the SRDS AFPM and capture measurement of motor efficiency and phase current data. The BEMF test setup is shown in Figure 95, the loaded test arrangement is shown in Figure 96 and a single line diagram describing the loaded test arrangement is provided in Figure 97.

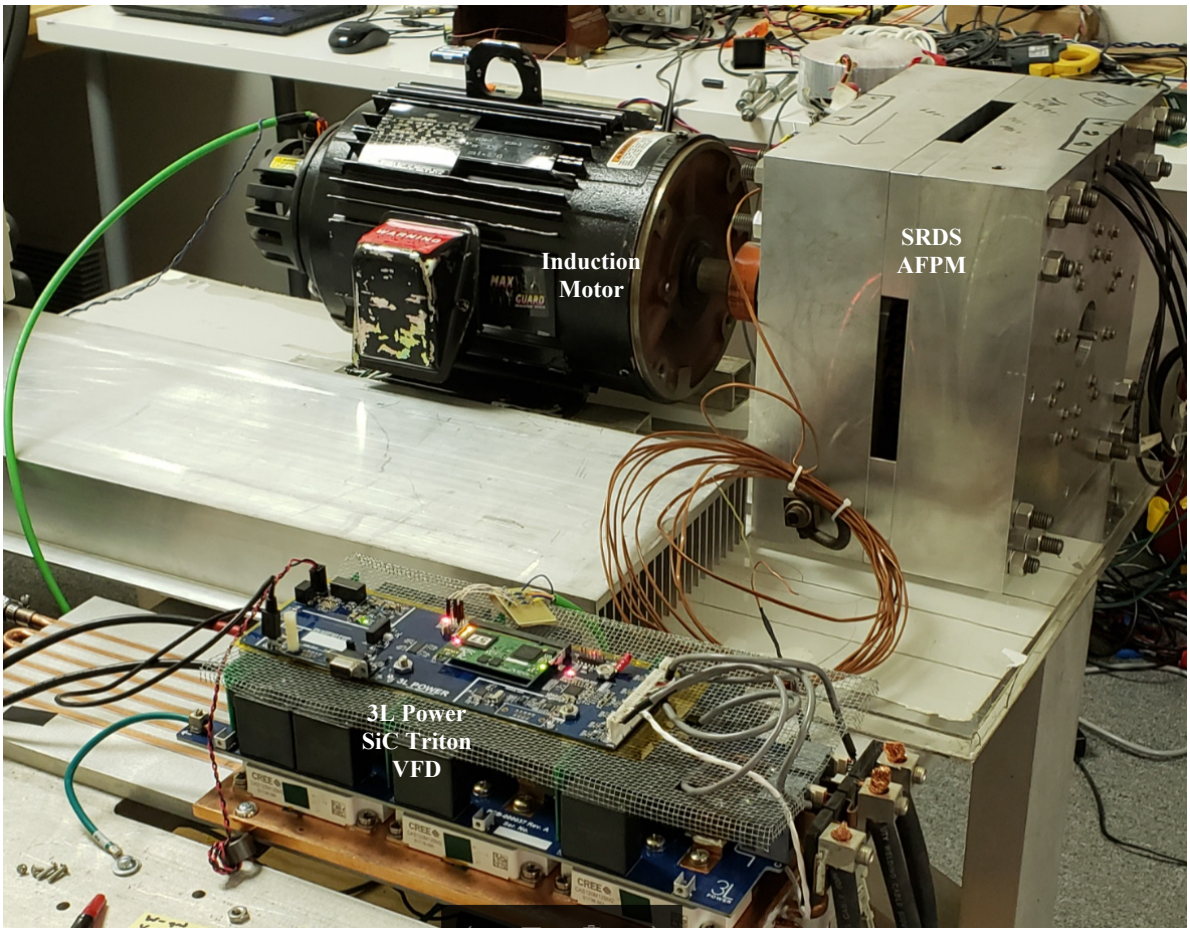

Figure 95. SRDS AFPM Back-EMF Test Setup

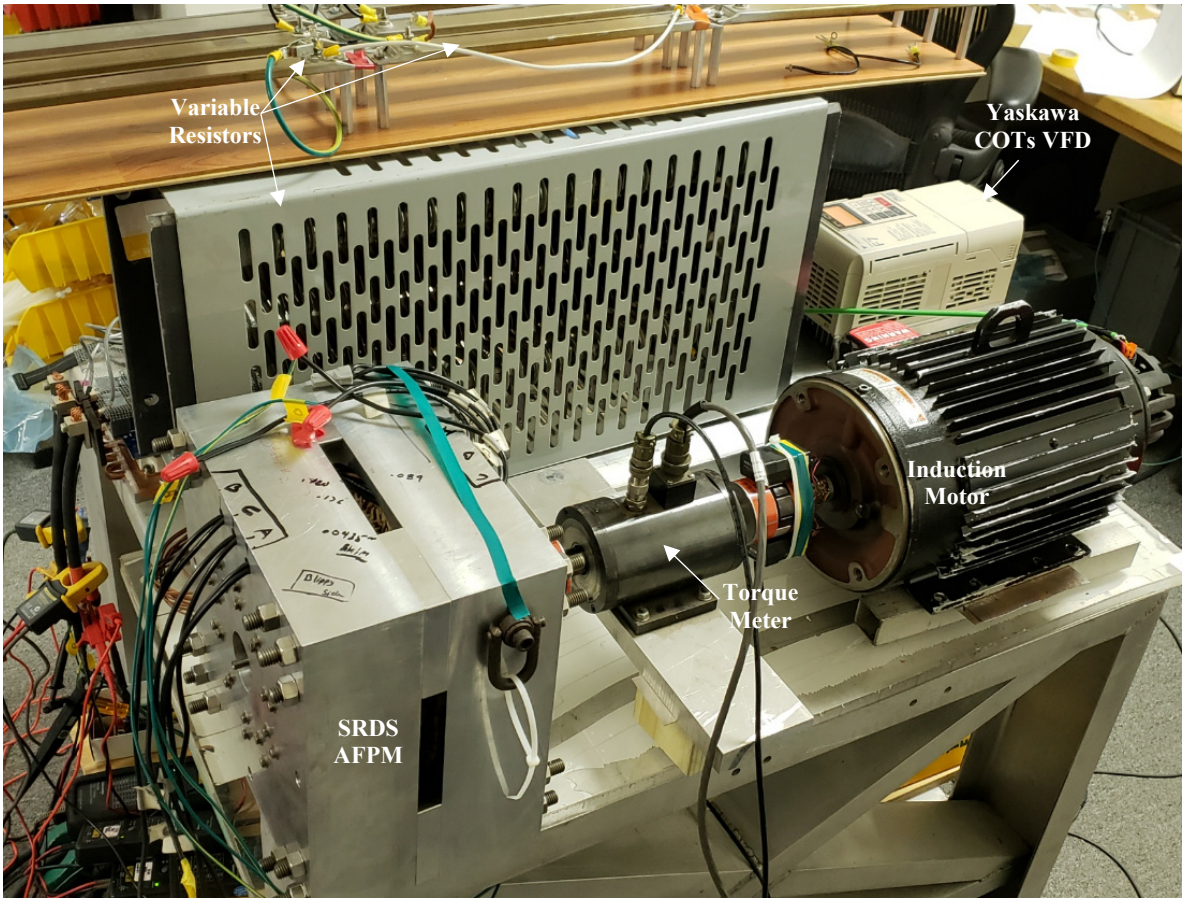

Figure 96. SRDS AFPM Load Testing Test Setup

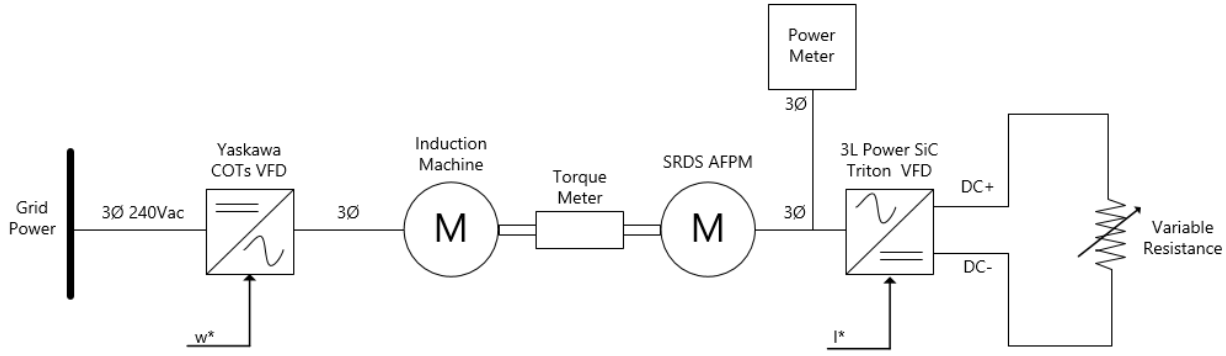

Figure 97. SRDS AFPM Load Testing Single Line Diagram

6.3 Unloaded Machine Measurements

6.3.1 Back-EMF Test Data

BEMF Measurements were taken with the SDRS AFPM being driven by an induction motor, using the test setup shown in Figure 95. The average BEMF voltage was measured at 165 RPM and Ranged from 11.21 to 11.66 Volts, resulting in an average machine electrical constant of 0.0695 Vrms / RPM. Figure 98 presents the measured BEMF data for Stator 1 Phase A and B, and Stator 2 Phase B and Figure 99 is the FFT of stator 1, Phase A BEMF Voltage. The measured THD, following Equation (5.1) was 1.80%.

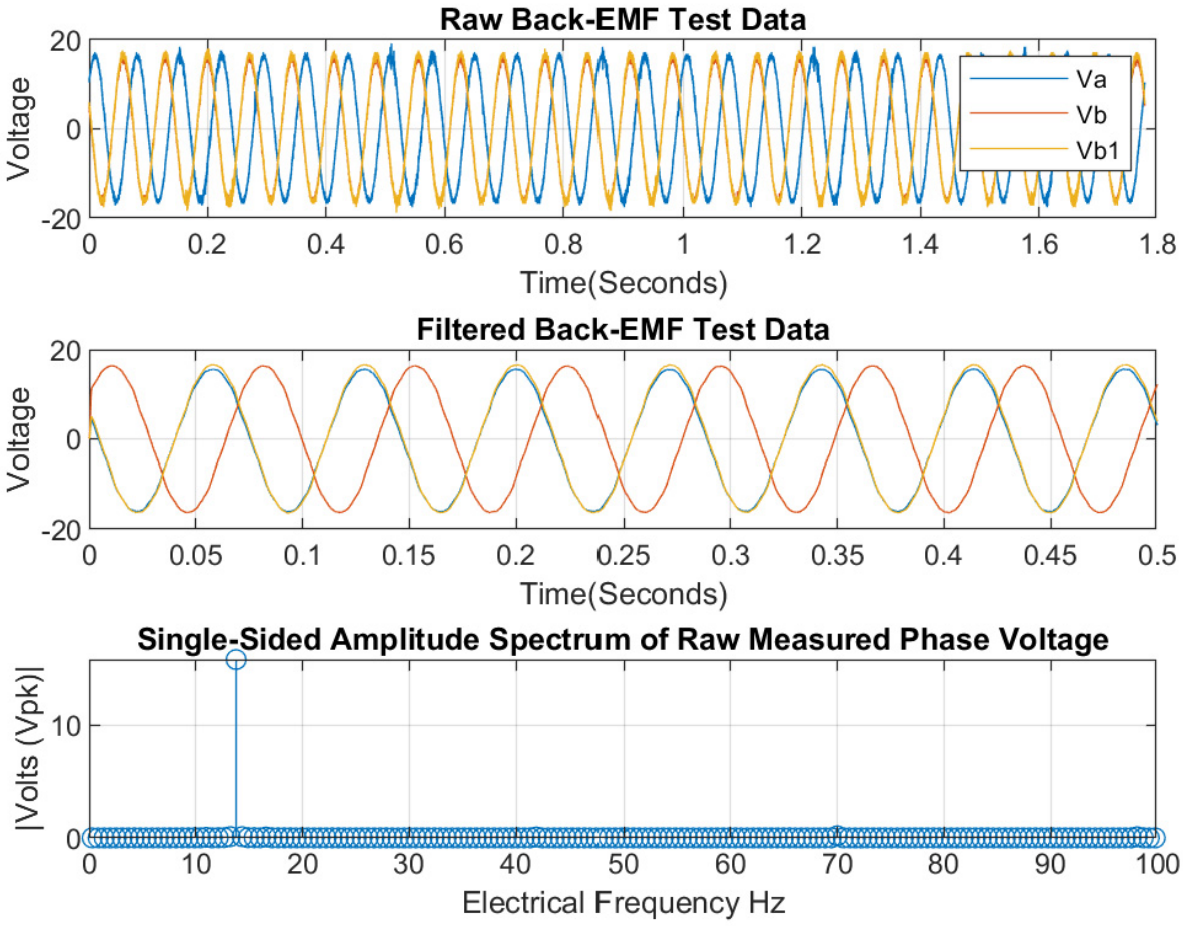

Figure 98. SRDS AFPM BEMF Test Data and FFT

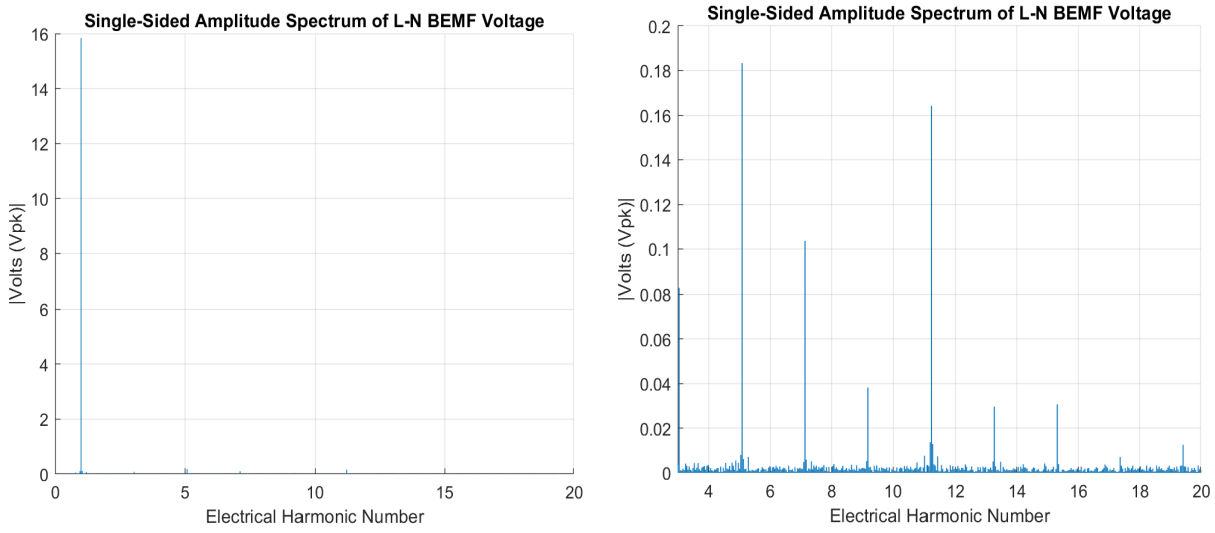

(a) (b)

Figure 99. FFT of Measured Back-EMF Data at 1800 RPM, (a) 1st through 20th Harmonic, (b) 3rd through 20th Harmonic

6.3.1.1 Discussion of Back-EMF Results

The measured average voltage constant of 0.0695 Vrms / RPM presented in Figure 98 correlates well to the analytic, 2D and 3D FE results. Below Table VII provides a comparison of each presented analysis method's prediction of BEMF voltage versus the averaged measured motor prediction, using its measured voltage constant.

Table VII. Comparison of Predicted Back-EMF Voltage at 1800 RPM.

1800 RPM Back-EMF Prediction					
	Analytical [Vrms]	**2D FEA, Single Slice Model [Vrms]**	**2D FEA, 16-Slice Model [Vrms]**	**3D FEA [Vrms]**	**Test Ke [Vrms]**
Prediction	133.6	137.2	135.2	128.4	125.1
% Error From Test	+6.79%	+9.67%	+8.07%	+2.64%	0.00%

Reviewing the spectral content of the BEMF data, we see that there is a large contribution of harmonic context which exists in the 5th, 7th, 11th and 13th electrical harmonics. This observation matches those of analytical, 3D and all of the 2D models results presented, indicating that all methods are capturing the

machine space harmonics accurately. Below, Table VIII presents a comparison of the predicted BEMF THD from analytical, 3D and multiple 2D FE modeling techniques.

Table VIII. Comparison of Back-EMF Total Harmonic Distortion Predictions

1800 RPM Back-EMF – Total Harmonic Distortion Prediction						
	Analytical [%]	**2D FEA, Single Slice Model [%]**	**2D FEA, 2 Slice Model [%]**	**2D FEA, 16-Slice Model [%]**	**3D FEA [%]**	**Measured [%]**
Prediction	1.62%	0.99%	1.40%	1.48%	1.31%	1.80%
Variance From Measurement	-0.18%	-0.81%	-0.40%	-0.32%	-0.49%	0.00%

The measured THD is slightly higher than all prediction methods, with the analytical THD prediction and the 16-Slice 2D FEA modeling efforts producing the closest overall correlation to test measurement. Interestingly, increasing the number of 2D FEA slices does appear to have a positive impact on increasing correlation of voltage harmonics to those measured, with 2-slice 2D modeling correlating closest with 3D modeling efforts and 16-slice correlating most closely with measured test data.

6.3.2 Inductance and Resistance Testing

In additional to BEMF data, the prototype AFPM's inductance was measured using a Chroma Brand LCR Meter, Model 11025. Results of LCR meter testing are presented in Table IX, where we can see that the predicted 2-D finite element falls within the distribution of measured inductances, and within five percent of the average measured phase inductance when analytical end turns inductance is considered.

Table IX. 2-D AND 3-D FINITE ELEMENT SELF-INDUCTANCE (1A EXCITATION) VS. TEST MEASURED SELF-INDUCTANCE @ 100HZ

2-D Finite Element Self-Inductance [mH]	**2-D Finite Element Self-Inductance with Analytical End Turns [mH]**	**3-D Finite Element Self-Inductance [mH]**	**Measured Self-Inductance [mH]**						
2-D	**2-D**	**3-D**	**Phase A**	**Phase B**	**Phase C**	**Phase A1**	**Phase B1**	**Phase C1**	**Average Test Measurement**
1.517	1.554	1.547	1.58	1.52	1.70	1.58	1.69	1.66	1.62

Using the same LCR meter, resistance was also measured for all motor phases. Results of resistance measurements are presented in Table X, where we can see that the analytical prediction of motor resistance is within 11.3% of the averaged measured result. Analytical estimates of motor phase resistance were produced using the equations derived in Chapter 4. Finite element predictions of phase resistance were not conducted, and thus not reported for comparison.

Table X. Analytic Phase Resistance vs. Test Measured Resistance @ 100Hz

Analytical Phase Resistance [mΩ]	**Measured Phase Resistance [mΩ]**						
Analytic	**Phase A**	**Phase B**	**Phase C**	**Phase A1**	**Phase B1**	**Phase C1**	**Average Test Measurement**
0.581	0.519	0.503	0.532	0.521	0.526	0.533	0.522

6.3.2.1 Discussion of Inductance and Resistance Results

In general all of the inductance predictions correlated well with the measured test results. The 2D and 3D results were strikingly similar, especially once analytic end turns were added to the two dimensional results, indicating that 2D and 3D models are representing the motor geometry accurately. Note that the 2D single pole model and full motor model produced nearly identical inductance predictions and thus no differentiation was made between the two models. Refer to Section 5.3.1.1 for further discussion on the 2D model inductance results.

6.4 Experimental Machine: Load and Efficiency Testing

Efficiency measurements were taken while the SDRS AFPM was loaded by an induction motor driven by a COTs Yaskawa Variable Frequency Drive [23]. While the Yaskawa COTs VFD was used to regulate speed, the SRDS AFPM was being operated in current control mode through 3L Power brand SiC Triton VFD and Atlas control board. The Triton VFD's DC link was couple to a variable set of resistors, slightly loading the SRDS AFPM and ensuring the Triton DC link did not experience transient voltages beyond its rating. Between the induction motor and the SRDS AFPM a Honeywell Model 1604-1K inline torque meter was installed to measured generated torque. In this test arrangement the SRDS AFPM was operated

in generating mode, on three of six available phases. This test arrangement limited the speed range of test and the parasitic load resistors also limited the torque control. The efficiency and load test configuration is shown in Figure 96, and described through a single line diagram in Figure 97. Efficiency test results are presented below in Figure 100; while efficiency testing was conducted, measurement of the SRDS AFPM's torque constant was also measured and is presented in Figure 101.

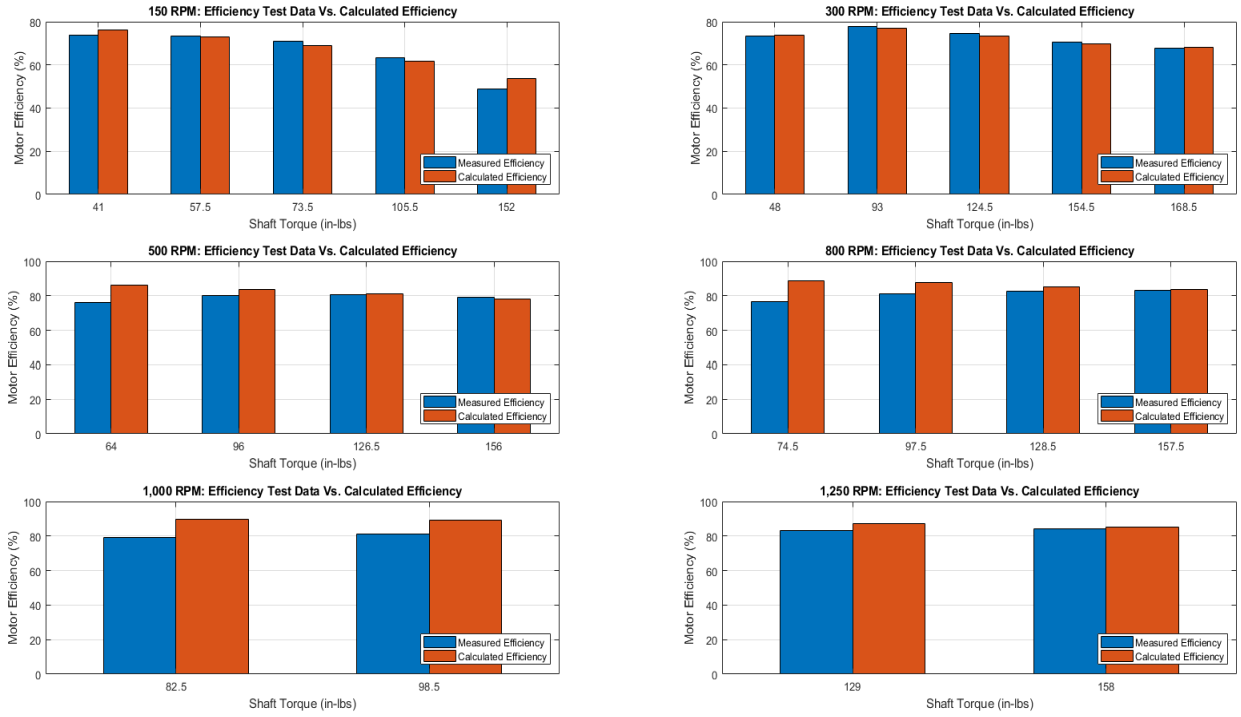

Figure 100. SRDS AFPM Efficiency Measurement vs. Prediction

The efficiency calculations presented for comparison against test data in Figure 100 were conducted analytically following the process and equations developed in Section 3.3.5. These calculations account for the fact that the motor was operating on only three phases, through removal of the stator factor of 2 in equation (3.49) and by including parasitic core losses in the inactive stator, excited by the magnet's magnetic flux passing the core. The inactive stator's magnetic flux was assumed uninfluenced by the active

stator's armature reaction, where-as the active stator's armature reaction was assumed to be orthogonal to that of the magnet field, thus the armature flux was added in quadrature to that of the magnet's field.

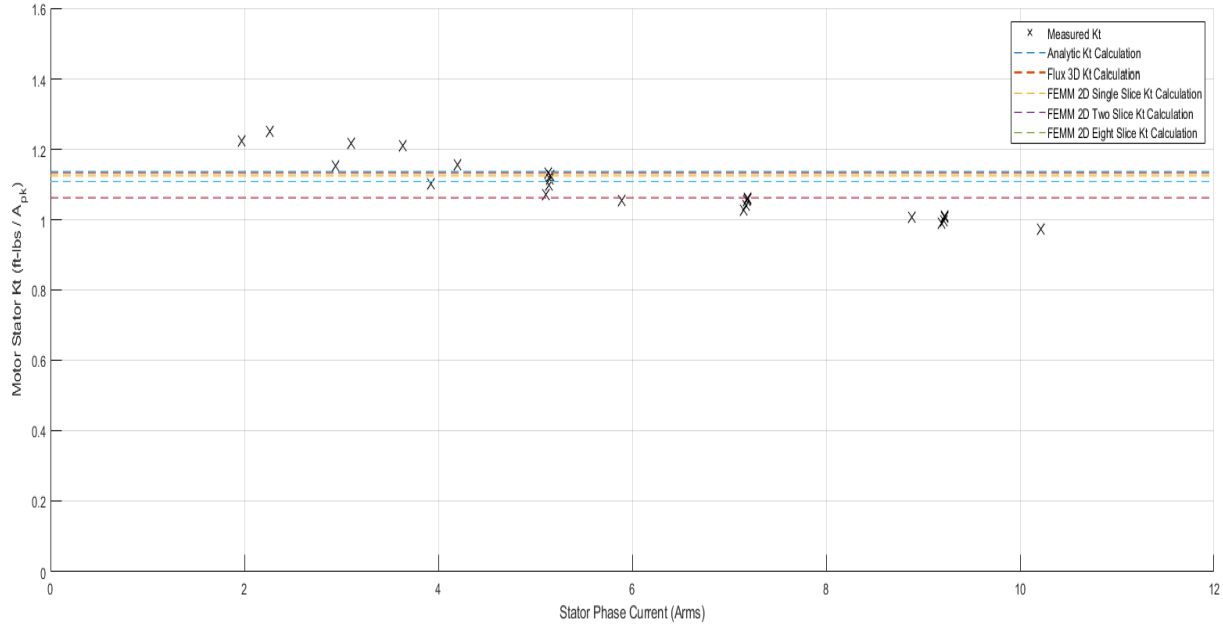

Figure 101. SRDS AFPM Measured Torque Constant, Kt

6.4.1 Discussion of Load and Efficiency Test Results

Similar to inductance, resistance and BEMF test results, the measured efficiency and motor torque constants appear to correlate well with analytical and finite element predictions. Under light load, and especially at higher speeds there is an observable deviation in predicted motor efficiency vs. measured motor efficiency.

Attempts were made to minimize test setup drag through coupling alignment, but these did not appreciable improve the correlation at low load. Interestingly the deviation between measured and predicted efficiency seems to diminish with load, perhaps indicating a static drag (DC) torque not accounted for in the test setup.

The measured motor torque constant data appears to correlate well with analytic, 2D and 3D FE predictions. Interestingly we see a trend of decreasing Kt with applied current, but independent of speed. During initial test setup the VFD was timed to provide current in phase with BEMF, and throughout testing the current angle was not adjusted, as to be consistent with finite element modeling efforts and predictions. However, this lagging Kt indicates that perhaps additional current phase control may be beneficial at implementation.

6.5 Summary of Experimental Data

Chapter 6 provided experimental data from a prototype SRDS AFPM for standard test described in [33]. The SRDS AFPM tested matched the geometry analyzed in Chapter 5. The first portion of this chapter outlined the machine under test as well and defined the various test configuration utilized to conduct experimental work and gather test data.

The next portion of Chapter 6 measured the prototype SRDS AFPMs BEMF and post-processed the data in a manner similar to was presented Chapter 5. This test data was compared against analytic, 2D and 3D FE results, indicating good agreement between all methods, with 3D FE RMS voltage correlating the closest. The prototype SRDS AFPMs BEMF THD was measured and compared against all presented analysis techniques. THD measurements were correlated with all presented analysis methods, indicating that all methods are capturing the machine space harmonics accurately.

The third portion of Chapter 6 measured phase resistance and inductance of the prototype SRDS AFPM for comparison against modeling predictions. Inductance predictions correlated within the phase to phase variance measured in the prototype machine and analytical phase resistance estimates were within approximately 11% the average machine measurement.

Lastly Chapter 6 measured the prototype SRDS AFPMs loaded efficiency and torque constant. The measured efficiency had a notable deviation at low load, high speed but otherwise correlate well. Measured motor torque constants were also presented, indicating good correlation to motor predictions.

Chapter 7

Conclusions and Future Work

7.1 Conclusions

This thesis set out to investigate the SRDS AFPM through development of analytical modeling equations for BEMF, inductance, resistance and overall machine performance. Additionally, this thesis proposed a method of discretizing the inherently 3D topology of an AFPM into a single, or series of 2D FE model for the purpose of quantifying the accuracy of 2D FE modeling techniques, relative to analytic and 3D FE predictions as well as test data. Lastly this thesis developed and tested a prototype SRDS AFPM for comparison and validation of predictions and methods.

Analytical formulas for predicting the SRDS AFPM inductance, resistance, BEMF and phase current were developed as an extension of classic RFPM analysis techniques. These RFPM derived analysis techniques were then extended to conduct performance predictions for a prototype SRDS AFPM with integral slot-pole windings. Results of analysis correlated will with test data and multiple FE predictions.

A 2D FE modeling methodology was presented for the SRDS AFPMs as well as strategies for increasing 2D FE model accuracy and alternative geometric boundary conditions. Modeling efforts substantiated that 2D FE voltage and torque prediction correlation, relative to 3D FE analysis can be increased through discretization of the 2D FE model into several 2D models, each representing a small portion of the AFPM. Cogging torque prediction correlation did not increase with further discretization of the AFPM, however the general characteristics of cogging wave shape and frequency were captured through the 2D FE modeling. Efforts to use alternative geometric boundary conditions did produce results, however the erratic nature of torque predictions, coupled with inherent asymmetry in predictions did not improve accuracy relative to more classic 2D modeling methods.

Experimental measurements were presented, which verified analytical predictions of resistance, inductance and BEMF. Experimental measurements of torque per ampere of current also closely correlated with 3D FE results, validating the presented analytical, 2D and 3D modeling techniques for a SRDS AFPM. Lastly, experimental efficiency measurements were conducted on the prototype SRDS AFPM and compared against analytical predictions. Experimental efficiency results correlated well with predictions, with a noted discrepancy at light loads which was more pronounced at higher rotational speeds.

7.2 Recommendations for Future Work

The following Section presents opportunities and recommendations for future work.

7.2.1 2D FE Modeling of Alternative Axial Flux Machines

This thesis has focused on the SRDS configuration of AFPMs. The modeling techniques presented in this thesis represent an approach of simplifying any axial flux machine into a 2D, or series of 2D FE models. Future work could apply this technique to axial flux induction motors, multi-gap axial flux permanent magnet or other Non-SRDS AFPM configurations.

7.2.2 2D FE Modeling of Alternative Slot and Magnet Configurations

This thesis only consider an SRDS AFPM which had parallel sided slots and pie shaped magnets which had a constant magnet fraction. However, this same approach could be adapted to other slot and magnet configurations. Of particular interest, this approach could be adapted to account for stator or rotor skew.

7.2.3 2D FE Optimization and Design of Experiments

This thesis proposed several methods for modeling SRDS AFPMs using 2D FE as well as a method of increasing 2D FEA accuracy, relative to 3D FEA. Furthermore, the thesis empirically showed that 2D FEA can be conducted with significantly less computational time than 3D FEAs. Coupling the proposed methods and reduced computational requirements could be adapted to conduct optimization studies and Design of Experiments for SRDS AFPMs as well as other AFPM topologies.

7.2.4 2D FE Cogging Prediction Refinement

This thesis focused on the case study of a one SRDS AFPM and varied the 2D FE analysis techniques for comparison against each other. The machine under consideration produced a relatively low cogging torque, which resulted in large percentage-based deviation of cogging predictions between 2D FE and 3D FE modeling efforts. While the deviation was approximately 30% between the two methods, the absolute different was approximately 0.16 ft-lbs.

It would be beneficial to exercise the 2D FE modeling approach across several machine designs to understand if cogging predictions produce a DC offset, or if 2D modeling consistently produces a relatively large percentage of error, relative to 3D FE modeling.

7.2.5 Analytical BEMF Prediction

The presented method of analytically predicting BEMF waveforms assumes a non-pole shaped magnet and relied upon the fact that the machine under consideration utilized an integral slot-pole combination. It would be beneficial to adapt this method for use with fractional slot motors, through development of alternative winding functions. It would be further beneficial to incorporate a function to account for pole-shaping of the magnets or an alternative Fourier Series to capture the effects of pole shaping.

7.2.6 Quantification of 3D FE Effects

When comparing 2D FE results against 3D FE results, the 3D model consistently predicted less torque output per ampere of current as well as lower terminal voltage. The 3D model also consistently prediction lower cogging torque. This thesis hypothesized that these variance were the result of end effects as well as off-axis flux linkage. Future efforts could expand this hypothesis, quantifying and characterizing end effects in AFPM machines. This research could potential leverage or further understanding of radial field end effects as well as other machine topologies.

References

[1] J. Gieras, R. Wang, M. Kamper, Axial Flux Permanent Magnet Brushless Machines, 2004.

[2] T.M. Jahns, “The Expanding Role of PM machines in Direct-Drive Applications”, Proc. of 2011 Intl. Conference on Electric Machines and Systems (ICEMS’11), Aug. 2011.

[3] Zhu, Howe, “Analytical Prediction of Cogging Torque in Radial-Field Permanent Magnet Brushless Motors”, IEEE Transaction on Magnetics, Vol. 28, No. 2, March 1992.

[4] J.L. Kirtley, “6.685 Electric Machines, Fall 2005”, http://hdl.handle.net/1721.1/85612

[5] Technical Data Sheet, PA44-450/LC Permanent Magnet Motor. 2018. https://www.leonardodrs.com/media/7119/pa44-625_datasheet.pdf

[6] Moreels, Leijen, “High Efficiency Axial Flux Machines”, April 2018. https://www.magnax.com/products

[7] M. M. Liwschitz, "Distribution Factors and Pitch Factors of the Harmonics of a Fractional-Slot Winding," in *Transactions of the American Institute of Electrical Engineers*, vol. 62, no. 10, pp. 664-666, Oct. 1943.

[8] W.A. Salah, D. Ishak, K.J. Hammadi, “Minimization of Torque Ripples in BLDC Motors due to Phase Commutation –a review”, Przeglad Electrotechniczny (Electrical Review), January 2011, pp. 183-188.

[9] J.L. Kirtley, “Electric Power Principles Sources, Conversion, Distribution and Use”, 2010.

[10] W.L. Soong, “Sizing of Electrical Machines”, Power Engineering Briefing Notes Series #9, Sep. 2008.

[11] P. Mongeau, "High performance electric drivetrain components," in *IEEE Transactions on Magnetics*, vol. 31, no. 1, pp. 67-72, Jan. 1995.

[12] D. J. Patterson, J. L. Colton, B. Mularcik, B. J. Kennedy, S. Camilleri and R. Rohoza, "A comparison of radial and axial flux structures in electrical machines," *2009 IEEE International Electric Machines and Drives Conference*, Miami, FL, 2009, pp. 1029-1035.

[13] D. Hanselman, “Brushless Permanent Magnet Motor Design”, 2006.

[14] R.D. Lorenz, L.P. Haines, “Understanding Modern Power Conversion”, 2010, 3rd Ed., pp. 3-4

[15] A. Fitzgerald, C. Kingsley, S. Umans, “ Electric Machinery”, 1990, 5th Ed., pp. 224

[16] W.L. Soong, “Permanent Magnet AC Machines: Principles, Design and Analysis,” University of Wisconsin – Madison, 2009.

[17] J.R. Hendershot, T.J.E. Miller, “Design of Brushless Permanent-Magnet Machines”, 2010

[18] T.J.E. Miller, M.I. McGilp, D.A. Staton, J.J Bremner, “Calculation of Inductance in permanent-magnet DC motors”, IEE Proc. Of 1999, Electric Power Applications, Vol. 146 No. 2, Mar. 1999

[19] A.M. El-Refaie, Z.Q. Zhu, T.M. Jahns, D. Howe, “Winding Inductances of Fractional Slot Surface-Mounted Permanent Magnet Brushless Machines, in Industry Application Society Annual Meeting, 2008, IAS ’08 (IEEE, 2008), pp.1-8

[20] S.W. Colton, “Design and prototyping methods for brushless motors and motor control,” Massachusetts Institute of Technology, 2010.

[21] E. Hewitt, R. Hewitt, C. Truesdell, ‘The Gibbs-Wilbraham Phenomenon: An Episode in Fourier Series Analysis’, Archive for History of Exact Sciences, vol. 21, no. 2, pp. 129-160, 1979

[22] R. Hamming, *Numerical Methods for Scientists and Engineers*, 1986, pp. 534-536.

[23] Technical User Manual, Yaskawa F7 Variable Frequency Drive, 2008 https://www.yaskawa.com/delegate/getAttachment?documentId=TM.F7.01&cmd=documents&openNewTab=true&documentName=TM.F7.01.pdf

[24] J. Coulomb and G. Meunier, "Finite element implementation of virtual work principle for magnetic or electric force and torque computation," in *IEEE Transactions on Magnetics*, vol. 20, no. 5, pp. 1894-1896, September 1984.

[25] J. Coulomb, "A methodology for the determination of global electromechanical quantities from a finite element analysis and its application to the evaluation of magnetic forces, torques and stiffness," in *IEEE Transactions on Magnetics*, vol. 19, no. 6, pp. 2514-2519, November 1983.

[26] Gieras, Wing, “Permanent Magnet Motor Technology”, 2002

[27] Shigley, Mischke, “Mechanical Engineering Design”, 5th ed., 1989

[28] A. El-Refaie *et al*., "Comparison of traction motors that reduce or eliminate rare-earth materials," *2016 IEEE Energy Conversion Congress and Exposition (ECCE)*, Milwaukee, WI, 2016, pp. 1-8.,

[29] J.S. Walker, “Physics”, 2002

[30] N.L. Schmitz, D.W. Novotny, “Introductory Electromechanics”, 1965

[31] K. Sitapati, R. Krishnan, “Performance comparisons of radial and axial field, permanent-magnet, brushless machines,” *IEEE Trans. Ind. Appl*., vol. 37, no. 5, pp. 1219-1226,2001.

[32] K.M. Rahman, N.R. Patel, T.G. Ward, J.M. Nagashima, F. Caricchi, F. Crescimbini, “ Application of direct-drive wheel motor for fuel cell electric and hybrid electric vehicle propulsion system,” *IEEE Trans. Ind. Appl.*, vol. 42 no. 5, pp. 1185-1192, Sep. 2006.

[33] Guide to General-Purpose Synchronous Motors without Excited Rotor Windings, NEMA SM 1-2017

[34] T.M. Jahns, “ECE 711 Lecture Notes,” University of Wisconsin -- Madison, Spring 2018.

[35] T.T. Hambleton, L.V. Bewley, “The Synchronous Converter Theory and Calculations”, Transactions of the American Institute of Electrical Engineers, vol. XLVI, pp.60-76, 1921

[36] B. Hague, S. Neville, “The Properties of the Distribution Factor of Armature Windings”, Journal of the Institution of Electrical Engineers, vol. 60, issue 312, 1922

[37] L.V. Bewley, “Induced Voltage of Electric Machines”, Transactions of the American Institute of Electrical Engineers, vol. 49, issue 2, 1930

[38] J.H. Kim, “Design and analysis of axial flux machine with example studies,” University of Wisconsin -- Madison, 2014.

[39] M. Aydin, “Axial flux surface mounted permanent magnet disc motors for smooth torque traction drive applications,” University of Wisconsin -- Madison, 2004.

[40] Technical Data Sheet, PA57-1000 Permanent Magnet Motor. 2018. http://www.leonardodrs.com/media/6888/pa57-1000_datasheet.pdf

[41] C.C. Jensen, “A novel axial field permanent magnet machine using amorphous iron,” University of Wisconsin -- Madison, Department of Electrical Engineering, 1989.

[42] F. Magnussen, C. Sadarangani, “Winding Factors and Joule Losses of Permanent Magnet Machines with Concentrated Windings” *IEEE International Electric Machines and Drives Conference, 2003. IEMDC'03.*, Madison, WI, USA, 2003, pp. 333-339 vol.1.

[43] A. Watanabe, T. Saito, T. Ueno, H. TSURUTA, Y. Nakamura, “Thin and High-Torque Axial Gap Motor Using Soft Magnetic Powder Cores”, https://global-sei.com/technology/tr/bn86/pdf/86-21.pdf

[44] A. Mlot, A. C. Malloy and M. U. Lampérth, "Effect of rotor/stator misalignment on the performance of a permanent magnet axial-flux motor," *8th IET International Conference on Power Electronics, Machines and Drives (PEMD 2016)*, Glasgow, 2016, pp. 1-6.

[45] J. Li, Y. Lu, Y. Cho and R. Qu, "Design an Analysis of a Water-Cooled Axial Flux Permanent-Magnet Machine for Large Power Direct-Driven Applications," *2018 XIII International Conference on Electrical Machines (ICEM)*, Alexandroupoli, 2018, pp. 118-124.

[46] G. Brown, A. Kascak, B. Ebihara, D. Johnson, B. Choi, M. Siebert, C. Buccieri, “NASA Glenn Research Center Program in High Power Density Motors for Aeropropulsion”, Report NASA/TM-2005-213800, National Aeronautics and Space Administration, 2005.

[47] Technical Presentation, “Electrified Thinking”, GKN EVO eDrive Systems, http://projects.iqsoft.co.in/EVS26-UK-SEMINAR-Evo-Electric.pdf

[48] Technical Data Sheet, Launch Point Technologies 45kW Gen-Set, rev. 1, 2019. https://cdn2.hubspot.net/hubfs/53140/45kW%20gen%20set%20data%20sheet_R1.pdf

[49] Y. Xu, Q. Li, L. Zhang and Q. Ma, "Development of permanent magnet synchronous motor for electric vehicle," *2009 International Conference on Sustainable Power Generation and Supply*, Nanjing, 2009, pp. 1-5.

[50] Fu Minli, "Design of Permanent Magnet Synchronous Motor for Electric Vehicle Drive," Converter Technology & Electric Traction, pp. 48-52, May. 2007

[51] E. A. Grunditz, S. T. Lundmark, M. Alatalo, T. Thiringer and A. Nordelöf, "Three traction motors with different magnet materials — Influence on cost, losses, vehicle performance, energy use and environmental impact," *2018 Thirteenth International Conference on Ecological Vehicles and Renewable Energies (EVER)*, Monte-Carlo, 2018, pp. 1-13.

[52] R. Madhavan and B. G. Fernandes, "Axial flux segmented SRM with a higher number of rotor segments for electric vehicles," IEEE Trans. Energy Convers., vol. 28, no. 1, pp. 203–213, Mar. 2013.

[53] M. Aydin, S. Huang, and T. A. Lipo, "Design, analysis, and control of a hybrid field-controlled axial-flux permanent-magnet motor," *IEEE Trans. Ind. Electron.*, vol. 57, no. 1, pp. 78–87, Jan. 2010.

[54] K. Sitapati and R. M. Krishnan, "Performance comparisons of radial and axial field, permanent-magnet, brushless machines," IEEE Trans. Ind. Appl., vol. 37, no. 5, pp. 1219–1226, Sep./Oct. 2001.

[55] M. Aydin, S. Huang, and T. A. Lipo, "Torque quality and comparison of internal and external rotor axial flux surface-magnet disc machines," IEEE Trans. Ind. Electron., vol. 53, no. 3, pp. 822–830, Jun. 2006

[56] D. D. Tremelling, "On the design and analysis of a printed circuit board in a high speed surface permanent magnet axial flux machine," University of Wisconsin -- Madison, 2009.

[57] J. H. Kim and B. Sarlioglu, "Preliminary design of axial flux permanent magnet machine for marine current turbine," in *Proc. 39th IEEE IECON*, 2013, pp. 3066–3071.

[58] G. De Donato, F. Giulii Capponi, G. A. Rivellini and F. Caricchi, "Integral-Slot Versus Fractional-Slot Concentrated-Winding Axial-Flux Permanent-Magnet Machines: Comparative Design, FEA, and Experimental Tests," in *IEEE Transactions on Industry Applications*, vol. 48, no. 5, pp. 1487-1495, Sept.-Oct. 2012.

[59] J. H. Kim and B. Sarlioglu, "Investigation of effect of slot opening on fractional slot and integer slot axial flux permanent magnet machine," *2015 IEEE Energy Conversion Congress and Exposition (ECCE)*, Montreal, QC, 2015, pp. 2956-2963.

[60] A. Egea, G. Almandoz, J. Poza, G. Ugalde and A. J. Escalada, "Axial-Flux-Machine Modeling With the Combination of FEM-2-D and Analytical Tools," in *IEEE Transactions on Industry Applications*, vol. 48, no. 4, pp. 1318-1326, July-Aug. 2012.

[61] D. Jaksic, ""Getting rid of the air", or how to maximize winding fill factor (ID 81)," *2011 1st International Electric Drives Production Conference*, Nuremberg, 2011, pp. 84-87.

[62] Technical Data Sheet, DI-MAX M-10X Non-Oriented Electrical Steels, 2014 https://www.aksteel.com/sites/default/files/2018-01/dimaxm-10x201406_2.pdf

[63] S. Huang, Jian Luo, F. Leonardi and T. A. Lipo, "A general approach to sizing and power density equations for comparison of electrical machines," *IAS '96. Conference Record of the 1996 IEEE Industry Applications Conference Thirty-First IAS Annual Meeting*, San Diego, CA, USA, 1996, pp. 836-842 vol.2.

[64] N. Taran, V. Rallabandi, G. Heins and D. M. Ionel, "A comparative study of conventional and coreless axial flux permanent magnet synchronous motors for solar cars," *2017 IEEE International Electric Machines and Drives Conference (IEMDC)*, Miami, FL, 2017, pp. 1-7.

[65] D. Meeker, "Finite Element Method Magnetics Version 4.2 User Manual", Oct. 2015

[66] D. Meeker, Finite Element Method Magnetics, Version 4.2 (25Feb2018 Build), http://www.fem.info

[67] Altair, Flux, Version 2018.0 (25Jan2018 Build), https://altairhyperworks.com/product/flux

[68] S. McFee, J.P. Webb, D.A. Lowther, "A tunable volume integration formulation for force calculation in finite-element based computational magnetostatics," IEEE Transactions on Magnetics, 24(1):439-442, January 1988.

[69] F. Henrotte, G. Deliege, K. Hameyer, "The eggshell method for computation of electromagnetic force on rigid bodies in 2D and 3D," CEFC 2002, Perugia, Italy, April 16-18, 2002.

[70] Altair, Flux, "User Guide Flux 2018 Volume 3", Jan. 2019

[71] J. F. Calvert, "Amplitudes of Magnetomotive-Force Harmonics for Fractional-Slot Windings of Three Phase Machines", 1939.

[72] N. Bianchi, S. Bolognani, M. D. Pre and G. Grezzani, "Design considerations for fractional-slot winding configurations of synchronous machines," in IEEE Transactions on Industry Applications, vol. 42, no. 4, pp. 997-1006, July-Aug. 2006.